Discrete Element Method to Model 3D Continuous Materials

Discrete Element Model and Simulation of Continuous Materials Behavior Set

coordinated by
Ivan Iordanoff

Volume 1

Discrete Element Method to Model 3D Continuous Materials

Mohamed Jebahi
Damien André
Inigo Terreros
Ivan Iordanoff

ISTE

WILEY

First published 2015 in Great Britain and the United States by ISTE Ltd and John Wiley & Sons, Inc.

ISTE Ltd
27-37 St George's Road
London SW19 4EU
UK

www.iste.co.uk

John Wiley & Sons, Inc.
111 River Street
Hoboken, NJ 07030
USA

www.wiley.com

Library of Congress Control Number: 2015930631

British Library Cataloguing-in-Publication Data
A CIP record for this book is available from the British Library
ISBN 978-1-84821-770-6

Contents

List of Figures

List of Tables

Preface

Bridging the scales for material multiphysical studies.

Smart materials, Added Value Manufacturing, and factories for the future are key technological subjects for the future product developments and innovation. One of the key challenges is to play with the microstructure of the material to not only improve its properties but also to find new properties. Another key challenge is to define micro- or nano-composites in order to mix physical properties. This allows enlarging the field of possible innovative material design. The other key challenge is to define new manufacturing processes to realize these materials and new factory organization to produce the commercial product. From the material to the product, the numerical design tools must follow all these evolutions from the nanoscopic scale to the macroscopic scale (simulation and optimization of the factory). If we analyze the great amount of numerical tool development in the world, we find a great amount of development at the nanoscopic to the microscopic scales, typically linked to *ab initio* calculations and molecular dynamics. We also find a great amount of numerical approaches used at the millimeter to the meter scales. The most famous in the field of engineering is the finite element method (FEM). But there is a numerical death valley to pass

though, from micrometers to several centimeters. This scale corresponds to the need for taking into account discontinuity or microstructures in the material behavior at the sample scale or component scale (several centimeters). Since the 2000's, some attempts have been carried out to apply the discrete element method (DEM) for simulation of continuous materials. This method has been developed historically for true granular materials, like sand, civil engineering grains or pharmaceutical powders. Some recent developments give new and simple tools to simulate quantitatively continuous materials and to pass from microscopic interactions at the material scale to the classical macroscopic properties at the component scale (stress and strain, thermal conductivity, cracks, damages, electrical resistivity, etc.).

In this set of books on descrete element model and simulation of continuous materials, we propose to present and explain the main advances in this field since 2010. This first book primarily explains in a clear and simple manner the numerical way to build a DEM simulation that gives the right (same) macroscopic material properties, e.g. Young Modulus, Poisson Ratio, thermal conductivity, etc. Then, it shows how this numerical tool offers a new and powerful method for analysis and modeling of cracks, damages and finally failure of a component. The second book [JEB 15] presents the coupling (bridging) between DEM method and continuum numerical methods, like the FEM. This allows us to focus DEM on the parts where the microscopic properties and discontinuities conduce the behavior and allow FEM calculation where the material can be considered as continuous and homogeneous. The last book [CHA 15] presents the object oriented numerical code developed under the free License GPL: GranOO (www.granoo.org). All the presented developments are implemented in a simple way on this platform. This allows scientists and engineers to test and contribute to improving the presented methods in a simple and open way.

Now, dear reader let us open this book and welcome in the DEM community for the material of future development ...

Ivan IORDANOFF
January 2015

Introduction

I.1. Toward discrete element modeling of continuous materials

The most fascinating and interesting problems in mechanics are also often the most difficult to resolve. To overcome this difficulty, a natural way in which the scientists proceed is to subdivide the studied problem into individual components or elements, whose behavior is readily understood, and to rebuild the original problem from these components to study its behavior. This is the key idea of a numerical simulation. Starting from the 1960s, numerical simulation has become a significant and, at times, an essential approach in the progress of many areas in engineering and science. With the help of increasing computer power, this modern numerical approach makes it possible to solve mechanical problems in all their detail without making too many simplifying assumptions and approximations, as when adopting the traditional theoretical practice. Nowadays, such an approach plays a valuable role in providing validation for theories, offers insights into the experimental results and assists in the interpretation or even the discovery of new phenomena. In certain cases, the problem of interest is of a discrete nature. Therefore, a finite number of well-defined components are sufficient to obtain an

adequate model of the studied problem. With the current computer capacity, discrete problems can be solved even if a large number of components are involved. The numerical methods used to solve such problems will be called discrete methods (DMs). However, in most situations, the problem needs to be indefinitely subdivided into infinitesimal components, leading to local (usually differential) governing equations which imply an infinite number of components. Such a problem is called "continuous" problem. In continuous problems (also called continua), the studied material is assumed to be continuous and to completely fill the space it occupies. As the computer capacity is finite, continuous problems can only be solved exactly by mathematical techniques, which are usually limited to very simplified situations.

To circumvent the intractability of realistic continuous problems, various methods of discretization have been proposed. All the methods involve an approximation which, hopefully, tends toward the true solution (of the continuous problem) as the number of discrete variables increases. These methods are known as continuum methods (CMs). The most important among the CMs is the finite element method (FEM) [ZIE 05a, ZIE 05b, ZIE 05c]. This method is undoubtedly the most popular and powerful numerical approach for studying the behavior of a wide range of engineering and physical problems. This method is classically used to simulate mechanical problems having length scales much greater than the interatomic distances, and for which the continuity assumption is valid and remains valid during simulation. Solving a continuous problem using the FEM method undergoes a preliminary step of meshing (discretization) which aims to subdivide the problem domain into a finite number of elements, called meshes or grids, whose mechanical behavior is defined using a finite number of parameters. The major drawback of this method is that the associated governing equations arise from continuum

mechanics, based on a predefined mesh or grid. Therefore, it faces great difficulties to predict most of the complex microscopic effects, which can strongly influence the macroscopic behavior, e.g. fracture, fatigue and durability.

A large number of attempts have been made to correct the shortcomings of this method. The one most commonly used is the rezoning (remeshing) technique, which aims to rezone (remesh) the problem domain or simply the regions where the initial mesh is severely affected. The computation is then resumed on the new mesh. The field variables are approximated at the nodes of the new mesh by mass, momentum and energy transport. Despite the great success of this technique in the simulation of complex problems, it has several difficulties which can limit its application. The rezoning procedure can be tedious and time-consuming. Besides, the transport of the field variables from the old to the new mesh is generally accompanied by material diffusion which can lead to a loss of material history [BEN 92]. Furthermore, the numerical results are generally mesh dependent. To alleviate these difficulties, Moës *et al.* [MOË 99] have developed the extended finite element method (XFEM). This approach is based on the concept of local partition of unity [CHE 03]. It extends the standard FEM by enriching the approximated solution space so as to naturally reproduce the challenging features (e.g. discontinuity and singularity) associated with the studied problem. Originally, this method was developed to model fracture problems that are challenging for the traditional FEM. The standard polynomial basis functions for nodes belonging to elements that are interested in the cracking mechanisms are enriched by discontinuous basis functions. The enriched basis, which includes crack opening displacements, is then used to simulate fracture. Subsequent research has illustrated that this method can also be used to solve problems involving more general localized effects, e.g. singularities, material interfaces or voids, which can be described by an appropriate

set of basis functions. A key advantage of XFEM is that the mesh topology does not need to conform with the discontinuity surfaces, and then the mesh does not need to be updated to track the microscopic effects (e.g. crack path). This makes it possible to alleviate the computation costs and the projection errors, compared to standard FEM. However, embedding complex features and effects into the approximation space is not always a straightforward issue. For example, application of this method to simulate problems with complex crack patterns, such as multiple cracks or crack nucleation at multiple locations, presents a huge challenge and is currently the subject of several studies. The difficulties and limitations of this method are particularly evident when simulating hydrodynamic phenomena such as explosion and high velocity impact (HVI). In parallel with these efforts to improve the FEM and grid-based methods in general, an emerging number of new ideas have been led since the 1970s for the development of alternative approaches. These approaches now compete with traditional grid-based methods. One main direction has resulted in the next generation of CMs: meshfree methods. Among these methods, we can cite the smoothed-particle hydrodynamics (SPH) and its different variants (e.g. corrective SPH, discontinuous SPH) [LIU 03, RAN 96, LIU 10], moving least square (MLS) [LEV 98] and element-free Galarkin method (EFGM) [BEL 94]. The main objective of the meshfree methods is to provide an accurate and stable numerical solution for the governing equations of the studied problem with a set of arbitrarily distributed nodes (or particles) without using any mesh or connectivity between them. Since the problem domain is only represented by a set of scattered nodes, rather than a system of predefined meshes or grids, these methods are attractive in dealing with problems that are difficult for traditional (grid-based) CMs. Nonetheless, they are very time-consuming and they suffer from several numerical problems, such as accuracy degradation near the boundaries and difficulties to impose essential (Dirichlet) boundary

conditions. In addition, they generally lead to approximation errors larger than those obtained using grid-based methods.

Despite the diversity of the proposed solutions, accurate description and modeling of several important mechanical problems have long been a challenge for traditional continuum-based theories, and then for CMs. Indeed, certain inherent drawbacks caused by the reliance of these methods on computation meshes and unsuitability in dealing with discontinuities are still not adequately addressed. In contrast, the DMs such as molecular dynamics (MD) [ALD 57, ALD 59] and discrete element method (DEM) [CUN 71, CUN 79] are based on discrete mechanics and do not rely on any kind of mesh. The domain of interest is modeled by a discrete system made up of fully persistent discontinuities delimiting a set of rigid (or pseudo-deformable) bodies that are in interaction with each other by interaction laws through these discontinuities. Although these methods were originally developed to study naturally discrete problems (e.g. powder or granular material problems), some of their features are very attractive for several continuous problems that cannot be easily solved by CMs (e.g. damage, fracture, discontinuities and fragmentation). Indeed, these methods naturally take into account discontinuities, and then there is no need for complex transition procedure from continuum phase to discontinuum phase. However, the lack of theoretical basis has seriously restricted their application on continua until recent years. Mainly, two significant challenges must be tackled to this end: (1) the first challenge is concerned with the choice of the cohesive links (bonds) between adjacent discrete elements and the identification of their microscopic parameters so as to ensure a correct macroscopic behavior; (2) the second challenge is concerned with the construction of a discrete domain taking into account the structural properties of the original problem domain, e.g. homogeneity and isotropy, such that the macroscopic mechanical behavior is independent of

the number of discrete elements. The terms "microscopic" and "macroscopic" are used here to designate, respectively, the bond (cohesive link) level and the domain level. This bears no reference to modeling scales as otherwise used in material modeling. Although some works contributing to address the first challenge (correspondence between the microscopic and macroscopic properties) can be found in the literature, the second challenge has remained up to very recently far from being tackled.

To develop relationships between microscopic and macroscopic properties, two approaches have been proposed in the literature: analytical approach and numerical approach (calibration). In the case of regular two-dimensional (2D) lattices, Potapov *et al.* [POT 95a, POT 95b] have shown that the macroscopic properties can easily be derived by a hand calculation, using bond-level strain–stress formulas. Based on energy considerations, Wang and Mora [WAN 08] have extended the works of Potapov *et al.* [POT 95a, POT 95b] to regular three-dimensional (3D) lattices. As for general 3D lattices, the relationships between microscopic and macroscopic properties can be derived using the principle of energy conservation, which posits that the external work and the potential energy (stored elastic energy of the bonds) are equivalent. This can be done in a discrete manner by summing bonds between discrete elements or using integral form of a fictitious continuous lattice [KUH 01, LIA 97]. In this derivation, the external work is estimated using a kind of homogeneous strain field, which is not well defined and can lead to relatively large and inescapable estimate errors [LIA 97]. This represents the weak link of the analytical approach. To overcome this limitation, other authors [HEN 04a] have proposed a numerical approach based on "best-fit" strategy. In this approach, the microscopic properties corresponding to the expected macroscopic properties are determined by calibration.

I.2. Scope and objective

The major drawback of the existing (analytical and numerical) approaches to relate microscopic and macroscopic properties is that the obtained relationships between these quantities are most often dependent on the number of discrete elements used to discretize the problem domain. Therefore, these relationships must be recalculated each time the domain discretization is refined, which can be tedious and costly. Besides, the discretization of the studied domain generally does not reflect the structural properties (e.g. isotropy and homogeneity) of this domain. A discrete domain having some regularities (e.g. identical discrete elements and arranged discrete elements along the axes) may lead to an anisotropic mechanical behavior at the structure level. To overcome these problems, André *et al.* [AND 12b, AND 13, AND 14] have recently proposed a new methodology allowing for correct discrete element modeling of 3D continua. This methodology is developed for a particular DEM variation in which the interaction between the adjacent discrete elements is ensured by 3D cohesive beam bonds, but it can easily be extended for other DEM variations. As shown by André *et al.* [AND 12b], several conditions must be fulfilled to ensure equivalence between a continuum and its DEM representation (from both geometric and mechanical points of view) and to get round the fineness dependence of the results. These conditions are divided into two classes: (1) conditions on the construction of the DEM domain to ensure a "good" geometric representation of the continuous domain and (2) conditions on the mechanical behavior of the cohesive beam bonds between the discrete elements to ensure a correct macroscopic behavior. These conditions are intimately bound up with each other in such a way that the proposed methodology is valid only when all of them are applied. Further work carried out by the same research team [TER 13] has shown that this methodology can also be

applied to preform DEM modeling of thermal conduction in 3D continua.

The present book aims at bringing together the various developments performed on the newly proposed variation of DEM for 3D discrete element modeling of continuous materials. This book is dedicated to detailing the basic ideas and formulation of this variation and to providing a comprehensive and robust methodology to model mechanical behavior, thermal conduction and brittle fracture of these materials.

I.3. Organization

Following this Introduction, the book is organized as follows:

– Chapter 1 introduces some background knowledge of discrete element modeling. The different classes of DMs are quickly reviewed so that the place of the DEM variation used in this book can be distinguished. Subsequently, analytical and numerical approaches used to assess macroscopic variables (e.g. stress and strain tensors) in discrete element modeling are briefly discussed.

– Chapter 2 constitutes the main chapter of the book. It covers the formulation and implementation of the newly developed DEM variation as well as the proposed methodology to correctly model a continuum, and discusses various aspects of the approach. This approach not only systematically derives a robust DEM representation of a continuous problem, but also guarantees fineness independence of the numerical results beyond a certain number of discrete elements.

– Chapter 3 is devoted to DEM modeling of thermal conduction in 3D continua. It describes a fast and efficient method, based on the methodology presented in the previous chapter, to simulate heat conduction through a 3D continuum by the proposed DEM variation.

– Chapter 4 deals with brittle fracture simulation. It shows how the present DEM variation allows us to simply implement fracture criteria and test the effect on the structure. Two brittle fracture models are discussed. As will be shown, some of the existing fracture models fail to reproduce the cracking mechanisms at the microscopic scale correctly, which can undermine application of DMs for fracture problems. To overcome the limitations of these models, this chapter proposes an approach based on the computation of an equivalent stress tensor at the discrete elements.

– Finally, the book ends with several conclusions.

1

State of the Art: Discrete Element Modeling

1.1. Introduction

As mentioned in the previous chapter, in conjunction with the accelerating progress in computer science and software technology, the final decades of the 20th Century have seen an explosion of powerful numerical methods which can be classified into discrete methods (DMs) and continuum methods (CMs). These methods have been used over the years to simulate a wide variety of mechanical problems at different scales. Typically, four scales can be distinguished in the context of numerical simulation:

– the nanoscopic (or atomic) scale ($\sim 10^{-9}$ m), where phenomena related to the behavior of electrons become significant. At this scale, the interaction between particles (electrons, atoms, etc.) is directly dictated by their quantum mechanical (QM) state;

– the microscopic scale ($\sim 10^{-6}$ m), where phenomena related to the behavior of atoms are considered. The interaction between atoms is governed by empirical interatomic potentials, which are generally derived from

Discrete Element Method to Model 3D Continuous Materials, First Edition.
Mohamed Jebahi, Damien André, Inigo Terreros and Ivan Iordanoff.

QM computations. Classic Newtonian mechanics is used to compute the displacements and rotations of atoms;

– the mesoscopic scale ($\sim 10^{-4}$ m), where phenomena related to lattice defects are considered. At this scale, the atomic degrees of freedom are not explicitly treated, and only larger scale entities (clusters of atoms, clusters of molecules, etc.) are considered. The interaction between particles is also described by classic Newtonian mechanics;

– the macroscopic scale ($\sim 10^{-2}$ m), where macroscopic phenomena which can be described by continuum mechanics are considered. At this scale, the studied physical systems are regarded as continua, whose associated behavior is described by constitutive laws.

Typically, the DMs cover the first three scales. At these scales, the length scale of interest is at the same order of magnitude as the discontinuity spacing, which makes inappropriate the application of traditional CMs. Otherwise, additional handling is required to correctly reproduce phenomena associated with discontinuities like strain localization at crack initiation. At the macroscopic scale, most of the interesting materials can be treated as continua even though they consist of discrete grains at smaller scales. CMs can therefore be used without remorse at this scale. However, it is often rewarding to model such materials as discontinuous by DMs because new knowledge can be gained about their macroscopic behavior when their microscopic mechanisms are understood. The need to model these materials as discontinuous is even more rooted when they are characterized by complex nonlinear mechanical behaviors that cannot easily be described by traditional continuum theories, e.g. anomalous behavior of silica glass [JEB 13b]. This reflects the tremendous diversity of problems to which discrete element modeling can be applied and the ever-increasing availability of DMs. Section 1.2 gives a bird's-eye view of these methods, in order to position the one

that is used in this book; the reader can refer to [DON 09, JIN 07, JEB 14] for more detail. The common feature of these methods is that the studied material is modeled by a set of discrete elements, which can be of different shape and size. These elements interact with each other by contact laws and/or cohesive bonds whose type is directly dictated by the physics of the material being modeled. Knowing forces and torques applied on the discrete elements, displacements and rotations can be computed using the Newton's second law. For practical purposes, it would be often beneficial to express these results in terms of homogeneous macroscopic variables (e.g. strains and stresses). This allows us, for example, to compare the numerical results with experimental ones. Several techniques have been developed to assess macroscopic quantities from the discrete variables (e.g. force, displacement, etc.). The most commonly used techniques are detailed in section 1.4.

1.2. Classification of discrete methods

According to the analysis scale, the DMs most commonly used in numerical simulation can be classified into three classes: quantum mechanical (or *ab initio*) methods (QMMs), atomistic methods (AMs) and mesoscopic DMs (MDMs) (Figure 1.1).

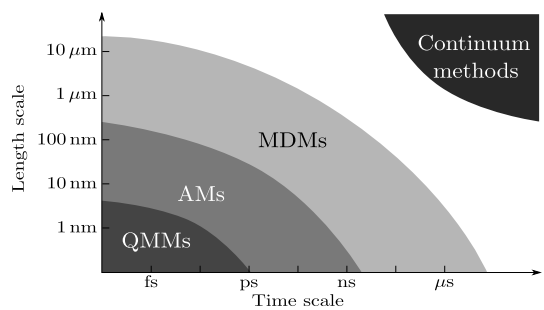

Figure 1.1. *Characteristic length scales and time scales for numerical methods*

1.2.1. *Quantum mechanical methods*

The QMMs are used for material simulation at the atomic scale ($\sim\ 10^{-9}$ m), in which the electrons are the players (Figure 1.1). The molecules are treated as collections of nuclei and electrons whose interaction is directly dictated by their QM state, without any reference to "chemical bonds". These methods all ultimately stem from the Schrödinger equation first brought to light in 1925. The fully time-dependent form of this equation for a single particle p (e.g. electron) is expressed as:

$$\left[-\frac{\hbar}{2m^p}\left(\nabla^2+\Phi\left(\mathbf{r}^p,t\right)\right)\right]\Psi\left(\mathbf{r}^p,t\right)=i\hbar\frac{\partial\Psi\left(\mathbf{r}^p,t\right)}{\partial t} \qquad [1.1]$$

where m^p and $\mathbf{r}^p$ are, respectively, the mass and position vector of the particle of interest, t designates the time, Φ is an external field (e.g. elecrostatic potential), ∇^2 is the Laplacian, $\hbar$ is Plank's constant divided by 2π, i is the square root of -1 and Ψ is the wave function which characterizes the particle motion. In fact, the wave function Ψ can properly be obtained for all the particles within a system, which, for crystalline materials, is actually reduced to the primitive unit cell because of translational symmetry. However, equation [1.1] needs this function to be expressed for individual particles. To get around this, the technique most commonly used is to write the overall wave function as a product of single-particle wave functions (the Slater determinant) and then to recast the underlying Schrödinger equation in terms of these functions. Solving this equation gives the particle motions, which in turn give the molecular structure and energy among other observables, as well as information about bonding. The challenge in developing QMMs is that such an equation can be solved exactly only for few problems, e.g. one-electron system (the hydrogen atom), and approximations need to be made. The approximation commonly used is the so-called "Hartree–Fock" which consists of replacing the "correct"

description of particle (electron) motions by a picture in which the particles behave essentially as independent bodies. Several other approximations can be found in the literature. These approximations constitute the main difference between QMMs. Examples of these methods are quantum Monte Carlo (QMC) [FOU 01] and quantum chemistry (QC) [SZA 89]. These methods allow us to treat electrons explicitly and accurately, which makes them very accurate but computationally too demanding to handle more than a few tens of electrons. Other QMMs are density-functional theory (DFT) and local density approximation (LDA) [HOH 64, PAY 92]. In these approaches, the primary Schrödinger equation is expressed in terms of particle density rather than the wave functions. Although they are less accurate than QMC or QC, these methods can be readily applied to systems containing several hundred atoms for static properties. Dynamic simulations with DFT and LDA are usually limited to timescales of a few picoseconds.

Overall, the QM methods are generally very accurate since they hold out the possibility of performing simulations without need for prior tuning. However, they are extremely expensive and can only be applied on very small domains a few nanometers in size. Indeed, they deal with electrons in a system and, even if some of the electrons are ignored (as in the semi-empirical approaches), a large number of particles must still be considered.

1.2.2. *Atomistic methods*

The AMs are used for material simulation at the microscopic scale ($\sim 10^{-6}$ m), where atoms are the players (Figure 1.1). These methods ignore the electronic motions and compute the energy of a system as a function of the atomic positions only. This way to compute energy derives its legitimacy from the Born–Oppenheimer approximation, which postulates that the electrons adjust to the new atomic

positions much faster than the atomic nuclei. The interaction laws between particles (atoms) can be described by empirical interatomic potentials that encapsulate the effects of bonding (mediated by electrons) between them. These potentials may depend on the distance between particles, angles between bonds, angles between planes, etc. Equation [1.2] gives the general form of these potentials:

$$\begin{aligned}\Phi(\mathbf{r}1, \mathbf{r}2, ..., \mathbf{r}N) = &\sum p\Phi1(\mathbf{r}p) + \sum p \sum q,\ q > p\Phi2(\mathbf{r}p, \mathbf{r}q) \\ &+ \sum p \sum q,\ q > p \sum m,\ m > q\Phi3(\mathbf{r}p, \mathbf{r}q, \mathbf{r}m) \\ &+ ... \end{aligned} \quad [1.2]$$

where $\mathbf{r}^p$ is the position vector of a particle (atom) p, N is the total number of particles, Φ_1 is the one-particle part of Φ (due to external field or boundary conditions) and Φ_2 and Φ_3 are, respectively, the two-particle and three-particle parts of Φ due to interaction between particles. The interatomic potentials may include several parameters which can be obtained by calibration using experimental data or from QM calculations. When only Φ_2 parts are present, the associated Φ is called the pair potential, e.g. Hard sphere potential and Lennard–Jones potential. The Hard sphere potential (Figure 1.2a) is the simplest part (without any cohesive interaction) and is generally used in the theoretical investigation of some idealized problems:

$$\Phi(l^{pq}) = \begin{cases} \infty \text{ for } l^{pq} \leq l_0 \\ 0 \quad \text{for } l^{pq} > l_0 \end{cases} \quad [1.3]$$

where $l^{pq} = \|\mathbf{r}^q - \mathbf{r}^p\|$ is the distance between two particles p and q and l_0 is the cutoff distance. The Lennard–Jones potential (Figure 1.2b) is more complex and more realistic to

model some physical interactions, such as the van der Waals interaction in inert gases and molecular systems:

$$\Phi(l^{pq}) = 4\varepsilon \left[\left(\frac{\sigma}{l^{pq}} \right)^{12} - \left(\frac{\sigma}{l^{pq}} \right)^{6} \right] = \varepsilon \left[\left(\frac{l_m}{l^{pq}} \right)^{12} - 2 \left(\frac{l_m}{l^{pq}} \right)^{6} \right] \quad [1.4]$$

where ε is the depth of the potential well (the region surrounding the potential minimum), σ is the finite distance at which the interparticle potential is zero and l_m is the distance at which the potential reaches its minimum. Several papers providing the Lennard–Jones parameters for some molecular systems can be found in the literature [ASH 76, HAL 75]. The pair interatomic potentials are currently the most commonly used because of their simplicity and their relatively good ability to model several molecular systems. However, in some complex problems, more sophisticated many-body potentials (including Φ_3 and higher terms) are required to correctly reproduce the involved interaction mechanisms. Knowing the interatomic potential Φ, the loadings acting on the particles (atoms) can be obtained. Then, Newton's second law can be applied to find the motions of these particles. This is the key idea of the AMs. Examples of these methods are molecular mechanics (statics) (MM) [HEH 03], molecular dynamics (MD) [ALD 57, ALD 59] and MC [MET 49], which are widely used in molecular simulation.

Although they are less accurate than the QMMs, the AMs are relatively inexpensive (compared to QMMs) and are able to provide insight into atomic processes involving considerably large systems of up to 10^9 atoms [ABR 02]. Nevertheless, dynamic simulation with AM methods is generally limited to timescales of a few nanoseconds, which can be crippling for the simulation of realistic mechanical problems.

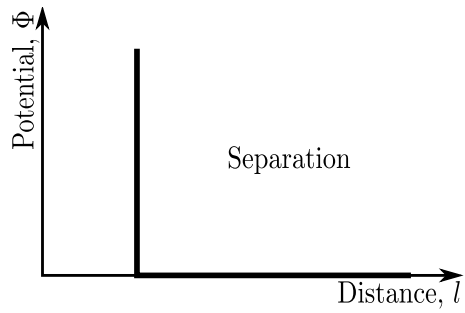

(a) Hard sphere potential

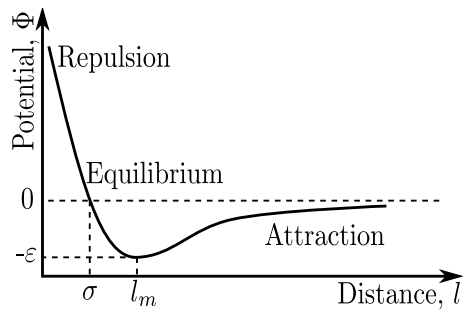

(b) Lennard–Jones potential

Figure 1.2. *Examples of pair potentials*

1.2.3. *Mesoscopic discrete methods*

To overcome the timescale limitations of the QMMs and the AMs, another generation of DMs has been developed: MDMs. The MDM methods can be used for material simulation at the mesoscopic scale ($\sim 10^{-4}$ m), where lattice defects such as dislocations, crack propagation and other microstructural elements are the players. At this scale, the system is too small to be regarded as a continuum and too large to be simulated effectively using QMMs or AMs. More accurately, the mesoscopic scale can be defined as an intermediate scale at which the microscopic phenomena (e.g. particle motions) can be assumed in mechanical equilibrium, but cannot be described by continuum mechanics. The MDMs

can broadly be regarded as a generalization of the AMs, where more complex interaction laws are used. These interaction laws are usually derived by calibration or from phenomenological theories that encompass the effects of interactions between atoms. In MDMs, the atomic degrees of freedom are not explicitly treated and only larger-scale particles are modeled. Originally, this class of methods was developed to model movements within granular materials in rock mechanics [CUN 71]. Subsequent works have extended this class to study damage in various geometricals such as concrete [HEN 04b] and rocks [BOB 09]. More recently, attempts to apply this class of method on continuous materials (continua), such as ceramics [TAN 09] and glasses [AND 13, JEB 13b, JEB 13a, AND 12b], have emerged. In these attempts, the continuum is also modeled by an agglomerate of discrete elements (particles or nodes) which interact via bilateral cohesive links to ensure the material cohesion. Different cohesive links are tested according to the physical properties of the studied material. Figure 1.3 illustrates an example of a continuum modeled by the MDM method. As will be seen in Chapter 2, the application of MDMs methods in modeling of continua must respect certain geometric and mechanical rules.

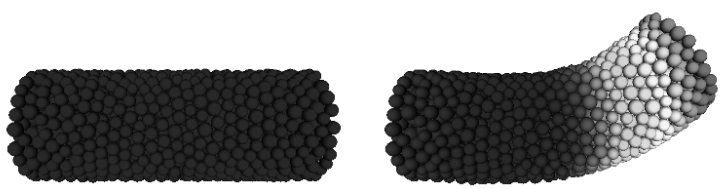

(a) Relaxing state (b) Loading state

Figure 1.3. *MDM modeling of a continuum. For a color version of the figure, see www.iste.co.uk/jebahi/discrete.zip*

Nowadays, the MDMs present an alternative method to study realistic complex problems, for which continuity assumption is not valid, or problems with discontinuities that cannot easily be treated by CMs, such as cracking behavior of silica glass [AND 13, JEB 13b, JEB 13a, AND 12b]. The benefits of these methods have attracted several researchers, and consequently, several variations of MDMs have been developed. These variations can be divided into four categories as shown in Figure 1.4. The fundamental concepts of each one are briefly recalled hereafter.

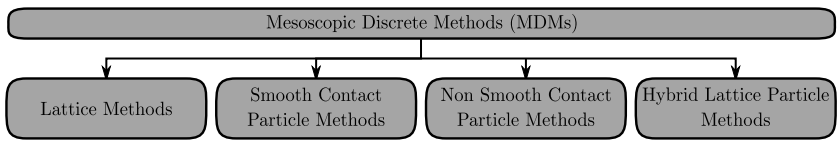

Figure 1.4. *Classification of mesoscopic discrete methods (MDMs)*

1.2.3.1. *Lattice methods*

In lattice models, a solid is modeled by a set of nodes connected with truss or beam elements [SCH 92a, SCH 92b] (Figure 1.5). Typically, nodes have neither masses nor volumes (they do not occupy volumes). Solving a mechanical problem with this class of DMs is based on the construction of a global stiffness matrix $\mathbf{K}$ from the local connection properties. Knowing this matrix, the displacements $\mathbf{u}$ and rotations $\boldsymbol{\theta}$ at the nodes can be obtained for static analysis by solving:

$$\mathbf{K}\,\mathbf{X} = \mathbf{b} \qquad [1.5]$$

where $\mathbf{X}$ is the vector of the problem unknowns which includes both displacements and rotations of all the nodes and $\mathbf{b}$ is the loading vector which includes forces and torques in the beams. Both regular and irregular lattices were studied. Originally, the lattice models were used to represent elastic continuum; the equivalence was established for both

truss [HRE 41] and beam [SCH 96] elements. Later on, obvious enhancements, such as brittle beam failure, were introduced. Lattice models nicely show the emergence of relatively complex structural behaviors, although fairly simple formulas are used to describe the governing local processes.

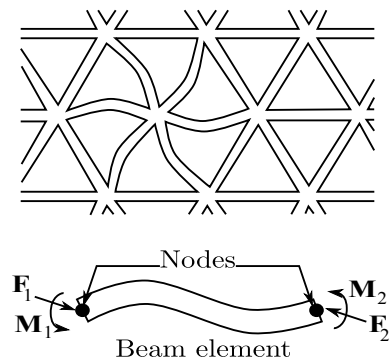

Figure 1.5. *2D regular triangular lattice of beams (inspired by [SCH 92a])*

Lattice models have shown a great ability to model fracture in continuous materials. Schlangen *et al.* [SCH 97] pointed out that using beam elements (forces and torques are considered), the crack pattern is quite close to the experimentally observed pattern. The same authors [SCH 97] emphasized the importance of the beam torques, without which the crack behavior may be entirely unacceptable. The major drawback of these models is that the nodes do not have volumes, which can cause numerical problems related to crack closure in postfracture stage. To circumvent this problem, Ibrahimbegovic *et al.* [IBR 03] have proposed to associate fictitious equivalent volumes with the nodes, based on the spatial Voronoï decomposition. However, this solution is generally time-consuming, especially in the case of large three-dimensional (3D) problems.

1.2.3.2. *Smooth contact particle methods*

This class of methods is very close to the first discrete approach proposed in the literature by Cundall and Strack [CUN 71, CUN 79]: distinct (discrete) element method (DEM). Contrary to lattice models, particle models consider elements with masses and volumes in interaction through contact laws. These elements often have a disk shape (in two-dimensional (2D)) or spherical shape (in 3D): only one parameter (the radius) is required to determine the geometry of elements and there is only one possible contact easily detectable between them. Consequently, computer memory requirements and processing time are minimized with these element shapes, even when a relatively large number of elements are used. Nevertheless, discs and spheres can roll or rotate easily. This does not reflect the expected behavior for several materials, for example, in the case of large shear processes. To solve this problem, more complex shapes such as ellipses [TIN 93], ellipsoids [LIN 97], polygons [ISS 92] and polyhedra [CUN 88] were proposed in the literature to provide more flexibility for element characterization in particle models.

Basically, the associated algorithm involves two stages. In the first stage, interaction forces are computed when elements slightly interpenetrate each other. This force-interpenetration formulation is generally referred to as a "smooth contact" method or "force–displacement" method. Actually, the interpenetration between discrete elements, which makes no mechanical sense, represents the relative deformation of the surface layers. In the second stage, Newton's second law is applied to determine the acceleration of each element, which is then integrated, using "*dynamic explicit*" schemes, to find the new velocities and positions of elements. This process is repeated until the simulation is achieved.

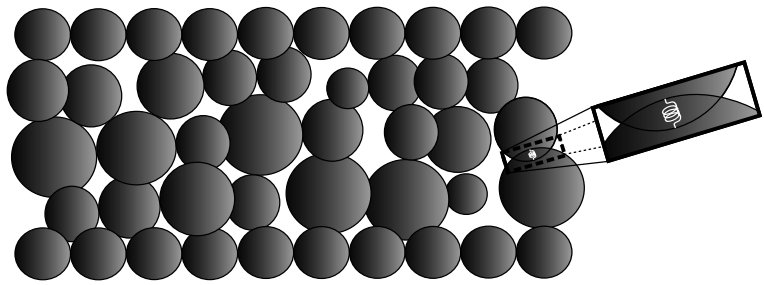

Figure 1.6. *2D smooth contact particle model*

1.2.3.3. *Non-smooth contact particle models*

Despite the great success of the smooth contact particle models to simulate a wide variety of complex systems, there are cases for which they are less appropriate:

– in systems where the typical duration of a collision is much shorter than the mean time between successive collisions of a particle. Therefore, the pairwise collisions of particles may be considered as instantaneous events;

– in systems where the contact laws between particles cannot easily be determined as a function of the relative position, velocity and orientation; however, information about postcollision velocities is accessible from the precollision conditions (e.g. by using experimental techniques);

– in systems where the particles are very rarely in contact with more than one other particle.

To allow a better investigation of such systems, another class of DMs has been developed. This class provides an alternative approach based on a "non-smooth" formulation of mutual exclusion and dry friction between elements [JEA 99, LUD 96, MOR 94]. It introduces the notion of non-smooth (irregular) contact between elements which is, at present, the subject of several studies. Interpenetration between elements is prevented: no elastic contact laws are used between them.

Mainly, two classes of numerical integrators exist for non-smooth contact methods; both of them are of the "*dynamic implicit*" type: the event-driven integrators, also referred to as the event-driven method (EDM) [LUD 96], and the time-stepping integrators, also referred to as the contact dynamics method (CDM) [JEA 99, MOR 94]. In EDM, a collision or "event" occurs when two rigid elements touch each other and the postcollisional and angular velocities are prescribed by a collision operator [RAP 80]. Despite being very accurate, the event-driven integrators treat only one force at a time. Therefore, they are not well adapted for problems with many simultaneous contacts, as often encountered in mechanics. To overcome this limitation, Jean and Moreau [JEA 99, MOR 88] have developed the CDM which has a specialized numerical scheme for problems with many contacts. The governing equations are expressed as differential inclusions (multivalued differential equations) and the accelerations are replaced by velocity jumps. In the generic CDM algorithm, an iterative process is used to compute forces and velocities. This process consists of solving a single contact problem with all other contacts kept constant, and iteratively updating the forces until a convergence criterion is fulfilled. Two basic kinematic constraints are used between elements in the CDM formulation:

– the *Signorini conditions* which state that the normal force f_n is repulsive when the elements are in contact (distance between them is zero), and $f_n = 0$ otherwise. To deal with persistent contacts, f_n is reset to zero when no relative velocity exists between elements in contact;

– *Coulomb's friction law*, which relates the sliding particle velocities and the friction forces f_t.

These kinematic constraints can also be complemented by a "*rolling friction*" constraint which introduces a moment resistance [BRA 02]. Within the CDM, the time resolution is much larger than the collision characteristic time (unlike in

the case of smooth contact approaches). Therefore, the time step represents a unit of time during which collisions can occur, causing velocity jumps. Although CDM has successfully been used for several geomechanical problems [DON 09], it is much more difficult to implement than the DMs based on smooth contact. Also, the prediction of the contact forces and particle velocities in the following time step from the current configuration is very problematic and is currently the subject of several studies.

The non-smooth contact models are generally used to study quasi-static problems or problems with relatively low dynamic effects. This class of methods is perfectly suitable to study mechanical problems of granular mechanics. However, in the case of continuous media, the use of models based on regular or "smooth" interaction laws seems to be advantageous since the elasticity is naturally taken into account by these interaction laws.

1.2.3.4. *Hybrid lattice-particle models*

As seen earlier, the features and advantages of the lattice and particle models are largely complementary. Indeed, the particle methods cannot correctly model a continuum using a simple disk of spherical elements, especially when significant shear effects are involved. This problem can be solved using cohesive beams between elements, such as in lattice models. On the other hand, particle methods can correctly deal with crack closure in postfracture stage, since elements have their own volumes. However, additional treatment must be made to simulate this phenomenon by using lattice models. Therefore, it would be beneficial to combine these models, in order to strengthen their advantages and overcome their drawbacks. This idea has attracted a strong research effort which has given rise to the class of hybrid lattice-particle methods. This class merges the main features of the combined models, i.e. by considering sphere elements connected with cohesive beams [GRI 01] (Figure 1.7).

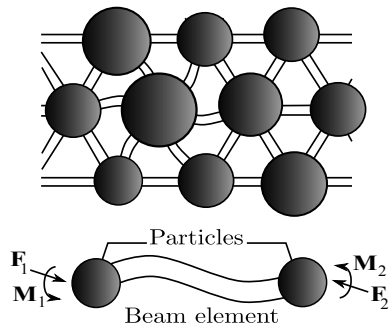

Figure 1.7. *2D hybrid lattice-particle model*

1.3. Discrete element method for continuous materials

As seen in the previous section, the DMs are classified into three classes: QMMs, AMs and MDMs. The first two classes are adapted for very fine-scale problems for which continuum description is not possible. Application of these classes to study continuous materials whose scale of interest is much greater than the interatomic distance is extremely time-consuming or even crippling. The MDMs are used to study the problems at the mesoscopic scale which is the scale of interest for most of the complex phenomena that are encountered in continuum simulation, but cannot correctly be treated by CMs. Compared to QMMs and AMs, these methods are relatively inexpensive and seem to be the most adapted to simulate continuous materials. Mainly, four categories of MDMs can be distinguished. The category of non-smooth contact methods is based on a non-smooth formulation between particles. This formulation can be perfectly adapted for granular materials; however, it is inappropriate to study continuous materials. In effect, the use of models based on regular or "smooth" interaction laws seems to be advantageous for these materials since their mechanical behavior can naturally be taken into account by the smooth interaction laws. Except for the non-smooth contact methods, all MDM categories present this feature (of

smooth interaction between particles) and seem *a priori* candidates to model continuous materials. Among them, the category of hybrid lattice-particle methods has practically all the advantages of the MDM categories with regard to continuum simulation, while alleviating their drawbacks. The use of a DM in this category to model continua is thereby justified. Specifically, this book focuses on the variation of DMs recently developed by André *et al.* [AND 12b, AND 13, JEB 13b, TER 13, JEB 13a]. This method models a continuum by a set of spherical particles linked by 3D cohesive beams. The main specificities and features of this method will be detailed later.

1.4. Discrete-continuum transition: macroscopic variables

In the framework of discrete element modeling, results of a mechanical problem are given in terms of forces and torques acting on particles, and their corresponding displacements and rotations. However, in order to compare these results with macroscopic experiments or theories, it is useful to assess macroscopic quantities from these results. This is the subject of several works which aim to establish a correspondence with continuum theories by computing macroscopic tensorial quantities, e.g. stress tensor σ and strain tensor ε, as well as other scalar properties, e.g. bulk and shear moduli [GOD 86, KRU 96, LIA 97]. These macroscopic quantities can even be applied to enrich some criteria used in discrete element modeling. As will be shown in Chapter 4, fracture criteria based on a stress tensor allow us to reproduce the cracking mechanisms much better than the traditional criteria based on the forces or displacements. The major challenge in obtaining these quantities is that, in some variations of DMs, the particles have additional degrees of freedom (rotations) which are not taken into account in classical continuum theories. To account for rotation effects, it is necessary to develop a consistent size-dependent

continuum theory able to account for the microstructure of materials. This theory must span many scales and, of course, reduce to classical theories for the macroscopic scale. More accurately, new length-related measures of deformation, such as the curvature tensor, are needed in a more complete continuum theory. As a result, this theory also requires us to introduce the notion of couple stress which was originally proposed by Voigt in 1887 [VOI 87]. Several attempts have been developed in the literature to establish such a theory [TOU 62, CHE 01, LEO 02, HAD 11, COS 09]. However, these attempts, with their numerous difficulties, fall far short of providing a solid formulation workable in practice [ERI 68, MIN 62, HAD 11].

In the remainder of this section, approaches used to compute stress and strain tensors will be briefly reviewed, while remaining within the framework of classic continuum theories. The contribution of couple stress will then be ignored in this review. Furthermore, the phenomena related to the kinematics of the particles and having no equivalent in continuum will not be considered. This does not mean ignoring the particle rotations, only phenomena associated with no dissipated or stocked energy are ignored, e.g. loss contact or rolling without sliding. According to several papers [CAI 95, MOR 97, AND 13, BAG 06, CAM 09], these approaches lead in a first approximation to an acceptable estimate of these tensors. For the sake of clarity, unless there is a need for index form, equations in the following will be given in matrix form. Moreover, tensors will be replaced by their corresponding matrices in the equations.

1.4.1. *Stress tensor for discrete systems*

Within the framework of classic continuum theories, the most commonly used definition of stress in DMs is the virial stress. This stress, also called system-level stress, is based on a generalization of the virial theorem of Clausius developed

in 1870 for gas pressure. In the original definition [MCL 74, TSA 79, SWE 83], the average virial stress over a volume V around a particle p is given by:

$$\bar{\boldsymbol{\Pi}} = \frac{1}{V}\left(-m^p\,\dot{\mathbf{u}}^p \otimes \dot{\mathbf{u}}^p + \frac{1}{2}\sum_{q\neq p}\mathbf{l}^{pq} \otimes \mathbf{f}^{pq}\right) \qquad [1.6]$$

where m^p is the mass of p, $\dot{\mathbf{u}}^p$ is the velocity of p (material time derivative of the displacement $\mathbf{u}^p$, $\dot{\mathbf{u}}^p = d\mathbf{u}^p/dt$), $\mathbf{l}^{pq} = \mathbf{r}^q - \mathbf{r}^p$ is the vector linking the centers of particles p and q, $\mathbf{r}^p$ is the position vector of p, $\mathbf{f}^{pq}$ is the force applied on p by particle q, "$\otimes$" denotes the tensor product and the summation runs over all the particles in V. The sign convention for solid mechanics is used in the virial stress relation [1.6], i.e. the stress is negative in compression and positive in extension. This relation includes two parts. The first part depends on the mass and velocity (or in some versions the fluctuations of velocity) of the particles, reflecting that the mass transfer through a fixed spatial surface causes mechanical stress on this surface. The second part depends on the interparticle forces and particle positions, providing a continuum measure for the internal mechanical interactions between particles.

The virial stress as defined in [1.6] has widely been used in the past to compute an equivalent to Cauchy stress in discrete systems. Recently, Zhou [ZHO 03] has demonstrated that, contrary to what was believed by some investigators, this quantity is not a measure for the mechanical forces between material points and cannot be regarded as a measure of mechanical stress in any sense. The lack of physical significance is both at the microscopic level (particle level) and macroscopic level (system level). This author has shown that only the second part of the virial stress can be identified with the Cauchy stress. The details of the proof can

be found in [ZHO 03]. Therefore, the average stress in a region of volume V as given by Zhou is:

$$\bar{\boldsymbol{\sigma}} = \frac{1}{2\,V} \sum_{p} \sum_{q \neq p} \mathbf{l}^{pq} \otimes \mathbf{f}^{pq} \qquad [1.7]$$

Originally, expressions [1.6] and [1.7] were developed for MD where the interparticle forces are derived from a functional Φ (e.g. Lennard–Jones potential [1.4]) as follows:

$$\mathbf{f}^{pq} = \frac{\partial \Phi(\mathbf{l}^{pq})}{\partial l^{pq}} \frac{\mathbf{l}^{pq}}{l^{pq}} \qquad [1.8]$$

where $l^{pq} = \|\mathbf{l}^{pq}\|$ represents the distance between particles p and q. In this instance, expressions [1.6] and [1.7] lead to symmetric tensors. However, this cannot be generalized to all DMs. To analyze the symmetry of the stress tensor [1.7] for the general case, the approach proposed by Chapuis [CHA 76] for quasi-static analysis can be used.

For quasi-static study, the resultant torque on a particle p must vanish:

$$\sum_{q \neq p} \mathbf{l}^{pq} \wedge \mathbf{f}^{pq} = 0 \qquad [1.9]$$

which is equivalent to:

$$\sum_{q \neq p} l_i^{pq}\, f_j^{pq} - l_j^{pq}\, f_i^{pq} = 0, \quad \forall\, i,\, j \in [1..3] \qquad [1.10]$$

Therefore,

$$\sum_{q \neq p} \mathbf{l}^{pq} \otimes \mathbf{f}^{pq} = \sum_{q \neq p} \mathbf{f}^{pq} \otimes \mathbf{l}^{pq} \qquad [1.11]$$

If the volume V, in which the stress tensor is computed, includes all the particles of the studied system (i.e. the volume

boundary does not cut any particle), equation [1.9] is true for each of these particles. Therefore, the following relation can be obtained:

$$\sum_{p}\sum_{q\neq p} \mathbf{l}^{pq} \otimes \mathbf{f}^{pq} = \sum_{p}\sum_{q\neq p} \mathbf{f}^{pq} \otimes \mathbf{l}^{pq} \qquad [1.12]$$

which proves the symmetry of the stress tensor given by [1.7]. However, if some particles are cut by the boundary of the considered volume, equation [1.9] is not valid for these particles. In this case, the symmetry of the stress tensor [1.7] is not guaranteed. However, if the volume V is large enough, the number of particles cut by the volume boundary is small with respect to the total number of particles in V. The associated stress tensor can therefore be considered as symmetric [CAI 95, MOR 97].

For dynamic study, the above analysis can also be followed when the particle forces are symmetrically applied around each particle center (as in regular assemblies). In this case, no particle torques are induced on the particles, and then equation [1.9] remains valid. If the particle forces are not highly unsymmetrical, the corresponding stress tensor can be assumed to be symmetric. Otherwise, the symmetric part of [1.7] can be used to compute an approximated stress tensor in discrete systems [AND 13, JEB 13b]:

$$\bar{\boldsymbol{\sigma}} = \frac{1}{2\,V}\sum_{p}\sum_{q\neq p}\frac{1}{2}\,(^{pq} \otimes \mathbf{f}^{pq} + \mathbf{f}^{pq} \otimes \mathbf{l}^{pq}) \qquad [1.13]$$

1.4.2. *Strain tensor for discrete systems*

The micromechanical interpretation of a strain tensor in discrete systems has been the subject of strong scientific interest in recent years. Consequently, several approaches have been proposed to this end. All these approaches are based on the assumption of small displacements of the

particles. Most of them are derived either from equivalent continuum computations or using best-fit methods. A brief review of the approaches commonly used is given hereafter; the reader is referred to [BAG 06, CAM 09] for more details. Only 3D domains are considered in this review, but almost all the reviewed approaches can also be used for 2D analysis. Let Ω_D denote the discrete region (made up of N particles) in which the strain tensor would be computed.

1.4.2.1. *Equivalent continuum strains*

These microstructural strains are based on the equivalent continuum technique. The discrete region Ω_D is replaced by an equivalent continuous domain, to which a displacement field is assigned such that the displacements of the continuum nodes (associated with the equivalent continuous domain) are equal to those of the particle centers. The strain tensor can then be determined from the gradient of this field, and expressed in terms of the particle displacements and the geometrical characteristics of the discrete model. Several approaches based on this technique can be found in the literature [BAG 93, BAG 96, KUH 99, CAM 00, KRU 03, KRU 96], some of which are studied and compared in [CAM 09, BAG 06]. The main difference between them lies in the way in which the equivalent continuum is defined. One particular approach is that suggested by Bagi [BAG 93, BAG 96], which can be regarded as a generalization of the first approach developed by Rothenburg in his PhD dissertation in 1980 for 2D analysis [ROT 80]. This approach is valid for 2D and 3D systems with arbitrary convex shape. Only particle displacements are considered in such an approach (particle rotations are ignored). The continuous domain is constructed from the discrete system using a kind of "space cell", which is defined as tetrahedra (triangles in 2D) formed by the centers of neighboring (but not necessary touching) particles (Figure 1.8). The displacement field associated with this continuum is defined using a linear

interpolation of nodal displacements, which are, by definition, the same that the particle displacements.

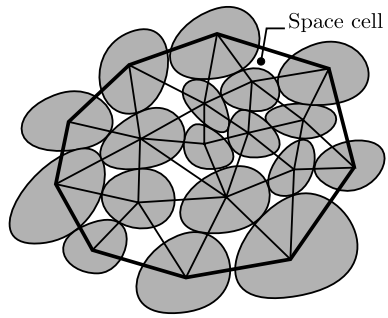

Figure 1.8. *Space cells (inspired by [BAG 06])*

Within a cell c, this displacement field is continuously differentiable, and its gradient is constant in this cell. Let $\mathbf{e}^c = \nabla \mathbf{u}$ denote the displacement gradient tensor in the cell c. The volume average of this tensor over the cell c can be expressed using a surface integral as follows:

$$\bar{\mathbf{e}}^c = \frac{1}{V^c} \oint_{S^c} \mathbf{u} \otimes \mathbf{n} \, ds \qquad [1.14]$$

where V^c and S^c are, respectively, the volume and boundary surface of the cell c, and $\mathbf{n}$ is the outward unit normal vector of S^c. Using [1.14], the volume average of the displacement gradient tensor over the whole continuum domain associated with Ω_D is given by:

$$\bar{\mathbf{e}} = \frac{1}{V} \sum_c V^c \, \bar{\mathbf{e}}^c \qquad [1.15]$$

where $V = \sum_c V^c$ is the volume of the whole continuum associated with Ω_D. To compute [1.15], Bagi [BAG 95, BAG 96] has introduced a new vector $\mathbf{d}^{pq}$ associated with the particle interactions pq (between particles p and q).

This vector is called the complementary area vector, and its derivation is detailed in [BAG 95, BAG 96]. It can be interpreted as the dual of the branch vector $\mathbf{l}^{pq}$ pointing from the center of the particle p to the center of the particle q, in the sense that the total volume of the studied domain is determined by summing the scalar products of these vectors over the total number of particle interactions pq:

$$V = \frac{1}{3} \sum_{pq} \mathbf{d}^{pq}.\mathbf{l}^{pq} \qquad [1.16]$$

Using the complementary area vector $\mathbf{d}^{pq}$, equation [1.15] can be rewritten as:

$$\bar{\mathbf{e}} = \frac{1}{V} \sum_{pq} \mathbf{u}^{pq} \otimes \mathbf{d}^{pq} \qquad [1.17]$$

where $\mathbf{u}^{pq} = \mathbf{u}^q - \mathbf{u}^p$ is the relative displacement of the centers of particles p and q. The details of the proof can be found in [BAG 95, BAG 96]. The symmetric part of the tensor $\bar{\mathbf{e}}$ defines the average strain tensor $\bar{\boldsymbol{\varepsilon}}$ in V:

$$\bar{\boldsymbol{\varepsilon}} = \frac{1}{2} \left(\bar{\mathbf{e}} + {}^{t}\bar{\mathbf{e}} \right) \qquad [1.18]$$

Several papers studying the Bagi approach can be found in the literature [BAG 06, CAM 09]. These papers conclude that this approach generally gives a good estimate of the strain tensor at the structure scale.

1.4.2.2. *Best-fit strains*

These microstructural strains are based on the best-fit technique (e.g. using the least squares method). They consist of finding the displacement gradient tensor which gives the smallest deviation from characteristic displacements of the particles in Ω_D (the discrete region in which the strain tensor would be computed). Several best-fit approaches have been proposed in the literature [CUN 79, LIA 97, CAM 00], all of

which are valid for 2D and 3D analyses. The main difference between these approaches lies in the way in which the characteristic displacements are defined, e.g. the relative displacements of the particle centers, the relative displacements at the contacts, etc. Among the first best-fit strains is the Cundall strain [CUN 79], which is widely used in the discrete element modeling and is even implemented in several well-known software packages (e.g. PFC, TURBAL, etc.). This microstructural strain is valid for particles with arbitrary shape. The approach used to obtain this strain is detailed hereafter. It should be noted that only displacements of the particle centers (particle rotations are ignored) are considered in this approach.

Let $\mathbf{x}^p$ and $\mathbf{u}^p$ be the initial position vector and displacement vector of a particle p. In the approach of Cundall, the space variables are expressed in a framework whose origin o is located at the average position of the particle centers belonging to Ω_D:

$$\mathbf{x}^o = \frac{1}{N} \sum_p \mathbf{x}^p \qquad [1.19]$$

where N is the total number of particles in Ω_D. The displacement of the Cundall framework is defined as the average displacement of the particle centers in Ω_D:

$$\mathbf{u}^o = \frac{1}{N} \sum_p \mathbf{u}^p \qquad [1.20]$$

Therefore, the vectors $\mathbf{x}^p$ and $\mathbf{u}^p$ are, respectively, replaced by $\mathbf{x}^{op}$ and $\mathbf{u}^{op}$. The vector $\mathbf{x}^{op}$ represents the relative position of individual particles with respect to $\mathbf{x}^o$:

$$\mathbf{x}^{op} = \mathbf{x}^p - \mathbf{x}^o \qquad [1.21]$$

The vector $\mathbf{u}^{op}$ represents the relative displacement of individual particles with respect to $\mathbf{u}^{o}$:

$$\mathbf{u}^{op} = \mathbf{u}^{p} - \mathbf{u}^{o} \qquad [1.22]$$

Assuming that the studied assembly deforms such that every particle displacement exactly corresponds to a uniform displacement gradient tensor $\bar{\mathbf{e}}$ (i.e. the strain tensor is assumed to be constant in Ω_D), equation [1.22] can be rewritten as:

$$\mathbf{u}^{op} = \bar{\mathbf{e}}\,\mathbf{x}^{op} \qquad [1.23]$$

because particle displacements are assumed to be small. Therefore, the Cundall approach consists of finding the tensor $\bar{\mathbf{e}}$ that gives the best fit to the relative particle displacements [1.23]. Using the least squares method, the problem is reduced to finding the optimum $\bar{\mathbf{e}}$ that minimizes S:

$$S = \sum_{p} \|\mathbf{u}^{op} - \bar{\mathbf{e}}\,\mathbf{x}^{op}\|^2 \qquad [1.24]$$

where "$\|.\|$" denotes the Euclidean norm. This last relation [1.24] can be rewritten in index form (using the Einstein summation convention) as follows:

$$S = \sum_{p} \left(u_i^{op} - \bar{e}_{ij}\, x_j^{op}\right)^2, \quad i,\, j \in [1..3] \qquad [1.25]$$

The corresponding mathematical problem is: find $\bar{\mathbf{e}}$ such that:

$$\forall\, i,\, j \in [1..3], \quad \frac{\partial S}{\partial \bar{e}_{ij}} = 0 \qquad [1.26]$$

which can be rewritten in matrix form as:

$$\mathbf{A}\,{}^{t}\bar{\mathbf{e}} = \mathbf{B} \qquad [1.27]$$

where the matrices $\mathbf{A}$ and $\mathbf{B}$ are given by:

$$\mathbf{A} = \sum_p \mathbf{x}^{op} \otimes \mathbf{x}^{op}, \quad \mathbf{B} = \sum_p \mathbf{x}^{op} \otimes \mathbf{u}^{op} \qquad [1.28]$$

As demonstrated by Bagi [BAG 05], the coefficient matrix $\mathbf{A}$ is positive-definite if and only if $n \geq 4$ and there exist at least four particles whose centers are not in the same plane. This is the necessary and sufficient condition for existence of the inverse coefficient matrix $\mathbf{A}^{-1}$, and then the existence of the Cundall strain in 3D. If $\mathbf{A}^{-1}$ exists, the best-fit displacement gradient tensor is given by:

$$\bar{\mathbf{e}} = {}^t\left(\mathbf{A}^{-1}\,\mathbf{B}\right) \qquad [1.29]$$

The Cundall strain is none other than the symmetric part of [1.29]. Based on [BAG 06, CAM 09], this microstructural strain gives relatively good results, in agreement with strain measures at the structure level.

1.4.2.3. *Satake strain*

Contrary to the Bagi and Cundall approaches, the Satake approach [SAT 04] takes into account both displacements and rotations of the particles. Such an approach shares some features with the equivalent continuum ones. Indeed, it is based on a tessellation system (space cells). However, no displacement field assigned to these cells is required, and then no cell deformations are analyzed (unlike in equivalent continuum approaches). This approach is valid for assemblies of disk or spherical particles, as in hybrid lattice-particle methods, which is of particular interest with regard to the subject of this book.

The geometrical background of the Satake strain is constructed using the generalized Dirichlet tessellation (which is also known as the Voronoï diagram) [ASH 86], whose 2D illustration is given by Figure 1.9. This tessellation

is unique for a given set of particles N, and it fills the convex hull of the particles. An individual Dirichlet cell (Voronoï cell) associated with a particle p is defined by:

$$T_p = \{\mathbf{x} |\, \|\mathbf{x} - \mathbf{x}_p\| < \|\mathbf{x} - \mathbf{x}_q\|\,,\ \forall p \neq q\} \qquad [1.30]$$

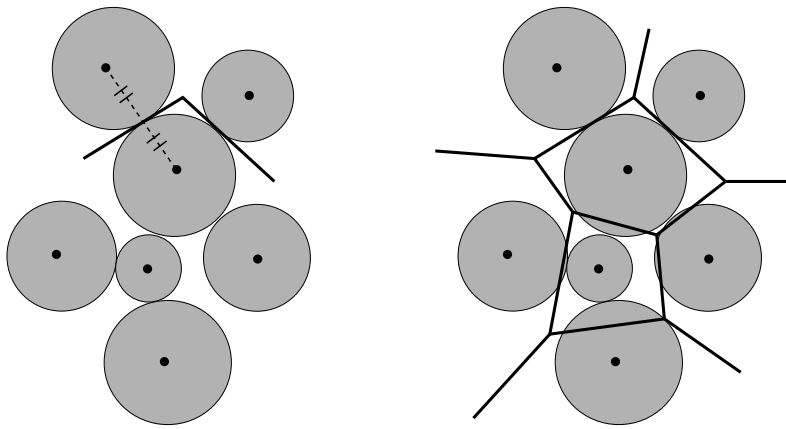

(a) Construction of generalized Dirichlet tessellation

(b) Generalized Dirichlet tessellation

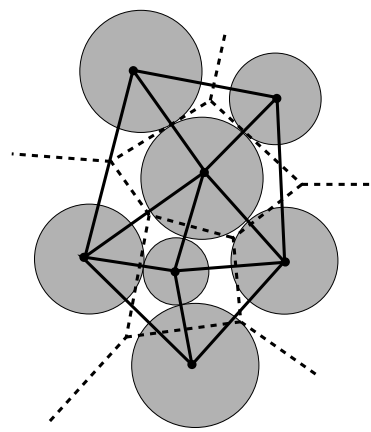

(c) Delaunay tessellation

Figure 1.9. *Geometric construction of the generalized Dirichlet tessellation and the associated Delaunay tessellation for a set of particles in 2D*

Using [1.30], the generalized Dirichlet tessellation P can be obtained:

$$P = \{T_p | \, p \in [1..N]\} \qquad [1.31]$$

After construction of P, the Delaunay tessellation (Figure 1.9c) can be formed by the branches connecting the centers of the particles which have a common face in P. This allows us to define the neighboring particles: every two particles p and q linked by a Delaunay branch are considered as neighbors. Then, the contact cells can be defined, based on the generalized Dirichlet tessellation and the associated Delaunay network, such that one contact cell is defined per pair of neighboring particles. The contact cell associated with the pair of particles (p and q) will be denoted by pq. For each pq, two vectors are introduced: branch vector $\mathbf{l}^{pq}$ linking the centers of the neighboring particles p and q and the dual branch vector $\mathbf{d}^{pq}$, whose direction is perpendicular to the Dirichlet face between these particle and magnitude is equal to the area of this face. The volume of this cell can be obtained using these two vectors as:

$$V^{pq} = \frac{1}{3} \mathbf{d}^{pq}.\mathbf{l}^{pq} \qquad [1.32]$$

After long and complicated calculations which can be found in [SAT 04], Satake has shown that the volume average of the displacement gradient tensor over the whole considered domain is defined by:

$$\bar{\mathbf{e}} = \frac{1}{V} \sum_{pq} \mathbf{c}^{pq} \otimes \mathbf{d}^{pq} \qquad [1.33]$$

where $V = \sum_{pq} V^{pq}$ is the volume of the whole domain and $\mathbf{c}^{pq}$ is the contact deformation defined as the relative displacement, between two particles p and q, expressed at the contact point c.

This quantity can be determined using particle displacements ($\mathbf{u}^p$ and $\mathbf{u}^q$) and the particle rotations ($\boldsymbol{\theta}^p$ and $\boldsymbol{\theta}^q$) as follows:

$$\mathbf{c}^{pq} = \{\mathbf{u}^q\}_c - \{\mathbf{u}^p\}_c = (\mathbf{u}^q + \boldsymbol{\theta}^q \wedge \mathbf{r}^{cq}) - (\mathbf{u}^p + \boldsymbol{\theta}^p \wedge \mathbf{r}^{cp}) \qquad [1.34]$$

where $\{\mathbf{u}^p\}_c$ is the displacement of the particle p expressed at the contact point c, $\mathbf{u}^p$ is the displacement of the center of the particle p, $\boldsymbol{\theta}^p$ is the rotation of a particle p, $\mathbf{r}^{cp}$ is a vector pointing from the center of the particle p to the contact (boundary) point c and "$\wedge$" denotes the vector product. The symmetric part of $\bar{\mathrm{e}}$ represents the Satake strain.

As can be seen from [1.17] and [1.33], the Satake strain expression is similar to that obtained by Bagi. One difference is that the dual branch vector is used in place of the so-called complementary area vector in the Bagi definition. This is due to a difference in the definition of the geometrical background of two microstructural strains. The generalized Dirichlet tessellation is used to obtain the Satake strain, which allows us to properly define a geometric background that takes into account the particle size. This makes the geometrical explanation more simple and clearer so that a systematic analysis becomes easy both in 2D and 3D analyses. Another difference between the strain definitions is that the Bagi definition is based upon relative displacements between the particle centers, whereas relative displacements at the contact points are considered for the Satake definition. This allows us to take into consideration the particle rotations in the computation of the microstrutural strain. Numerical comparison of these two definitions of microstructural strain shows that they give similar results, which are in good agreement with the strain measured at the structure level [BAG 06, CAM 09]. This can reflect that the contribution of the particle rotations is not of major importance in the computation of the strain tensor.

1.5. Conclusion

This chapter provides a brief review of discrete element modeling. A classification of the DMs most commonly used to model physical systems is given, in order to place the DEM proposed in this book. Depending on the analysis scale, three classes can be distinguished: QMMs, AMs and MDMs. The first two classes are extremely time-consuming and can be applied only to simulate very small-scale problems. The MDMs are used to simulate problems at the mesoscopic scale, which is the scale of interest of most of the complex phenomena encountered in continuum modeling (i.e. by using CMs). Therefore, this class provides an alternative method to model such phenomena. MDM methods are generally made up of four categories: lattice methods, smooth contact particle methods, non-smooth contact particle methods and hybrid lattice-particle methods. The non-smooth contact particle methods are based on the non-smooth formulation between particles. Such a category is rather adapted for granular materials. The other categories are based on the smooth particle interactions, and then come forward as candidates to model continuous problems. Indeed, the mechanical behavior of these materials can naturally be taken into account by such interactions. In particular, the category of hybrid lattice-particle methods has practically all the advantages of the MDM methods with regard to modeling of continuous materials. This is why a hybrid lattice-particle method is chosen to model continua in this book. The main features of this method will be detailed in the next chapter. The results of such a method and the DMs, in general, are given in terms of discrete particle loadings (forces and torques) and their corresponding particle motions (displacements and rotations). These results are strongly heterogeneous: their size and magnitude may significantly vary from particle to particle. Therefore, they cannot be estimated as continuously differentiable fields. Establishing a link between particle-level results and structure-level stresses and strains

is important to interpret these results from a macroscopic point of view. The second part of this chapter gives some analytical and numerical techniques used to bridge these levels. As will be seen in Chapter 4, these techniques are also useful to enrich the criteria applied in discrete element modeling.

2

Discrete Element Modeling of Mechanical Behavior of Continuous Materials

2.1. Introduction

The mechanical behavior of continuous materials is usually simulated by continuum approaches like the finite element method (FEM). However, simulation of discontinuous phenomena like multifracturing is not well-adapted to continuum description. In this case, as seen in Chapter 1, the hybrid lattice-particle methods are a good alternative because they naturally take into account discontinuities. Many researchers have shown the interest in these approaches for wear and fracture simulation. The problem is that, while hybrid lattice-particle methods are well-adapted to simulate discontinuities, they are not suitable for simulating continuous behaviors because continuum mechanics laws cannot be used directly within the formulation of these approaches.

The aim of this chapter, and those which follow, is to introduce and develop a new variation of hybrid lattice-particle methods that tackles these theoretical difficulties to facilitate quantitative simulation of the following mechanical

Discrete Element Method to Model 3D Continuous Materials, First Edition.
Mohamed Jebahi, Damien André, Inigo Terreros and Ivan Iordanoff.

and thermal behaviors: elastic, brittle fracture and thermal conduction. In accordance with what is collectively used, in the following, this variation will simply be called the discrete element method (DEM). Unless explicitly stated, to this name will be used to refer to this variation. An illustration of the main features of this method is given in Figure 2.1, where:

Figure 2.1a illustrates a discrete domain made up of spherical discrete elements connected by cohesive bonds. These bonds are symbolized in this figure by springs. This discrete domain models a sample of cohesive solid characterized by its mechanical behavior: elasticity, failure, etc.

Figure 2.1b illustrates the sample in a deformed state caused by an external force. To simulate the failure of the continuum, a criterion is introduced at the bond level. Generally, this criterion is given in terms of maximal strain or stress in the bonds. If a bond reaches this criterion, it is deleted. In this example, a bond, near the clamped face, is deleted.

Figure 2.1c illustrates the domain that comes back to the initial state. The deleted bond is replaced by a contact between the two discrete elements. The contact allows us to take into account the crack closing phenomenon.

These illustrations show how simple the qualitative modeling of a continuum behavior with the hybrid lattice-particle approach is. However, behind this apparent simplicity a great complexity to making quantitative simulation is hidden. Predominantly, the following four steps (Figure 2.2) are required to model a continuum behavior quantitatively with the presented approach:

1) Building of the discrete domain with given size and fineness.

2) Selection of the most adapted rheological model of the bonds to model qualitatively the expected mechanical behavior.

3) Quantification of the rheological parameters of the bonds. Generally, it is not always possible to deduce these parameters from analytical laws. This step requires some simulations and is called the *calibration* step.

4) Application of the developed model. The model is implemented to solve and study some scientific and engineering problems. This step is the enforcement of the developed model.

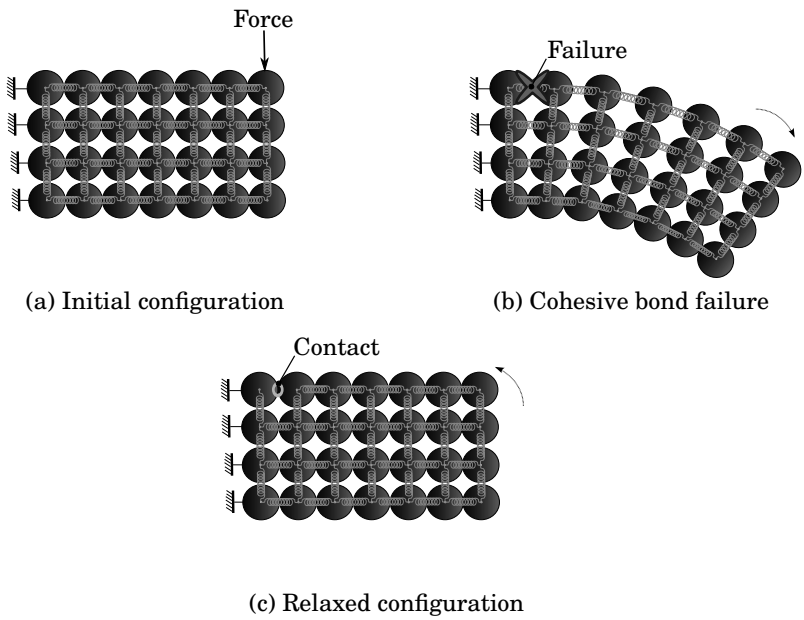

(a) Initial configuration

(b) Cohesive bond failure

(c) Relaxed configuration

Figure 2.1. *Illustration of the hybrid lattice-particle model*

2.2. Explicit dynamic algorithm

The numerical resolution is based on an explicit integration scheme, which is well-adapted to massive DEM

simulation [ROU 04] and high-velocity phenomena such as fracturing or impact. Many explicit schemes can be used: the Verlet velocity, Runge–Kutta, leapfrog or gear's method, etc. [EBE 10, section 13]. In [ROU 04], the authors have compared these algorithms in terms of accuracy, stability and CPU efficiency. It appears that all of them give approximately the same efficiency. In the present work, the Verlet velocity scheme is chosen for its simplicity. The discrete element positions and velocities are estimated by:

$$\mathbf{p}(t+dt) = \mathbf{p}(t) + dt\,\dot{\mathbf{p}}(t) + \frac{dt^2}{2}\,\ddot{\mathbf{p}}(t) \qquad [2.1]$$

$$\dot{\mathbf{p}}(t+dt) = \dot{\mathbf{p}}(t) + \frac{dt}{2}\,(\ddot{\mathbf{p}}(t) + \ddot{\mathbf{p}}(t+dt)) \qquad [2.2]$$

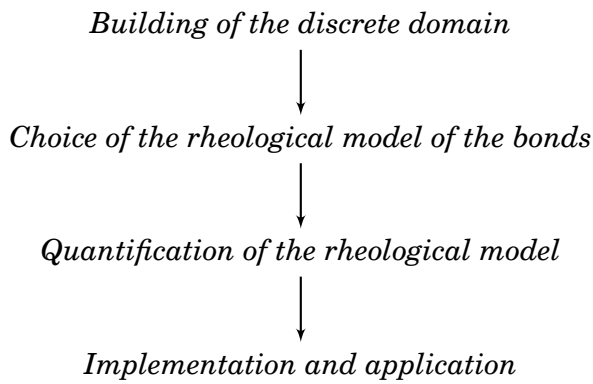

Figure 2.2. *General approach for DEM modeling of continuous materials*

where:

– t is the current time and dt is the integration time step;

– $\mathbf{p}(t)$, $\dot{\mathbf{p}}(t)$ and $\ddot{\mathbf{p}}(t)$ are the linear position, velocity and acceleration of the discrete elements.

The discrete element orientations are described by quaternions, noted as $q(t)$, that facilitate an efficient way to compute the rotation of the local frames associated with the discrete elements [PÖS 05, section 2.5]. Quaternion is linked to the angular velocity with the following equality [EBE 10, section 10.5]:

$$\dot{q}(t) = \frac{1}{2}\,\boldsymbol{\omega}(t)\,q(t) \qquad [2.3]$$

where $\boldsymbol{\omega}(t)$ is the angular velocity of a discrete element. The Verlet velocity scheme is also applied to quaternion $q(t)$, with:

$$q(t+dt) = q(t) + dt\,\dot{q}(t) + \frac{dt^2}{2}\ddot{q}(t) \qquad [2.4]$$

$$\dot{q}(t+dt) = \dot{q}(t) + \frac{dt}{2}\left(\ddot{q}(t) + \ddot{q}(t+dt)\right) \qquad [2.5]$$

To prevent quaternion numerical drifts, the quaternion must be normalized each time step. Algorithm 1 details the encapsulation of the Verlet velocity scheme in an explicit dynamic resolution. Note that this numerical scheme is not well-adapted to quasistatic simulation. Special care, described later in this paper, will be taken with this kind of test.

2.3. Construction of the discrete domain

Starting with the first point of the general approach presented in Figure 2.2, a preliminary work consists of building the initial discrete domain. This point is fundamental. If the initial domain is badly formed, the following simulations that use this domain may give some unexpected behaviors. To prevent this, the following section describes the construction rules to ensure the expected behavior of the discrete domain, independently of its shape or its size. This independence is the main goal of the described

method because it prevent fastidious calibration processes. The calibration process can be done only one time. Then, the obtained parameter values are used for all the discrete domains that model a same material without computation.

input: $\mathbf{p}(0)\ \dot{\mathbf{p}}(0)\ \ddot{\mathbf{p}}(0)\ q(0)\ \dot{q}(0)\ \ddot{q}(0)$
$t \leftarrow 0$;
foreach *iteration* n **do**
  foreach *discrete element* i **do**
    $\mathbf{p}_i(t+dt) \leftarrow$ Verlet velocity scheme [2.1];
    $\mathbf{F}_i(t+dt) \leftarrow$ Sum of forces acting on i;
    $\ddot{\mathbf{p}}_i(t+dt) \leftarrow$ Newton's second law;
    $\dot{\mathbf{p}}_i(t+dt) \leftarrow$ Verlet velocity scheme [2.2];
    $q_i(t+dt) \leftarrow$ Verlet velocity scheme [2.4];
    $q_i(t+dt) \leftarrow$ Normalization;
    $\mathbf{M}_i(t+dt) \leftarrow$ Sum of torques acting on i;
    $\ddot{q}_i(t+dt) \leftarrow$ Angular momentum law;
    $\dot{q}_i(t+dt) \leftarrow$ Verlet velocity scheme [2.5];
  end
  $t \leftarrow t + dt$
end

Algorithm 1. *Explicit dynamic resolution*

Figure 2.3 shows the different steps that are required to build an initial discrete domain. First, a compact granular domain is created (Figures 2.3a and 2.3b). This step requires a granular simulation. Second, the contact network is generated (Figure 2.3c). This network is formed by the branches (Figure 2.3c) that link the centers of the discrete elements in contact. Finally, the different branches of the contact network are replaced by cohesive bonds (solid lines in Figure 2.3d). These bonds will after be used to model the mechanical behavior of the material being modeled.

The effectiveness of the second and the third steps of the initial discrete domain construction are dependent upon the

compaction process (first step). Therefore, it is essential to carry out this step properly. Many methods can be used to achieve this goal such as the iterative growth algorithm [LUB 90], isotropic compression [MAR 03] or densification processes [BAG 05]. Although these methods are widely used in the literature, they are restricted to relatively simple domains. The next section details a new compaction method, which can be used for any domain.

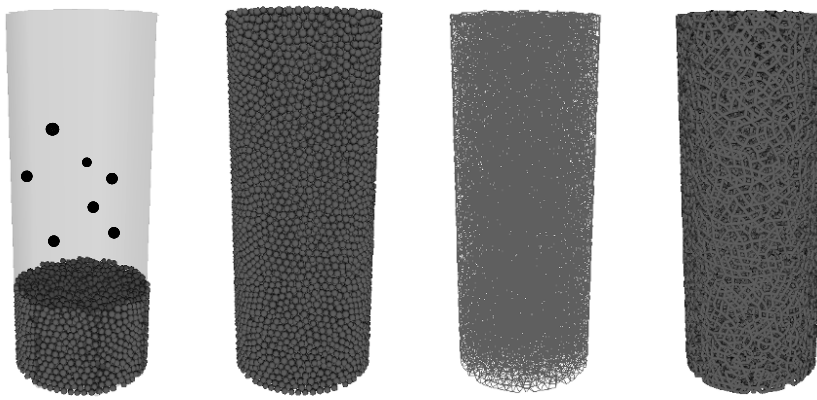

(a) Compaction process | (b) Compacted domain | (c) contact network | (d) cohesive beam network

Figure 2.3. *Different steps to create the initial discrete domain. For a color version of the figure, see www.iste.co.uk/jebahi/discrete.zip*

2.3.1. *The cooker compaction algorithm*

To achieve the compaction process, an original algorithm, which will be named *cooker* in this book, has been developed (algorithm 2). The main idea of the *cooker* algorithm is to fill the free space with randomly placed discrete elements using the `RandomFillDomain()` function (algorithm 2). The input parameters are the external boundaries of the discrete

domain, the characteristics of the discrete elements (distribution of the discrete element sizes or granulometry) and the expected average coordination number (average number of contacts per discrete element).

2.3.1.1. *Stopping criterion of compaction process*

For a mono-disperse distribution of the discrete element sizes, it has been established that the average coordination number (also called cardinal number) must be around 6.2 [GOT 74] and the volume fraction must be around 0.636 [FIN 70]. These two parameters can then be used as shutoff criteria of the compaction process. However, contrary to the average coordination number, the volume fraction can be set *a priori* by setting the number and the radii of the discrete elements. Therefore, the average coordination number must be used as stopping criterion of the *cooker* algorithm. This parameter is calculated for infinite discrete domains as follows:

$$\text{Average coordination number} = \frac{2 \times \text{Number of contacts}}{\text{Number of discrete elements}} \quad [2.6]$$

This formula supposes infinite discrete domains (with no boundaries), which can be modeled in practice using finite domains with periodic boundaries. However, its application on finite discrete domains is not valid. In this case, some discrete elements are cut by the domain boundaries, and then their coordination numbers are only half of the coordination numbers of the internal discrete elements. If the number of the cut discrete elements is small compared to the total number of discrete elements, the error on the average coordination number can be neglected. Otherwise, corrections must be made: the discrete elements belonging to the boundaries as well as the contacts between them must be ignored in [2.6].

2.3.1.2. *Filling process*

Figure 2.4 shows the static random filling of a cube at different stages. The filling process continues until no longer free place exists, i.e. after a given number (to be fixed by the user) of unsuccessful attempts to insert a new discrete element. Then, the discrete elements are forced to be inserted one by one (or by packet) until the expected average coordination number is reached. The forced insertion of a discrete element (or a packet of discrete elements) induces a high interpenetration with some other discrete elements. Therefore, the discrete domain must be relaxed after each forced insertion. This is done by the `RelaxDomain()` function (algorithm 2). This function performs a dynamic computation of the granular domain until the kinetic energy decreases to a very small value. During this computation, the interaction between the discrete elements is ensured by contact laws including damping effects to cancel the kinetic energy.

2.3.1.3. *Overlapping removing*

Once the average coordination number reaches the expected value, the *cooker* process is stopped. At this stage, the average interpenetration between the discrete elements is very significant. Its value can be larger than 2% of the average radius of the discrete elements. A solution, which is implemented in the `DecreaseWallStifness()` function (algorithm 2), consists of decreasing the boundary wall stiffness until this stiffness reaches a negligible value. It should be noted that this function is very time-consuming, and is recommended only when the contact between discrete elements is important in the further simulations (for which the discrete domain is prepared). If the discrete domain is prepared for lattice model simulations (the interaction between the discrete elements is ensured by cohesive bonds with no contact dynamics), this step is not required. Another comment concerns the coordination number. The

`DecreaseWallStifness()` function relaxes the domain and some contacts disappear. This effect significantly reduces the coordination number. Two solutions can be provided:

1) During the `DecreaseWallStifness()` process, the contact network is frozen. Each contact between two discrete elements is replaced by a bilateral spring-dashpot bond. These bonds are parametrized with an initial relaxed length that corresponds to a null interpenetration. With this solution, the coordination number is not affected by the `DecreaseWallStifness()` process.

2) At the end of the `DecreaseWallStifness()` process, the average coordination number is corrected. The final contact network is computed using a greater value of the discrete element radii. The factor used to enlarge the discrete elements is computed due to a dichotomy algorithm. The contact network is finally computed with the enlarging factor to reach the target value of the average coordination number.

The aim of the *cooker* process is to provide a compacted domain with given dimensions, shape, and average coordination number. This granular domain is characterized by a unique contact network. A future step consists of converting this contact network into a cohesive bond network to model the mechanical behavior of the continuum. It can be noted that, with the above solutions, the contact network used to define cohesive bond networks can be larger than the true contact network defined by the physical contacts between discrete elements. This allows each discrete element to have a sufficient number of cohesive bonds (and then a sufficient number of neighboring discrete elements), which prevents numerical problems due to high interactions when some cohesive bonds are destroyed (during a failure simulation for example).

input: the target value of average coordination number, the shape, the size and the granulometry of the compacted domain
output: a compacted domain with the given dimensions, shape, granulometry and very low interpenetration

while *the coordination number is lower than the target value* **do**
  `RelaxDomain();`
  `RandomFillDomain();`
end
`DecreaseWallStifness();`

Function `RelaxDomain()`
  while *kinetic energy is high* **do**
    `OneIterationStep();`
  end
end

Function `RandomFillDomain()`
  while *there is a free space* **do**
    `RandomAddDiscreteElement();`
  end
end

Function `DecreaseWallStifness()`
  while *the wall stiffness is higher than a very small value* **do**
    Decrease wall stiffness to a given small value;
    `RelaxDomain()`
  end
end

Algorithm 2. *The cooker algorithm*

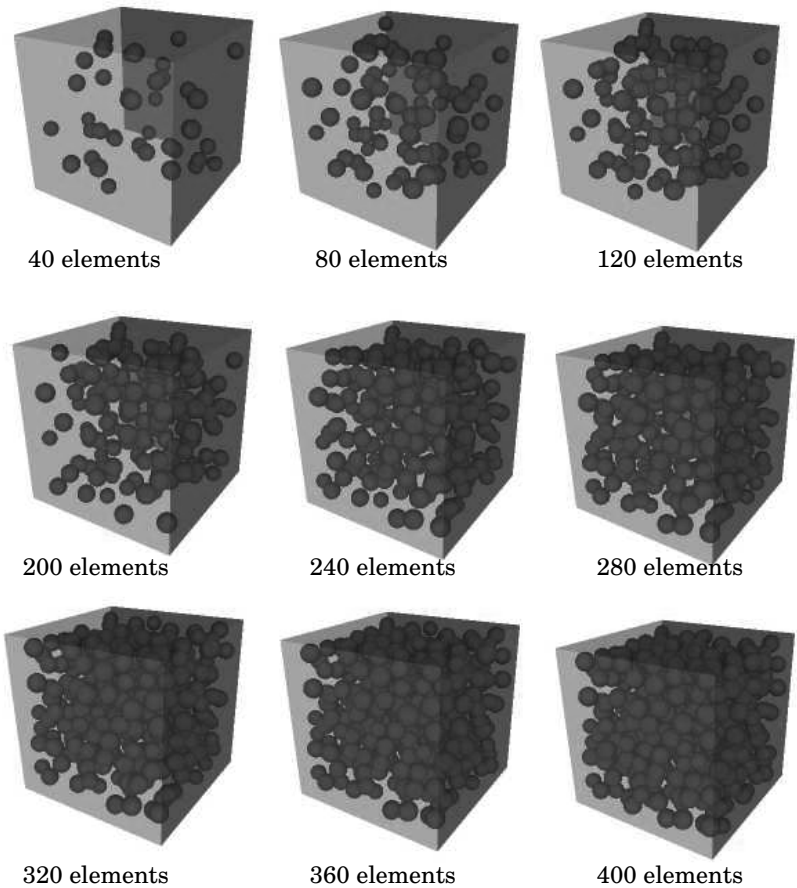

Figure 2.4. *Static random filling of the discrete domain. For a color version of the figure, see www.iste.co.uk/jebahi/discrete.zip*

2.3.2. *Geometrical characterization of the discrete domain*

In hybrid lattice-particle methods, the mechanical behavior of the studied material is governed by the rheological model assigned to the cohesive bonds. In addition, the network architecture of these bonds plays a great role in the mechanical behavior rendering. Schlangen and Garboczi [SCH 96, section 3] have studied the influence of the initial

geometric arrangement. Figure 2.5 illustrates the comparison made by the authors: a precracked sample is loaded in a shear configuration. The sample was modeled by 2D ordered (Figure 2.5a) and disordered (Figure 2.5b) lattices. The crack paths given by the disordered configuration is more realistic than the crack pattern given by the ordered lattice. This study demonstrates that the geometrical arrangement of the initial discrete domain significantly influences the mechanical behavior of the lattice.

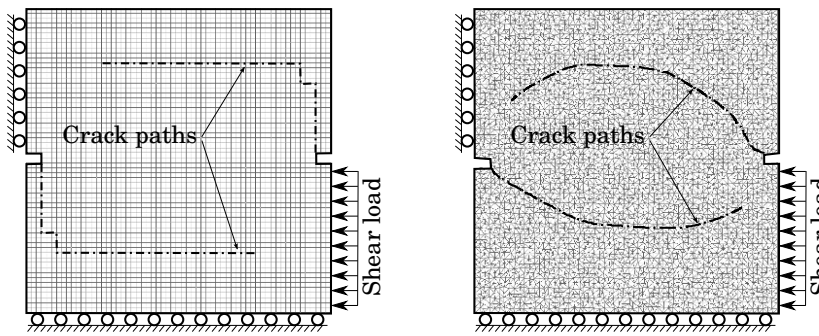

(a) Crack path in ordered 2D lattice

(b) Crack path in disordered 2D lattice

Figure 2.5. *Shear tensile test using different 2D lattices (taken from [SCH 96]). For a color version of the figure, see www.iste.co.uk/jebahi/discrete.zip*

2.3.2.1. *Geometrical isotropy and granulometry*

The definition of geometrical isotropy must be clarified before proposing a criterion characterizing this concept. Cambou [CAM 98, Introduction, S3.6] defines the geometric anisotropy as the distribution of contact and bond directions. If this distribution is perfectly homogeneous, the domain is considered as geometrically isotropic. It is considered that the geometrical isotropy is a necessary condition to ensure the mechanical isotropy of the simulated material. To measure the geometrical organization of granular material, Cambou *et al.* [CAM 09, section 1.2.2] have exploited a mathematical

tool called the "fabric tensor". However, this tool cannot be used to determine the isotropy in a simple way [KEN 84]. A more intuitive method based on a simple geometric computation and statistical analysis is proposed. This method is a three-dimensional (3D) extension of the classical two-dimensional (2D) graphs that classify contacts into direction subsets [KEN 84, D'AD 02].

Contacts are grouped into subsets depending on their orientation in the 3D space. All the members in a subset have a quite similar spatial orientation. To group contacts into orientation subsets, a platonic solid (a geode) of 320 equal faces is used as reference (Figure 2.6). Figure 2.6 and algorithm 3 detail the computation method of the contact directions. For each contact between two discrete elements, the contact direction Δ is determined. The straight line Δ going through the centers of two discrete elements in contact intersects the geode γ at two opposite geode faces f_j and f_k. The number of contacts that intersect each geode face are numbered. This allows us to count the contacts that match a given geode face.

foreach *Discrete element* DE_0 **do**
  Translate the geode γ to the discrete element center O_0;
  foreach *Discrete element* DE_i *in contact with* DE_0 **do**
    Compute the contact direction $\Delta = (O_0, O_i)$;
    Detect the opposite faces f_j and f_k that intersect Δ;
    Increment the contact direction numbers associated to f_j and f_k ;
  end
end

Algorithm 3. *Computation algorithm of the contact directions*

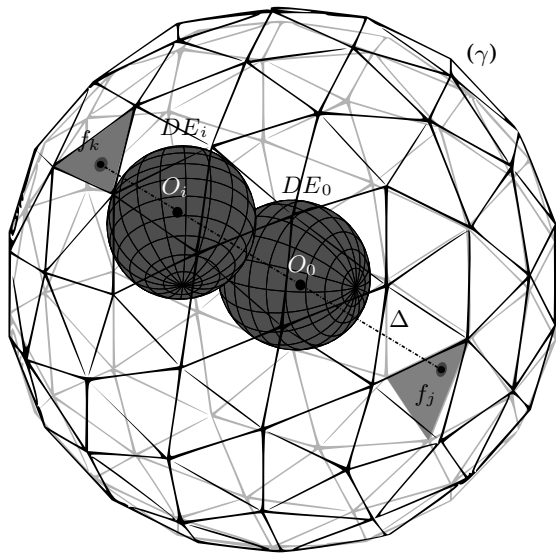

Figure 2.6. *Platonic solid used as a reference geometry to classify the contact orientations*

The final result is a 3D histogram (Figure 2.7) in which each bar represents the number of contacts belonging to an orientation subset (a sort of discretized solid angle). The weight of a given orientation subset is defined as the density of contact orientations that match this subset. As in the computation of the average coordination number (section 2.3.1.1), it is recommended to exclude the discrete elements that belong to the boundaries because the bonds between these elements have privileged directions.

With the aim of simulating isotropic behaviors, the discrete domain must be geometrically isotropic (the different orientation subsets are equally weighted). It is known from the literature [LOC 06] that to prevent an ordered packing configuration and then to promote geometrical isotropy, a dispersion (denoted as κ) must be applied on the radii of the

discrete elements. The most simple case is the case of uniform dispersion defined by maximum and minimum values:

$$\kappa = \frac{R_{max} - R_{min}}{\bar{R}} \qquad [2.7]$$

where R_{max}, R_{min} and $\bar{R}$ are the maximum, the minimum and the average discrete element radii.

Figures 2.8 shows the geometrical arrangement for two values of the dispersion parameter κ. This figure illustrates the influence of the radius dispersion on the geometrical arrangement (Figures 2.8a and 2.8b) and on the contact orientation (Figures 2.8c and 2.8d). For a distribution range $\kappa = 0\%$, the packing seems to be perfectly ordered. The perfect arrangement is strongly anisotropic. In contrast, a higher dispersion value ($\kappa = 25\%$) seems to promote the isotropy.

Figures 2.7a and 2.7b show the 3D histograms used to qualify the observed level of isotropy. From these figures, it is clear that the radius dispersion value κ highly influences the isotropy level. To quantify the isotropy level, it is proposed to compute the mean square difference between the observed frequencies in geode cells (f_i) and the uniform frequency ($1/N$):

$$e = \sum_{i=1}^{N} \frac{\left(f_i - \frac{1}{N}\right)^2}{N} \qquad [2.8]$$

where:

– N is the total number of cells: the 320 geode faces;

– f_i is the observed frequency of the cell i: the ratio between the number of the contacts that match the solid angle i and the total number of contacts.

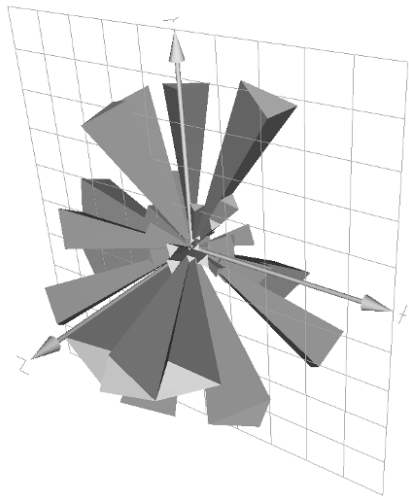

(a) $\kappa = 0\%$

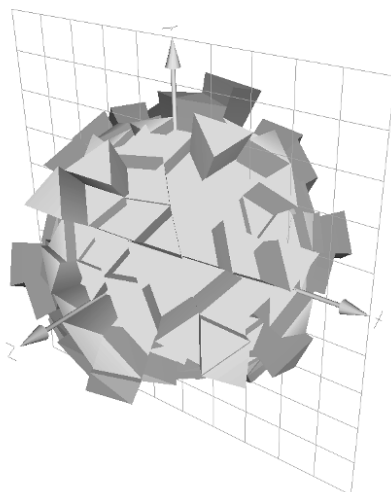

(b) $\kappa = 25\%$

Figure 2.7. *3D histograms of the orientation subsets. For a color version of the figure, see www.iste.co.uk/jebahi/discrete.zip*

The important aspect of this criterion is the asymptotic behavior (Figure 2.9). Increasing the radius dispersion value κ gives an asymptotic constant limit, beginning from a κ value of 15%. This result is in accordance with the observation of Luding [PÖS 01, Chapter 5]: *"crystallization (...) does not occur for polydisperse packing with* $\omega_0 \approx 0.15$*"*. In other words, for a dispersion value higher than 15%, an ordered geometrical arrangement does not occur within the sphere packing. A value of $\kappa = 25\%$ is chosen here to ensure minimal anisotropy.

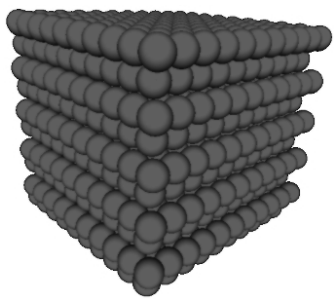

(a) Domain for $\kappa = 0\%$ *(discrete element view)*

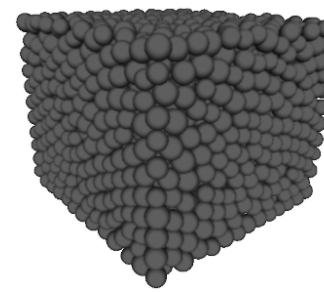

(b) Domain for $\kappa = 25\%$ *(discrete element view)*

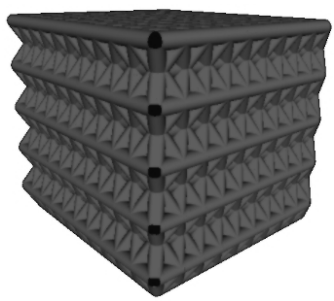

(c) Domain for $\kappa = 0\%$ *(contact network view)*

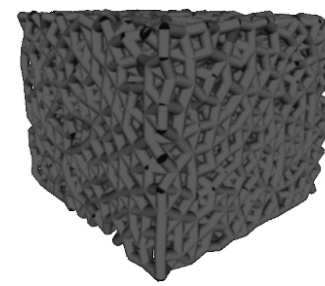

(d) Domain for $\kappa = 25\%$ *(contact network view)*

Figure 2.8. *Geometrical arrangement of a 3D sphere packing with* $\kappa = 0\%$ *and* $\kappa = 25\%$*. For a color version of the figure, see www.iste.co.uk/jebahi/discrete.zip*

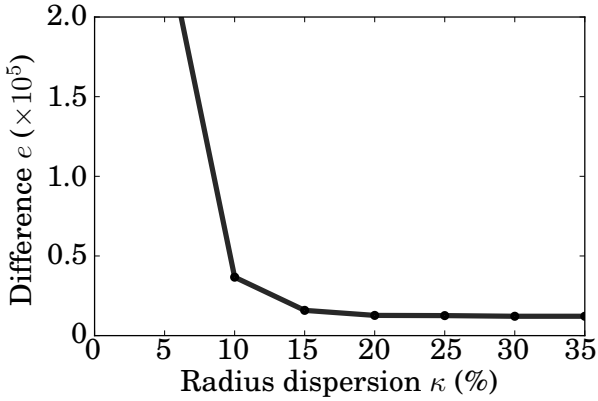

Figure 2.9. *Evolution of the mean square difference e parameter of the sampling distribution of the contact orientation packet versus radius dispersion κ*

2.3.2.2. *Average coordination number*

In the same way as the geometrical isotropy, the average coordination number influences the mechanical behavior. To illustrate this influence, the average coordination number of a given sample is increased due to the dichotomy process described in section 2.3.1.1. Figure 2.10 shows the result on the cohesive bond network with two values of average coordination number. The obtained samples were used to compute the macroscopic Young's modulus E_M and Poisson's ratio ν_M. In this study, all the samples have the same set of cohesive bond parameter values. Figure 2.11 shows the evolution of E_M and ν_M with the average coordination number. As this last parameter increases, the number of cohesive bonds increases. As a result, the rigidity of the Assembly and then the macroscopic Young's modulus increases. In contrast, the macroscopic Poisson's ratio diminishes. It is clear that the average coordination number influences the mechanical behavior.

It is recommended to use an average coordination number value close to 6.2. This value is a characteristic of the

Random Close Packing (RCP) as described in [LOC 06]. This kind of packing ensures a good level of geometrical isotropy. Larger average coordination numbers can also be used to improve simulation of certain complex behaviors (e.g. crack propagation) [AND 13]. However, in this case, high values of Poisson's ratio can be unreachable because of the decreasing tendency of this parameter (Figure 2.11).

(a) Average coordination number of 6.2

(b) Average coordination number of 8.0

Figure 2.10. *Cohesive bond network with two values of average coordination number. For a color version of the figure, see www.iste.co.uk/jebahi/discrete.zip*

The most important thing is to keep the same value of the average coordination number between discrete domains that simulate a same material. This allows us to ensure constant mechanical properties.

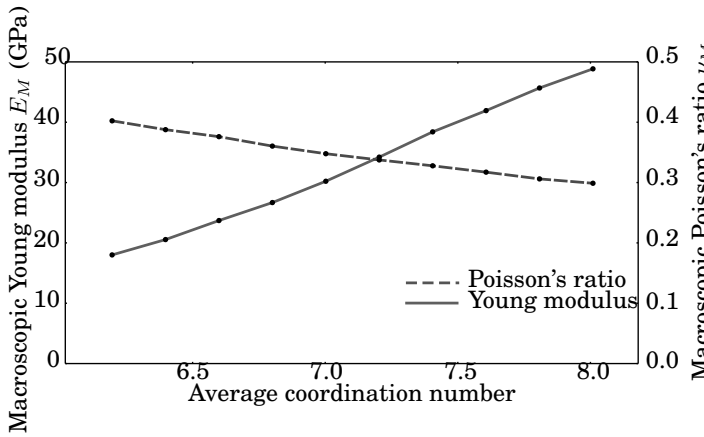

Figure 2.11. *Influence of the average coordination number on mechanical properties*

2.3.2.3. *Discrete domain fineness*

The discrete domain fineness is characterized, for a given volume, by the number of discrete elements that describe this volume. Mainly, three criteria are used to characterize a discrete element representation of a continuum: the volume fraction, the average coordination number and the isotropy (characterized by the mean square difference of the contact orientation subsets). This section deals with two questions:

1) Do the three criteria converge if the number of discrete elements per unit volume increases?

2) In this case, is it possible to define a critical number of discrete elements, beyond which simulation of homogeneous and isotropic media can be systematically performed?

To answer these questions, the influence of the discrete domain fineness on the above three criteria was first investigated. To do so, 22 packing domains having the same bounding volume[1] and different levels of discrete domain fineness were built. To facilitate a statistical processing, 5 packing domains were built for each number of discrete elements (for each fineness level). Therefore, a total of 110 packing domains were analyzed.

Figures 2.12a, 2.12b and 2.12c show the influence of the discrete domain fineness on the volume fraction, the average coordination number and the isotropy. These values are extracted from the discrete domains built with a dispersion radius of $\kappa = 25\%$ (corresponding to the conclusion of the previous section). Small differences could be accepted. The criteria could be classified as following on the basis of order of importance:

1) Isotropy is considered as the most important. This criterion highly influences the discrete sample mechanical behavior.

2) The average coordination number and the volume fraction are less important. However it is important to keep these parameters constant between discrete domains that simulate a same material.

The average coordination number converges to a limit value close to 6.2. As for the volume fraction and isotropy, slight variations are still observed for high number of discrete elements.

1 Bounding volume is defined as the volume of the minimal size hull containing the discrete domain.

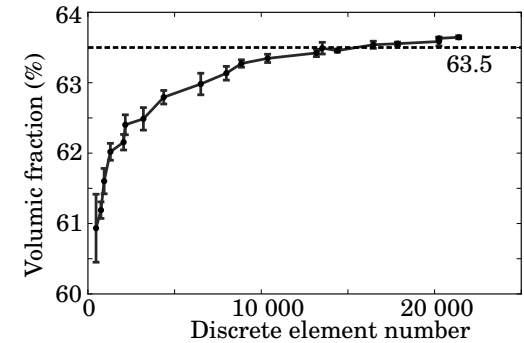

(a) Volume fraction

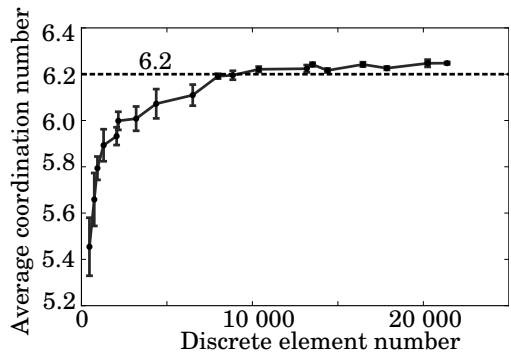

(b) Average coordination number

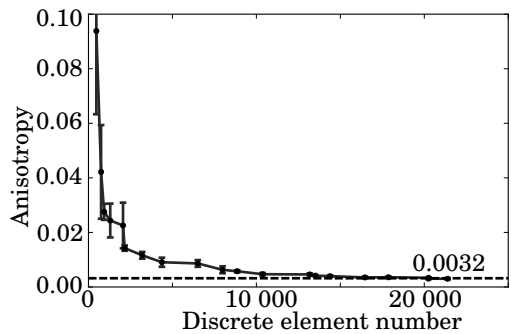

(c) Anisotropy

Figure 2.12. *Evolution of 3 geometrical criteria versus discrete domain fineness (for radius dispersion $\kappa = 25\%$)*

The discrete element number increases with refining. A high refining level brings down the computational performances. Therefore, a compromise must be made between performance and precision. For the next section, a number of $10,000$ discrete elements is considered as sufficient for an acceptable level of precision. For this value, the geometrical anisotropy criterion is lower than 0.0032, the coordination number is higher than 6.2 and the volume fraction is around 0.635. In conclusion, $10,000$ discrete elements in a 3D square domain gives a good level of convergence. This value for one-dimensional (1D) domains can be computed as $10,000^{1/3} \approx 21.5$.

2.4. Mechanical behavior modeling

At this stage, only the granular skeleton is defined. The aim of this section is to give mechanical properties to this skeleton. Following the general method described in Figure 2.2, the second point consists of choosing an appropriate rheological model according to the mechanical behavior of the continuum to be modeled. This model is assigned to the cohesive bonds between the discrete elements (Figure 2.3d). These bonds ensure the discrete domain cohesion, hence the name *cohesive bonds*.

The mechanical behavior of a random structure composed of a large number of discrete elements cannot be analytically predicted. Global behavior is the result of a large number of interactions between discrete elements and can be considered as an emergent physical property [MUN 04, preface]. Implicitly, two scales are considered in a discrete element approach:

– The structure scale, represented by a set of discrete elements. This scale will be called *"macroscopic scale"*.

– The discrete element scale and its elementary interaction with its neighbors. This scale will be called the *"microscopic scale"*.

The mechanical properties such as the Young's modulus or the Poisson's ratio, are considered as emergent properties at the macroscopic scale. Furthermore, unlike the FEM [ZIE 05a], continuous mechanical behavior laws cannot be directly introduced into the DEM formulation. As a result, the difficulty is to quantify DEM microscopic interaction laws according to continuous mechanical behavior. This problem has been discussed in detail by Ostoja-Starzewski [OST 02]. The author proposes micro-macro laws for some typical ordered lattice configurations. In the last paragraph (section 6.3) dedicated to the periodic random lattice network, Ostoja-Starzewski proposes numerical tests to calibrate the model. The analytical approach is limited to an ordered and homogeneous configuration. This idea is well-synthesized by Potyondy and Cundall [POT 04, section 3.1] who write:

"For continuum models, the input properties (such as modulus and strength) can be derived directly from measurements performed on laboratory specimens. For the BPM [2] *(...) the input properties of the components usually are not known. (...) For the general case of arbitrary packing of arbitrarily sized particles, the relation is found by means of a calibration process (...)"*.

To summarize, for random discrete domains, the quantification of the microscopic parameters requires some numerical tests called a calibration procedure. It is proposed, in the following section, to deal with this question with the most simple case: the elastic behavior.

2 *"Bonded Particle Model", discrete element model used by Potyondy and Cundall*

2.4.1. *Cohesive beam model*

The elastic behavior of materials is characterized by a Young modulus and a Poisson ratio. Modeling this behavior with the DEM has been intensively studied, and then several rheological models have been proposed to this end, e.g. the simple spring model [CHU 96, OST 02, GUN 02], the dual spring model (a pair of normal and tangential springs) [POT 04, HEN 04a, FAK 07, TAV 06] and the cohesive beam model [SCH 97, SCH 96, CAR 08] (Figure 2.13). Although the cohesive beam model is not well-established in the literature, this model allows us to obtain more realistic results, compared to classical spring and dual spring models, for some complex problems, e.g. fracture, large shear processes, etc. For example, as mentioned in the previous chapter, Schlangen and Garboczi [SCH 97, section 3] have shown that the cohesive beam model produces more realistic crack pattern than the simple spring and the dual spring models. Therefore, this model is chosen in this book to model the elastic behavior of continuous materials.

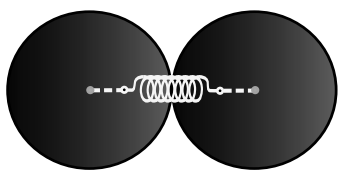

(a) Simple spring model

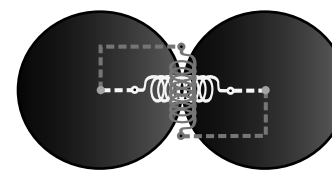

(b) Dual spring model

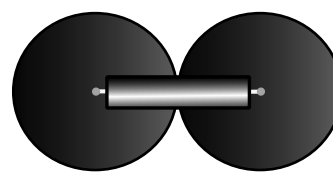

(c) Beam model

Figure 2.13. *Illustration of the three main cohesive bond models. For a color version of the figure, see www.iste.co.uk/jebahi/discrete.zip*

The cohesive beam model was first introduced by Stanley in 1988 [STA 88]. More recently, it was applied to model 2D ordered [SCH 92a, SCH 92b] and disordered [SCH 96, KUN 96, D'AD 02, IBR 03, D'AD 06] lattice networks. A major question that arises from application of this model is how to match the microscopic mechanical properties (of the cohesive beams) to the macroscopic properties (of the material being modeled). In [SCH 96], the authors have proposed to use equivalent microscopic and macroscopic properties. In their work, the beam dimensions (cross-section and inertia momentum) are chosen due to a numerical recursive algorithm to satisfy a uniform elastic continuum condition. However, this algorithm is only applied for simple discrete domains. Other researchers have proposed a more general calibration approach, in which the microscopic and macroscopic mechanical properties can be different and the relationships between them are determined by calibration process. This approach is applicable for any discrete domain, regardless its complexity. Therefore, it is chosen in this work to match the mechanical properties at the different levels. The microscopic properties which can be different from the macroscopic properties must be fitted such that the macroscopic mechanical behavior corresponds to the material being modeled.

2.4.1.1. *Analytical model*

Figure 2.14 shows two discrete elements bonded by a cohesive beam. A cylindrical beam geometry is chosen because its dimensional description requires only two independent parameters: a length l_μ and a radius r_μ[3]. Two mechanical properties are also assigned to the cohesive beams: a Young modulus E_μ and a Poisson ratio ν_μ. These four geometric and mechanical parameters are sufficient to describe the cohesive beam. Note that the cohesive beams are

3 To distinguish microscopic from macroscopic properties, microscopic parameters are denoted by 'μ' and macroscopic parameters by 'M'.

massless; mass properties are assigned only to the discrete elements.

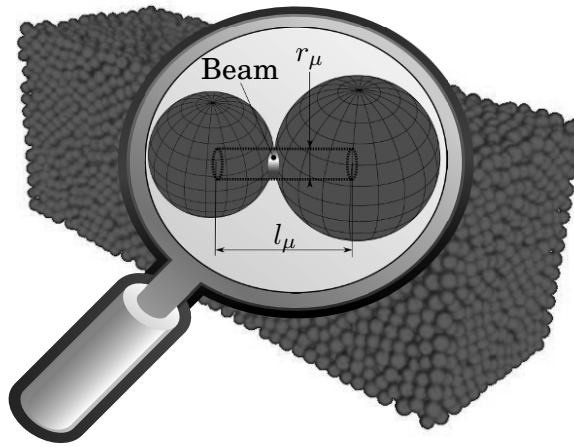

Figure 2.14. *The cohesive beam bond. For a color version of the figure, see www.iste.co.uk/jebahi/discrete.zip*

For the sake of clarity, Figure 2.15 shows a configuration in which the discrete elements have been moved away. The cohesive beam is symbolized by its median line. Both cohesive beam ends are fixed to the discrete element centers O_1 and O_2. The discrete element frames $F_1\left(O_1, \mathbf{X_1}, \mathbf{Y_1}, \mathbf{Z_1}\right)$ and $F_2\left(O_2, \mathbf{X_2}, \mathbf{Y_2}, \mathbf{Z_2}\right)$ are oriented such that $\mathbf{X_1}$ and $\mathbf{X_2}$ are normal to the beam cross-section ends. At the initial time, the beams are relaxed (Figure 2.15a). Figure 2.15b shows the cohesive beam in a loading state due to displacements and rotations of discrete elements.

The well-known analytical beam model of Euler–Bernoulli [TIM 83] is used to describe the mechanical behavior of the cohesive beams. In [GUP 99, section 6.2], the author describes a stiffness matrix expressed in the beam local frame for a finite element application. Figure 2.15b illustrates the beam local frame positioning. The center of discrete element 1 (O_1) is considered as the origin. The

"aligned" configuration, in which $\mathbf{O_1O_2} = k\mathbf{X_1} = -k\mathbf{X_2}$, is considered as the non-bending state and is taken as reference. Consequently, the cohesive beam local frame $F(O, \mathbf{X}, \mathbf{Y}, \mathbf{Z})$ is oriented such that (Figure 2.15b):

$$\mathbf{X} = \frac{\mathbf{O_1O_2}}{\|\mathbf{O_1O_2}\|} \text{ and } \mathbf{Y} = \mathbf{X} \wedge \mathbf{X_1} \text{ and } \mathbf{Z} = \mathbf{X} \wedge \mathbf{Y}$$

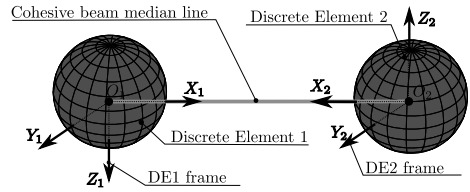

(a) Relaxing state

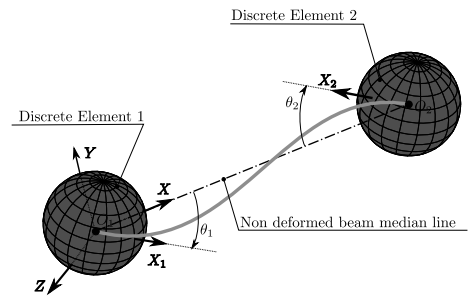

(b) Loading state

Figure 2.15. *Cohesive beam bond configurations. For a color version of the figure, see www.iste.co.uk/jebahi/discrete.zip*

In the local frame F, the deflections at O_1 and O_2 are null. Cross-section bending rotations at O_1 and O_2 are defined, respectively, by $\theta_1 = (\mathbf{X}, \mathbf{X_1})$ and $\theta_2 = (-\mathbf{X}, \mathbf{X_2})$ (Figure 2.15b). Consequently, the force and torque reactions

acting on discrete elements 1 and 2 are:

$$\mathbf{F_{DE1}} = +E_\mu S_\mu \frac{\Delta l_\mu}{l_\mu}\mathbf{X} - \frac{6E_\mu I_\mu}{l_\mu^2}\left(\left(\theta_{2z}+\theta_{1z}\right)\mathbf{Y} + \left(\theta_{2y}+\theta_{1y}\right)\mathbf{Z}\right) \quad [2.9]$$

$$\mathbf{F_{DE2}} = -E_\mu S_\mu \frac{\Delta l_\mu}{l_\mu}\mathbf{X} + \frac{6E_\mu I_\mu}{l_\mu^2}\left(\left(\theta_{2z}+\theta_{1z}\right)\mathbf{Y} - \left(\theta_{2y}+\theta_{1y}\right)\mathbf{Z}\right) \quad [2.10]$$

$$\mathbf{M_{DE1}} = +\frac{G_\mu Io_\mu}{l_\mu}\left(\theta_{2x}-\theta_{1x}\right)\mathbf{X} - \frac{2E_\mu I_\mu}{l_\mu}\left(\left(\theta_{2y}+2\theta_{1y}\right)\mathbf{Y} - \left(\theta_{2z}+2\theta_{1z}\right)\mathbf{Z}\right) \quad [2.11]$$

$$\mathbf{M_{DE2}} = -\frac{G_\mu Io_\mu}{l_\mu}\left(\theta_{2x}-\theta_{1x}\right)\mathbf{X} - \frac{2E_\mu I_\mu}{l_\mu}\left(\left(2\theta_{2y}+\theta_{1y}\right)\mathbf{Y} - \left(2\theta_{2z}+\theta_{1z}\right)\mathbf{Z}\right) \quad [2.12]$$

where:

– $\mathbf{F_{DE1}}$ and $\mathbf{F_{DE2}}$ are the beam force reactions acting on discrete elements 1 and 2.

– $\mathbf{M_{DE1}}$ and $\mathbf{M_{DE2}}$ are the beam torque reactions acting on discrete elements 1 and 2.

– l_μ and Δl_μ are the initial beam length and the longitudinal extension.

– $\boldsymbol{\theta}_{\mathbf{DE1}}(\theta_{1x},\theta_{1y},\theta_{1z})$ and $\boldsymbol{\theta}_{\mathbf{DE1}}(\theta_{2x},\theta_{2y},\theta_{2z})$ are the rotations of beam cross-section at the points O_1 and O_2 expressed in the beam local frame.

– S_μ, Io_μ and I_μ are the beam cross-section area, polar moment of inertia and moment of inertia along $\mathbf{Y}$ and $\mathbf{Z}$.

– E_μ and G_μ are the Young and shear moduli.

Note that the beam force and torque reactions are expressed in the beam local frame $F(O, \mathbf{X}, \mathbf{Y}, \mathbf{Z})$.

2.4.1.2. *Strain energy computation*

The explicit integration algorithm (section 2.2) requires small time steps. Therefore, it can be supposed that the different discrete element variables (forces, torques, displacement, rotations, etc.) are constant during a time step. This assumption allows us to compute the strain energy stored by the cohesive beams as the sum of their elementary works ΔW produced at each time step:

$$\Delta W = \mathbf{F_{DE1}}.\mathbf{\Delta U_{DE1}} + \mathbf{F_{DE2}}.\mathbf{\Delta U_{DE2}} + \mathbf{M_{DE1}}.\mathbf{\Delta \theta_{DE1}} + \mathbf{M_{DE2}}.\mathbf{\Delta \theta_{DE2}} \quad [2.13]$$

where:

– $\mathbf{F_{DE1}}$ and $\mathbf{F_{DE2}}$ are the beam force reactions acting on discrete elements 1 and 2 computed at a given time step;

– $\mathbf{M_{DE1}}$ and $\mathbf{M_{DE2}}$ are the beam torque reactions acting on discrete elements 1 and 2 computed at a given time step;

– $\mathbf{\Delta U_{DE1}}$ and $\mathbf{\Delta U_{DE2}}$ are the elementary displacements of the bonded discrete elements 1 and 2 done during a given time step;

– $\boldsymbol{\theta}_{\mathbf{DE1}}$ and $\boldsymbol{\theta}_{\mathbf{DE2}}$ are the elementary rotations of the bonded discrete elements 1 and 2 done during a given time step;

This elementary strain energy can be divided into tensile, bending and torsion energies as follows:

$$\Delta W_{Tensile} = \mathbf{F_{DE1}}.\mathbf{X} \times \mathbf{\Delta U_{DE1}}.\mathbf{X} + \mathbf{F_{DE2}}.\mathbf{X} \times \mathbf{\Delta U_{DE2}}.\mathbf{X} \quad [2.14]$$

$$\begin{aligned}\Delta W_{Bending} = {} & \mathbf{F_{DE1}}.\mathbf{Y} \times \mathbf{\Delta U_{DE1}}.\mathbf{Y} + \mathbf{F_{DE2}}.\mathbf{Y} \times \mathbf{\Delta U_{DE2}}.\mathbf{Y} \\ & + \mathbf{F_{DE1}}.\mathbf{Z} \times \mathbf{\Delta U_{DE1}}.\mathbf{Z} + \mathbf{F_{DE2}}.\mathbf{Z} \times \mathbf{\Delta U_{DE2}}.\mathbf{Z} \\ & + \mathbf{F_{DE1}}.\mathbf{Y} \times \boldsymbol{\theta}_{\mathbf{DE1}}.\mathbf{Y} + \mathbf{F_{DE2}}.\mathbf{Y} \times \boldsymbol{\theta}_{\mathbf{DE2}}.\mathbf{Y} \\ & + \mathbf{F_{DE1}}.\mathbf{Z} \times \boldsymbol{\theta}_{\mathbf{DE1}}.\mathbf{Z} + \mathbf{F_{DE2}}.\mathbf{Z} \\ & \times \boldsymbol{\theta}_{\mathbf{DE2}}.\mathbf{Z} \end{aligned} \quad [2.15]$$

$$\begin{aligned}\Delta W_{Torsion} = {} & \mathbf{F_{DE1}}.\mathbf{X} \times \boldsymbol{\theta}_{\mathbf{DE1}}.\mathbf{X} + \mathbf{F_{DE2}}.\mathbf{X} \\ & \times \boldsymbol{\theta}_{\mathbf{DE2}}.\mathbf{X} \end{aligned} \quad [2.16]$$

where $F\left(O, \mathbf{X}, \mathbf{Y}, \mathbf{Z}\right)$ is the beam local frame (section 2.4.1.1). So, at a given time t corresponding to n computational iterations, the strain energies stored by a cohesive beam are:

$$W_{Tensile} = \sum_{i=1}^{n} \Delta W_{Tensile} \quad [2.17]$$

$$W_{Bending} = \sum_{i=1}^{n} \Delta W_{Bending} \quad [2.18]$$

$$W_{Torsion} = \sum_{i=1}^{n} \Delta W_{Torsion} \quad [2.19]$$

2.4.2. *Calibration of the cohesive beam static parameters*

The aim of the calibration process is to quantify the values of the microscopic parameters to fit the macroscopic properties. The main difficulty is to establish the transition laws between the i microscopic parameters $(\gamma_\mu^1, \gamma_\mu^2, \ldots, \gamma_\mu^i)$ of the cohesive beams and the j macroscopic parameters $(\Gamma_M^1, \Gamma_M^2, \ldots, \Gamma_M^j)$ of the material being modeled. This section describes the calibration process of the cohesive beam static parameters used to model an elastic continuum. In this case, four parameters define the cohesive beams: the length , the

radius, the microscopic Young modulus and the microscopic Poisson ratio $(l_\mu, r_\mu, E_\mu, \nu_\mu)$. Whereas, only two parameters define the continuum: the macroscopic Young modulus and the macroscopic Poisson ratio (E_M, ν_M).

To simplify the calibration process, a parametric study aiming to investigate the influence of the microscopic parameters on the macroscopic mechanical properties was done. In this study, several numerical quasistatic uniaxial tensile tests were simulated, using different microscopic parameters in the cohesive beams.

2.4.2.1. *Quasistatic tensile test description*

A perfectly homogeneous, isotropic, elastic material is characterized by the Young modulus E_M and the Poisson ratio ν_μ. For real materials, these parameters are generally determined by quasistatic tensile tests. These experimental procedures can also be applied to a numerical sample.

2.4.2.1.1. From discrete to continuous geometry

To compute the macroscopic Young modulus and the Poisson's ratio, a perfect 3D continuous geometry is associated with the compact discrete domain. This perfect geometry is the bounding shape of the compacted discrete domain. The discrete elements belonging to the domain boundaries are marked to compute the perfect geometry dimensions (Figure 2.16). With the cylinder shape, three discrete element sets are marked (Figure 2.16) as:

– The "xMax" and "xMin" sets are associated with faces with normal $\mathbf{X}$ and $-\mathbf{X}$.

– The "radius" set is associated with the cylinder circumference.

The Perfect cylinder dimensions are computed as:

$$L_M = 2\overline{R} + \left(\frac{1}{N_{xMax}} \sum_{i=1}^{N_{xMax}} \mathbf{OG_i} + \frac{1}{N_{xMin}} \sum_{i=0}^{N_{xMin}} \mathbf{OG_i} \right) .\mathbf{X} \quad [2.20]$$

$$R_M = \overline{R} + \frac{1}{N_{radius}} \sum_{i=1}^{N_{radius}} \sqrt{(\mathbf{OG_i}.\mathbf{Y})^2 + (\mathbf{OG_i}.\mathbf{Z})^2} \quad [2.21]$$

where:

– L_M and R_M are the perfect cylinder length and radius.

– N_{xMax}, N_{xMin} and N_{radius} are the number of discrete elements belonging respectively to “xMax”, “xMin” and “radius” sets.

– $\mathbf{OG_i}$ is the position of the gravity center of the discrete element i.

– $\overline{R}$ is the average discrete element radius over the entire domain.

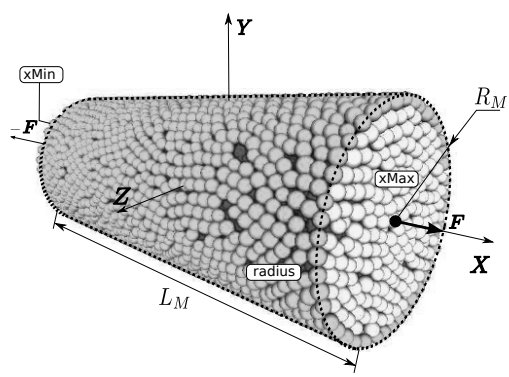

Figure 2.16. *Perfect cylinder associated with a discrete domain with $\kappa = 25\%$. For a color version of the figure, see www.iste.co.uk/jebahi/discrete.zip*

2.4.2.1.2. Loading

To ensure a quasistatic tensile test, the loading force acting on the discrete element sets "xMin" and "xMax", are progressively applied (linear ramp) and stabilized. The sum of forces acting on "xMax" and "xMin" are denoted by $\mathbf{F_{xMax}}$ and $\mathbf{F_{xMin}}$, respectively. These two forces, acting along $\mathbf{X}$ for $\mathbf{F_{xMax}}$ and $-\mathbf{X}$ for $\mathbf{F_{xMin}}$, have equal norms and opposite directions. To check the quasistatic properties, the kinetic and strain energies are computed and stored during the numerical test (section 2.4.1.2 for the computational method). Figure 2.17 confirms that the applied tensile loading gives a negligible kinetic energy and ensures a quasistatic aspect of the simulation.

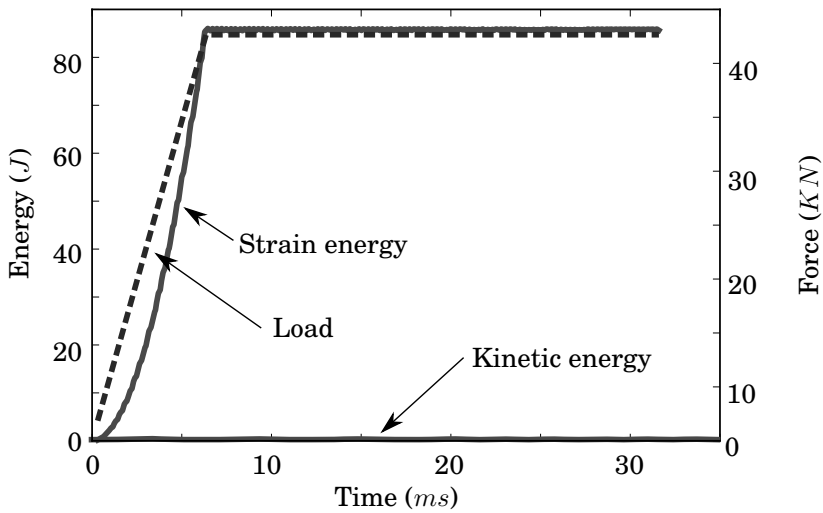

Figure 2.17. *Kinetic and strain energies and load during a quasistatic tensile test (computed with a time step $\Delta t = 3.10^{-7} s$ and a number of iterations n =100 000)*

2.4.2.1.3. E_M and ν_M computation

The macroscopic Young modulus and the Poisson ratio can be easily determined for the cylinder sample by using the

material strength analytical formulations:

$$E_M = \frac{F/S_{M_0}}{\Delta L_M / L_{M_0}} \quad [2.22]$$

$$\nu_M = -\frac{\Delta R_M / R_{M_0}}{\Delta L_M / L_{M_0}} \quad [2.23]$$

where:

– L_{M_0}, R_{M_0} and S_{M_0} are the initial bounding cylinder dimensions (respectively: length, radius, and section).

– E_M and ν_M are the macroscopic Young modulus and Poisson ratio.

– F is the normal force.

The explicit numerical schemes are not well-adapted to the quasistatic simulation. The system vibrates around the static solution. To facilitate results stabilization, a pure numerical damping factor is introduced in the numerical scheme as described by Tchamwa and Wielgosz [MAH 09]. This is a decentered explicit integration scheme that facilitates high frequency dissipation. This scheme is very similar to the Verlet velocity algorithm. The dissipation is controlled with a single parameter φ. Only the second time derivative terms are modified. Equations [2.2] and [2.5] become:

$$\dot{\mathbf{p}}(t+dt) = \dot{\mathbf{p}}(t) + \varphi \frac{dt}{2} \left(\ddot{\mathbf{p}}(t) + \ddot{\mathbf{p}}(t+dt)\right) \quad [2.24]$$

$$\dot{q}(t+dt) = \dot{q}(t) + \varphi \frac{dt}{2} \left(\ddot{q}(t) + \ddot{q}(t+dt)\right) \quad [2.25]$$

A value $\varphi = 1.3$ is used to facilitate a high convergence rate to the static solution, as shown in Figure 2.18. To ensure a high convergence rate, the time step dt must be close to the critical time step dt_{max} of the explicit numerical scheme.

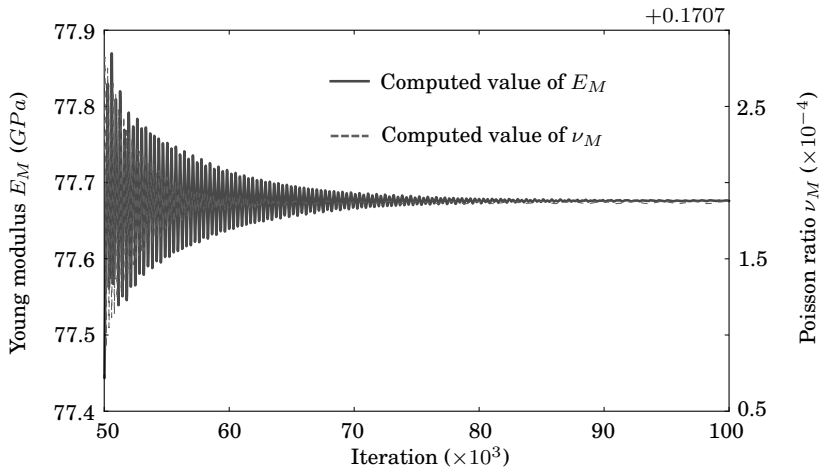

Figure 2.18. *Numerical damping effects on the macroscopic Young modulus E_M and Poisson ratio ν_M. For a color version of the figure, see www.iste.co.uk/jebahi/discrete.zip*

2.4.2.2. *Parametric study*

As shown previously, the cohesive beam bonds are defined by four parameters:

– Two geometrical parameters: length l_μ and radius r_μ.

– Two mechanical parameters: microscopic Young's modulus E_μ and microscopic Poisson's ratio ν_μ.

The lengths of the cohesive beam bonds are imposed by the distances between the centers of the discrete elements in contact and are not to be determined (non-free parameters). The other three parameters which are assumed to be the same for all the cohesive beams are free and must be quantified. Concerning the second geometrical parameter (r_μ), dimensionless cohesive beam radius, noted as $\tilde{r_\mu}$ and defined as the ratio between the beam radius r_μ and the mean radius of the discrete elements $\bar{R}$, will be preferred to

the beam radius. This allows this parameter to be independent of the size of discrete elements.

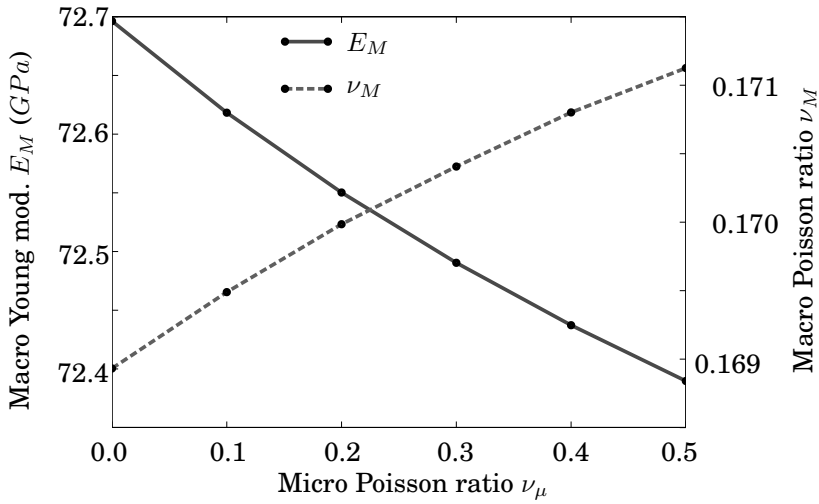

Figure 2.19. *Influence of ν_μ on E_M and ν_M*

2.4.2.2.1. Microscopic Poisson's ratio influence

Figure 2.19 shows the evolution of the macroscopic Young modulus E_M and Poisson ratio ν_M for different values of the microscopic Poisson ratio ν_μ in the range $[0, 0.5]$. It is observed that the microscopic parameter ν_μ does not influence significantly the macroscopic properties (E_M and ν_M). Actually, this parameter is only involved in [2.11] and [2.12] to compute the microscopic shear modulus G_μ, which in turn is only used to determine the local torsion loading (of the cohesive beams). To explain the ν_μ independence of the macroscopic properties, the total elastic energy during the quasistatic tensile test is split up into three energies (section 2.4.1.2 for details on the computation methods):

– *Tension* energy characterized by the sum of the cohesive beam works of the normal forces.

– *Bending* energy characterized by the sum of the cohesive beam works of the bending torques.

– *Torsion* energy characterized by the sum of the cohesive beam works of the torsion torques.

Figure 2.20 presents the evolution of these energies with time. The contribution of the torsion energy is minor (Figure 2.20), which explains the negligible effect of the microscopic Poisson ratio ν_μ. Consequently, this parameter can be fixed arbitrarily. For the rest of the study, a value of $\nu_\mu = 0.3$ is chosen.

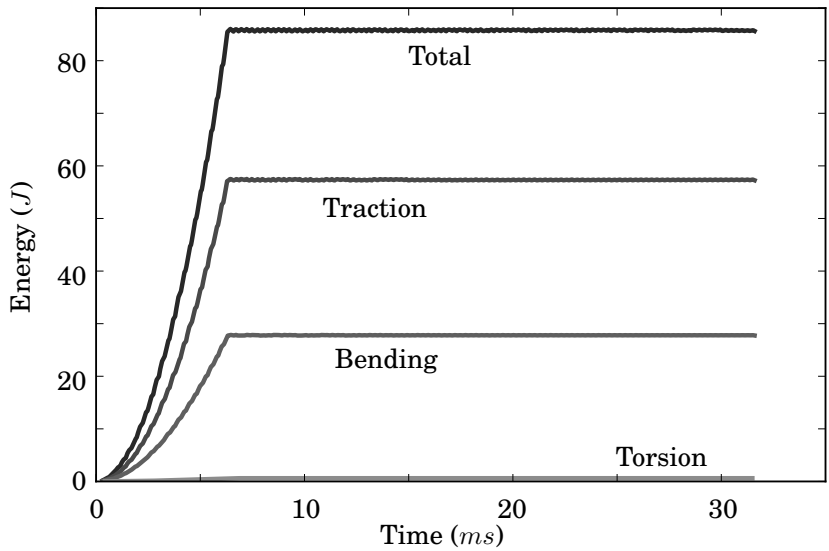

Figure 2.20. *Energy breakdown of total elastic energy stored by cohesive beams for the quasistatic tensile test (computed with a time step $\Delta t = 3.10^{-7} s$ and a number of iterations $n = 100\,000$)*

2.4.2.2.2. Microscopic Young's modulus influence

Figure 2.21 shows the evolution of the macroscopic parameters as a function of the microscopic Young modulus E_μ for different values of $\tilde{r_\mu}$ (microscopic radius ratio). Based on this figure, E_μ increases linearly the macroscopic Young

modulus, whereas it has no significant influence on the macroscopic Poisson ratio ν_M. Table 2.1 gives an outline of these evolutions.

Macro. parameters	Macro. Young's modulus E_M	Macro. Poisson's ratio ν_M
Functions	$E_M = f_1(E_\mu)$	$\nu_M = f_2(E_\mu)$
Evolution	increasing linear function	constant function
Figures	2.21a	2.21b

Table 2.1. *Influence of the microscopic Young modulus on the macroscopic properties*

2.4.2.2.3. Microscopic radius ratio influence

Figure 2.22 shows the evolution of the macroscopic parameters as a function of the microscopic radius ratio $\tilde{r_\mu}$ for different values of the microscopic Young modulus. Both the macroscopic Young modulus E_M and the macroscopic Poisson ratio ν_M are nonlinearly dependent upon $\tilde{r_\mu}$, but with reversed trends. $\tilde{r_\mu}$ increases E_M and decreases ν_M. Table 2.2 gives an outline of these evolutions.

2.4.2.3. *Calibration method for static parameters*

Section 2.4.2.2 has described the influence of the microscopic parameters ν_μ, E_μ and $\tilde{r_\mu}$ on the macroscopic parameters E_M and ν_M. The results of this section have been used to develop a calibration methodology. The next three steps describe this methodology with an application to the silica glass material whose Young modulus and Poisson ratio are respectively $E_M^{Silica} = 75\,\mathrm{GPa}$ and $\nu_M^{Silica} = 0.17$.

1) *Calibration of the microscopic Poisson ratio* ν_μ

Section 2.4.2.2.1 has shown that the influence of the microscopic Poisson ratio ν_μ is negligible. Its value is arbitrarily fixed at 0.3.

2) *Calibration of the microscopic radius ratio* $\tilde{r_\mu}$

The microscopic Young modulus E_μ is arbitrarily fixed at the macroscopic value (the silica glass value). A set of tensile

tests are simulated to plot the evolution of ν_M with $\tilde{r_\mu}$. This evolution facilitates to retrieve the value of $\tilde{r_\mu}$ that matches the value of the silica Poisson ratio, as shown in Figure 2.23a.

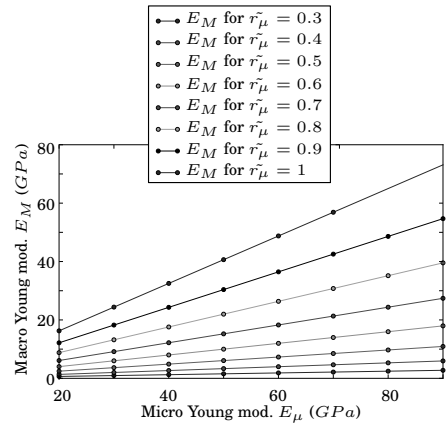

(a) E_M evolution as a function of E_μ

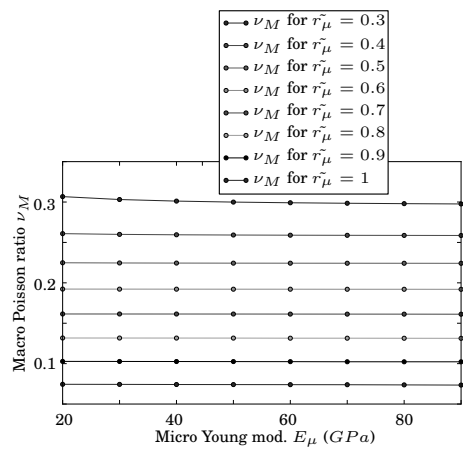

(b) ν_M evolution as a function of E_μ

Figure 2.21. *Microscopic Young's modulus E_μ influence on the macroscopic parameters E_M and ν_M. For a color version of the figure, see www.iste.co.uk/jebahi/discrete.zip*

Macro. parameters	Macro. Young's modulus E_M	Macro. Poisson's ratio ν_M
Functions	$E_M = f_3(\tilde{r_\mu})$	$\nu_M = f_2(\tilde{r_\mu})$
Evolution	increasing quadratic function.	decreasing quadratic function
Figures	2.22a	2.22b

Table 2.2. *Influence of the microscopic radius ratio on the macroscopic properties*

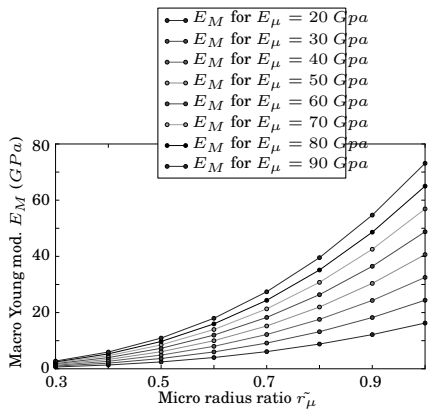

(a) E_M evolution as a function of $\tilde{r_\mu}$

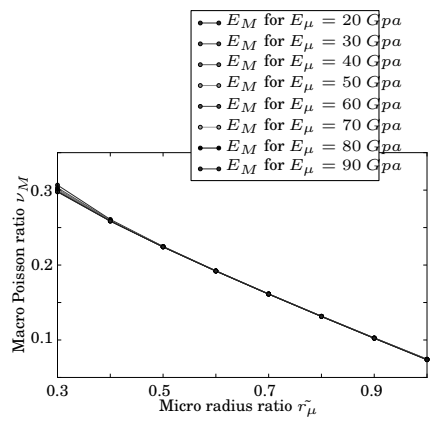

(b) ν_M evolution as a function of $\tilde{r_\mu}$

Figure 2.22. *Microscopic radius ratio $\tilde{r_\mu}$ influence on the macroscopic parameters E_M and ν_M. For a color version of the figure, see www.iste.co.uk/jebahi/discrete.zip*

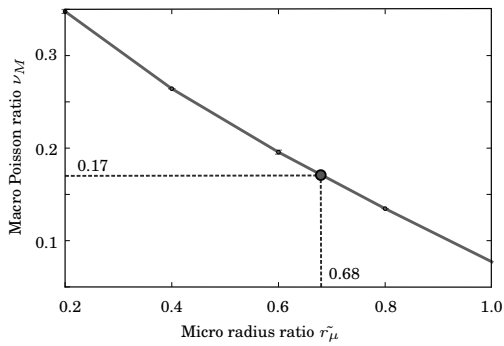

(a) Calibration of $\tilde{r_\mu}$

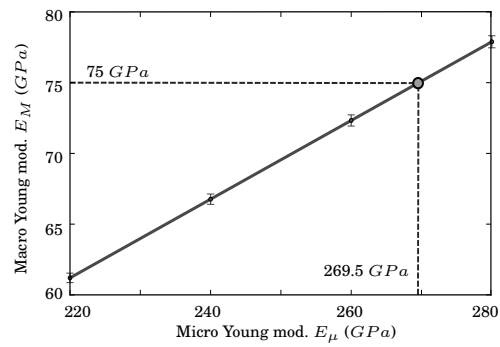

(b) Calibration of E_μ

Figure 2.23. *Calibration of microscopic parameters $\tilde{r_\mu}$ and E_μ that match the silica Young modulus and Poisson ratio values*

3) *Calibration of the microscopic Young modulus E_μ*

The microscopic radius ratio $\tilde{r_\mu}$ was quantified in the previous step. A set of tensile tests are simulated to plot the evolution of E_M with E_μ. This evolution facilitates to retrieve the value of E_μ that matches the value of the silica Young modulus, as shown in Figure 2.23b. Note that E_μ have no influence on the macroscopic Poisson ratio ν_M which was fitted in the previous step (section 2.4.2.2.2).

2.4.2.4. *Convergence study*

To apply the cohesive beam model to any material geometry, it must be verified that the calibration results do not depend on the number of discrete elements in a given material volume. To check this property, many discrete samples (with similar bounding dimensions) were built with an increasing number of discrete elements (Figure 2.24). The samples satisfy the criteria established in section 2.3. To take into account the variability of the sample geometry, four different samples were built for each number of discrete elements.

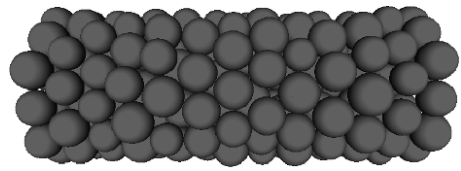

(a) 200 discrete elements

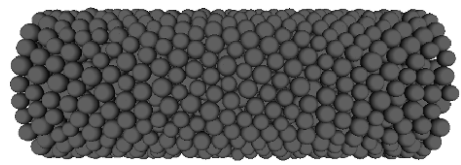

(b) 2 000 discrete elements

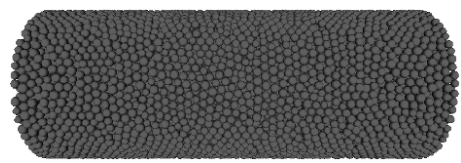

(c) 20 000 discrete elements

Figure 2.24. *Snapshot of discrete samples with increasing fineness. For a color version of the figure, see www.iste.co.uk/jebahi/discrete.zip*

Figure 2.25 shows the evolution of the macroscopic parameters E_M and ν_M as a function of the number of

discrete elements. Beyond $10,000$ discrete elements, the macroscopic Young modulus E_M and the macroscopic Poisson ratio ν_M fluctuate respectively around 3% and 2.5%. These fluctuations seem to be better than those obtained in the literature. Hentz *et al.* [HEN 04a] have shown that the Liao calibration methodology for the dual spring model [LIA 97] gives a dispersion around 28% for the Young modulus and 16% for the Poisson ratio. To improve the accuracy, the same authors have introduced an energy criterion, which has allowed us to reduce the dispersions to around 12% and 10%, respectively. However, this criterion is assembly dependent and must be computed for each sample.

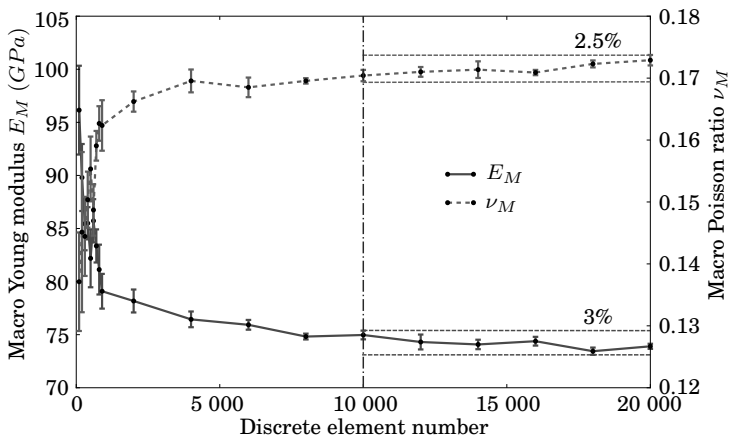

Figure 2.25. *Evolution of the macroscopic parameters E_M and ν_M as a function of the number of discrete elements. For a color version of the figure, see www.iste.co.uk/jebahi/discrete.zip*

The cohesive beam model associated with the compaction criteria facilitates a better precision without any recomputation. Consequently, a set of microscopic parameters $\tilde{r_\mu}$, E_μ and ν_μ allows us to model an elastic material whatever shape or discrete domain fineness it has, provided that a

sufficient number of discrete elements is used ($10,000$ or more).

2.4.2.5. *Validation*

The previous sections provide a methodology for calibrating the microscopic parameters from the macroscopic elastic properties. Tables 2.3 and 2.4 summarize the results obtained for the silica glass material. To validate these results, the obtained microscopic elastic parameters are used to build a cylindrical numeric sample of silica glass. This sample is submitted to quasistatic tensile, bending and torsion loadings, such that the "xMin" discrete element set is fixed and "xMax" set is loaded. To reproduce a quasistatic aspect, the loads are applied gradually (section 2.4.2.1.2). The free face ("xMax" set) displacement and rotation given by the numerical simulations are compared to the results given by the material strength theory. Table 4.2 summarizes the differences in terms of percentages between numerical and theoretical results. The higher difference is obtained for the torsion test and is less than 7%. A possible cause can be the definition of the bounding radius of the sample. A small difference on the radius value theoretically leads to a difference of fourth order magnitude on the torsion results because of the computation of the second moment of area. Figure 2.26 shows the two possible definitions of the sample radius. If the *Effective section* is used instead of the *Max section*, the difference for the torsion test decreases to a value of 1.8%. However the other differences, for bending and tensile tests, increase.

Young's Modulus	Poisson's ratio
$E_M = 75\ GPa$	$\nu_M = 0.17$

Table 2.3. *Macroscopic silica glass elastic parameters*

The transition from the discrete sample to a continuous shape has so far been an open question. A proposed solution

consists of computing the bounding volume of the discrete sample. The advantage of this definition is its simplicity. However, a more complex definition of the equivalent continuous geometry from a discrete sample may provide better results.

Young's Modulus	Poisson's ratio	Radius ratio
$E_\mu = 295.5\ GPa$	$\nu_\mu = 0.3$	$\tilde{r_\mu} = 0.68$

Table 2.4. *Microscopic silica glass elastic parameters*

	Tensile	Bending	Torsion
Criteria	Free face normal displacement	Free face tangential deflection	Free face rotation
Difference	1.20 %	4.16 %	6.13 %

Table 2.5. *Comparison of the numerical and theoretical results for the quasistatic tensile, bending and torsion tests*

2.4.3. *Calibration of the cohesive beam dynamic parameters*

The previous section has dealt with the calibration of the elastic (static) parameters. The presented calibration approach facilitates for quantification of the three microscopic elastic parameters (Young's modulus E_μ, cohesive beam radius $\tilde{r_\mu}$ and Poisson's ratio ν_μ) to obtain the expected elastic behavior at the structure scale. To quantitatively simulate dynamic phenomena such as cracks or impacts, it is also necessary to calibrate the microscopic mass parameters.

2.4.3.1. *Calibration method for dynamic parameters*

The discrete element mass parameters (mass and inertia matrix) depend on the discrete element volume and density. Since the geometrical characteristics of the discrete elements are set out during the construction of the discrete domain, only the density of these elements is to be adjusted. As the elastic parameters, this microscopic parameter can be

different from the macroscopic density of the material being modeled (to compensate the voids between the discrete elements in the compacted domain). To quantify this parameter, a very simple calibration criterion is chosen. This criterion ensures mass equality between the discrete and continuous domains:

$$\rho_\mu = \frac{\rho_M V_M}{\sum_{i=1}^{N} V_{\mu_i}} \qquad [2.26]$$

where:

– ρ_μ and V_{μ_i} are respectively the discrete element density and volume.

– ρ_M and V_M are respectively the continuous density and volume. The continuous domain dimensions are computed as presented in section 2.4.2.1.1.

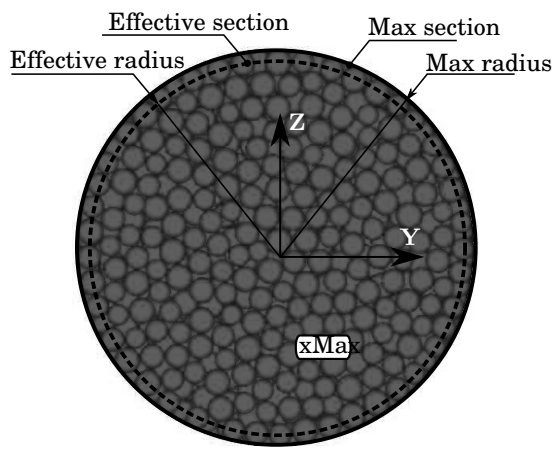

Figure 2.26. *Two possible definitions of the sample section: bounding or effective. For a color version of the figure, see www.iste.co.uk/jebahi/discrete.zip*

However, this criterion does not ensure inertia equality between the discrete and the continuous domains. To study the influence of this inequality, the results of simple 1D dynamic tests were analyzed. A set of discrete domains with aligned identical discrete elements are loaded to generate a resonance answer in tensile, bending and torsion modes (Figure 2.27).

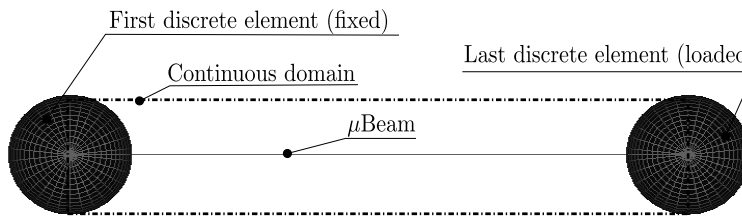

(a) Discrete domain made up of two aligned discrete elements

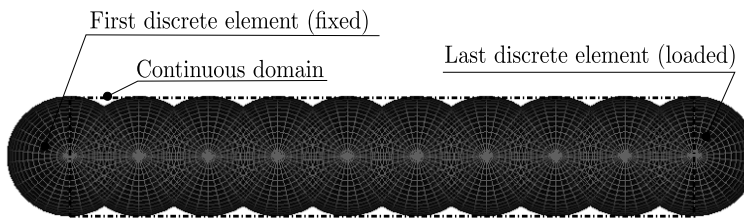

(b) Discrete domain made up of ten aligned discrete elements

Figure 2.27. *Illustration of simple 1D dynamic tests. For a color version of the figure, see www.iste.co.uk/jebahi/discrete.zip*

The oscillation periods are computed due to spectral analysis. The number of discrete elements is increased from 2 to 20 to study the convergence of the solution. For each mode, the analytical solution of oscillation period T associated with a clumped-free beam can be obtained using the material strength theory [SHA 97, section 4.1, section 4.2, section 4.3]:

$$T_{\text{tensile}} = 4\,L\sqrt{\frac{\rho}{E}} \qquad [2.27]$$

$$T_{\text{bending}} = \frac{2\,L^2}{\pi}\sqrt{\frac{\rho\,S}{E\,I}} \qquad [2.28]$$

$$T_{\text{torsion}} = 4\,L\sqrt{\frac{\rho}{G}} \qquad [2.29]$$

where:

– T_{tensile}, T_{bending} and T_{torsion} are the first mode oscillation periods of the clamped-free beam;

– E, G are the Young and shear moduli;

– ρ is the density;

– L, S, I are the length, the cross-section area and the second moment of area of the beam.

The discrete element density is computed so as to ensure mass equality between discrete and continuous domains:

$$\rho_\mu = \frac{3}{4}\frac{\rho\,L}{NR} \qquad [2.30]$$

where:

– N is the number of discrete elements;

– ρ_μ is the density of the discrete elements;

– R is the radius of the discrete elements.

In the case of 1D discrete domains, the parameter values of the cohesive beams are equal to those of the continuous domain:

$$E_\mu = E$$

$$\nu_\mu = \nu$$

$$r_\mu = R$$

The obtained results show that, in the case of:

– *tensile test* (Figure 2.28a), the numerical solution converges to the analytical solution.

– *bending test* (Figure 2.28b), the numerical solution converges to the analytical solution with a small difference. This error is due to material strength theory that neglects the rotational kinetic energy.

– *torsion test* (Figure 2.28c), numerical solution converges to the analytical solution with a difference of 10%. In this case, the rotational kinetic energy cannot be neglected, which explains the relatively large error.

The tensile and bending numerical results are in good agreement with the analytical solutions. Such an agreement is not as good in the case of torsion test, since 10% relative error is obtained between the numerical and analytical results. This error is due to computation of the discrete element density using mass equality between the discrete and continuous domains, rather than inertia equality. Using inertia equality, the discrete element density is computed as:

$$\rho_{\mu}^{\text{inertia}} = \frac{15}{16}\frac{\rho L}{N\,R} \qquad [2.31]$$

The ratio between the oscillation period using discrete element density computed with mass equality assumption ρ_{μ}^{mass} [2.30] and inertia equality assumption $\rho_{\mu}^{\text{inertia}}$ [2.31] is:

$$\frac{T_{\text{Torsion}}^{\text{mass}}}{T_{\text{Torsion}}^{\text{inertia}}} = \frac{4\,L\sqrt{\frac{\rho_{\mu}^{\text{mass}}}{G}}}{4\,L\sqrt{\frac{\rho_{\mu}^{\text{inertia}}}{G}}} = \sqrt{\frac{\frac{3}{4}\frac{\rho\,L}{N\,R}}{\frac{15}{16}\frac{\rho\,L}{N\,R}}}$$

$$\frac{T_{\text{Torsion}}^{\text{mass}}}{T_{\text{Torsion}}^{\text{inertia}}} = \sqrt{\frac{12}{15}} \approx 0,89 \qquad [2.32]$$

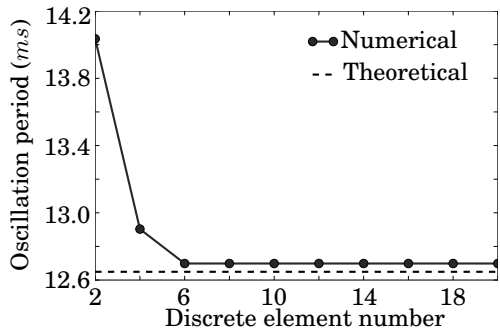

(a) Tensile

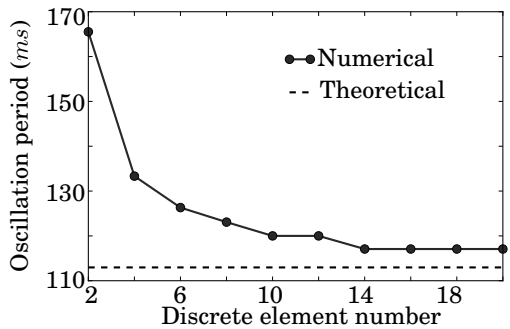

(b) Bending

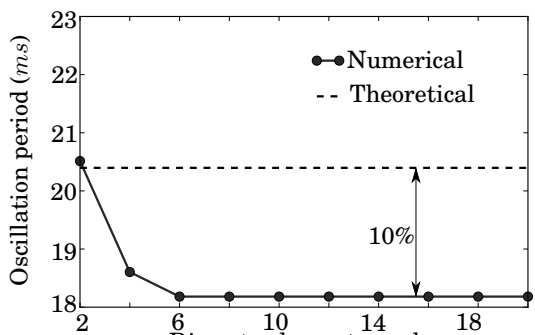

(c) Torsion

Figure 2.28. *Convergence study of oscillation periods*

Overall, the relative error in torsion results could be accepted in the framework of discrete element modeling, especially, as shown in Figures 2.20 and 2.29, the torsion energy does not contribute significantly in computation of the total energy.

In conclusion, the consequence of the error on the inertia computation, caused by the mass equality assumption, is not significant on the dynamic elastic response of the studied system. The mass equality can be used as a simple calibration method of the discrete element density.

2.4.3.2. *Validation*

The previous section considered simple 1D models to investigate the calibration method of the microscopic dynamic parameter (discrete element density). The present section attempts to validate the calibration results by simulation of dynamic tensile, bending, torsion and impact tests using 3D cylindrical discrete domains (Figure 2.16). The material of these domains is assumed to be silica glass whose the macroscopic elastic properties and their associated microscopic parameters are given by Tables 2.3 and 2.4, respectively. The silica glass density is $\rho_M = 2200\ kg/m^3$. The corresponding microscopic density is obtained using the mass equality assumption between discrete and continuous domains. The dimensions of the continuous domain are computed as explained in section 2.4.2.1.1.

Starting with dynamic tensile, bending and torsion tests, the boundary conditions and the loadings are applied such that the "xMin" face is fixed and the "xMax" face is loaded. The forces acting on "xMax" are applied progressively and suddenly set to 0. This loading allows us to excite the system dynamically. Based on spectral analysis, the numerical oscillation periods are obtained by averaging the positions of the discrete elements belonging to the free face ("xMax"). Numerical results are compared to theoretical results given by equations [2.27], [2.28] and [2.29].

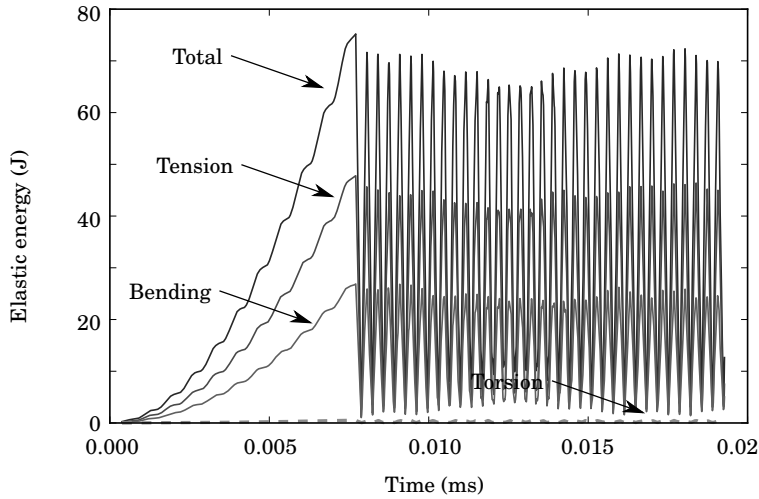

Figure 2.29. *Energy breakdown of total elastic energy stored by cohesive beams for a complex dynamic test (computed with a time step* $\Delta t = 3.10^{-7} s$ *and a number of iterations* $n = 50\,000$*). For a color version of the figure, see www.iste.co.uk/jebahi/discrete.zip*

For impact tests, an initial velocity on **X** is applied to the "xMin" face to generate a mechanical wave. "xMax" average velocity on **X** is measured at each time step. Incidentally, it is possible to capture the moment when the mechanical wave reach "xMax" face (Figure 2.30). Mechanical wave celerity is deduced with the elapsed time for the mechanical wave front to go through the numerical sample (Figure 2.31).

Table 2.6 shows relative comparison between simulation and theoretical results. Tensile, torsion and impact tests show very good adequacy with analytical results. The bending test shows less precision. The reason for this error is previously discussed and a solution is proposed in section 2.4.2.5.

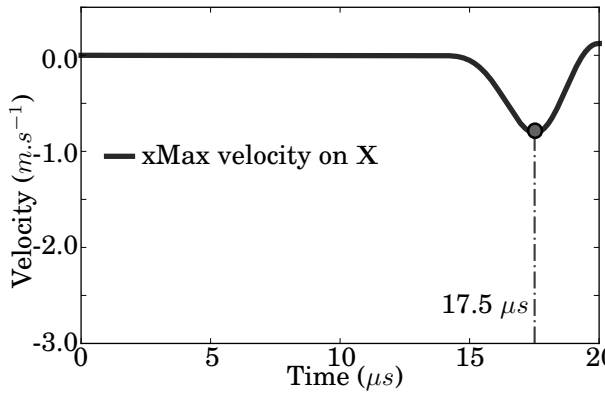

Figure 2.30. *"xMax" face average velocity as a function of time*

	Traction	Bending	Torsion	Impact
Criteria	Free face normal oscillation	Free face tangential oscillation	Free face rotational oscillation	Mechanical wave celerity
Difference	0.38 %	6.63 %	0.50 %	0.40 %

Table 2.6. *Comparison of the numerical and theoretical results for dynamic tensile, bending, torsion and impact tests*

2.5. Conclusion

The present chapter focuses on modeling of continuum mechanical behaviors using the hybrid lattice-particle method. Due to various difficulties, this method was, until very recently, used as a qualitative tool to understand complex phenomena such as wear, fracture or impact. This chapter aims to overcome these limitations by proposing a new variation of this method to model quantitatively continuous materials. In this variation, the studied material is represented by an agglomerate of spherical discrete elements connected by identical cylindrical cohesive beams.

In addition, a comprehensive methodology has been introduced to simplify application of this variation and

ensure a correct quantitative modeling of continuous materials. This methodology consists of four steps.

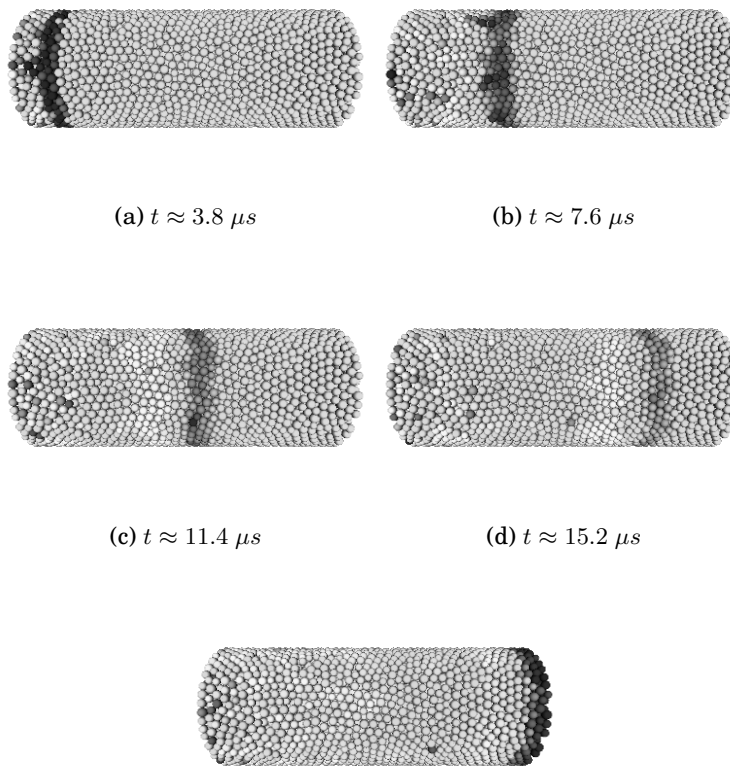

(a) $t \approx 3.8\ \mu s$ (b) $t \approx 7.6\ \mu s$

(c) $t \approx 11.4\ \mu s$ (d) $t \approx 15.2\ \mu s$

(e) $t \approx 19\ \mu s$

Figure 2.31. *Snapshots of mechanical wave propagation. For a color version of the figure, see www.iste.co.uk/jebahi/discrete.zip*

The first step concerns the construction of the discrete domain of the studied problem. As shown, building the initial discrete domain is a question of high level of interest. Indeed, the obtained discrete domain impacts greatly the associated

mechanical behavior. For example, a regular discrete domain can lead to an unexpected anisotropic behavior. This first step deals with this question and proposes a well-tested algorithm, the *cooker*, that can be used to correctly build the discrete representation of the studied material. A list of good-practices can be drawn from this step:

– The compacted domains must ensure a good level of geometrical isotropy to ensure mechanical isotropy. Then, ordered discrete domains must be prevented. To do so, a statistical distribution κ must be applied on the discrete element radii. In the case of uniform distribution [2.7], $\kappa = 25\%$ seems to promote the isotropy. The *cooker* algorithm proposed in this chapter has been proven to conduce to isotropy. If another method is used to generate the discrete element domain, isotropy must be verified with a 3D histogram, as shown in Figure 2.7.

– The compacted domains that model a same material must have same level of average coordination number (cardinal number) and volume fraction.

– The compacted domains must have a sufficient number of discrete elements N to ensure refining independence of the simulation results. It is demonstrated in this chapter that for a 3D discrete domain and beyond $N = 10,000$ the simulation results are weakly affected by this number.

The second step concerns the choice of the rheological model of the cohesive bonds used to link the adjacent discrete elements. To reproduce the linear elastic behavior of materials, cylindrical cohesive beam bonds were proposed. The mechanical behavior of these beams is described by the analytical Euler–Bernoulli theory. Only four parameters are required to completely describe their geometrical and mechanical properties: two geometrical parameters (length l_μ and radius r_μ) and two mechanical parameters (Young's modulus E_μ and Poisson's ratio ν_μ). These static parameters, in addition to the discrete element masses, are sufficient for

descibing the mechanical behavior of the studied problem. Except for l_μ which is imposed by the discrete element locations, all these parameters must be adjusted to ensure a correct macroscopic mechanical behavior.

The third step aims to address this point. An identification approach by calibration was proposed to identify the appropriate microscopic parameters. As in experimental identification, to determine the static microscopic parameters, quasistatic tensile tests were simulated using numerical samples having different static microscopic parameters. To simplify the calibration process, a parametric study was first done. As a result of this study, it has shown that the microscopic Poisson ratio ν_μ has no influence of the macroscopic mechanical behavior and can be fixed arbitrary. The microscopic Young modulus E_μ has influence only on the macroscopic Young modulus E_M. The microscopic radius ratio $\tilde{r_\mu}$ influences both E_M and ν_M. Therefore, this last parameter must be calibrated first to obtain the expected ν_M. Then, the parameter E_μ can be calibrated to match the expected E_M. As for the dynamic parameters (discrete element masses), these parameters can be replaced by only one parameter (simple to calibrate): the discrete element density ρ_μ which is assumed to be the same for all the discrete elements. As shown, this dynamic parameter can easily be determined by analytical calculation, using mass equality assumption between discrete and continuous domain.

The final step consists of implementation and application of the first three steps to simulate mechanical problems with the developed DEM variation. The obtained results have been quantitatively compared to experimental, analytical or other numerical results. As seen, these results are very promising to invest more in this direction.

This work is a first step in proposing a quantitative numerical tool able to quantitatively model those classes of problems that cannot be easily treated by classic numerical

approaches. Further developments will tackle more complex behaviors such as anisotropy, work hardening or densification, etc.

The next chapter attempts to apply the presented methodology to deal with another interesting aspect in mechanical engineering: thermal conduction in continuous materials.

3

Discrete Element Modeling of Thermal Behavior of Continuous Materials

3.1. Introduction

The temperature field plays a valuable role in almost any manufacturing process, such as machining, friction stir welding, etc. Due to the very strong dependence of metallurgical phenomena on this field, it critically influences the mechanical properties of the processed material. Consequently, the search for a realistic thermal simulation of these processes, including an accurate heat transfer modeling, is an issue of capital importance for the desired full control of manufacturing techniques. Predominantly, three fundamental modes of heat transfer can be distinguished:

– conduction which is defined as transfer of energy by diffusion between objects in physical contact;

– convection which is defined as transfer of energy between an object and its environment, due to fluid motion;

– radiation which is defined as transfer of energy by electromagnetic radiation generated from thermal motion of charged particles.

Discrete Element Method to Model 3D Continuous Materials, First Edition.
Mohamed Jebahi, Damien André, Inigo Terreros and Ivan Iordanoff.

Conduction is the most significant means of heat transfer within a solid or between solids in physical contact. In continuous materials, this mode can be described by using the Fourier equation which was first proposed in 1822 [FOU 22]. This equation can be written in the case of constant conductivity as:

$$\frac{\partial \Theta}{\partial t} = \frac{\lambda}{\rho\, c_p}\left(\frac{\partial^2 \Theta}{\partial x^2} + \frac{\partial^2 \Theta}{\partial y^2} + \frac{\partial^2 \Theta}{\partial z^2}\right) \qquad [3.1]$$

where Θ denotes the temperature field, λ is the thermal conductivity, ρ is the density of the considered material, c_p is the specific heat and t represents the time. Solving this equation analytically is only possible for few geometrically simple problems [CRA 56]. In the general case, it is often necessary to have recourse to numerical approaches to provide an approximate solution for this equation. In particular, continuum approaches have been widely applied to this end, due to their natural adaptation to partial differential equations.

In tooling processes, regions with high thermal gradients and heat fluxes are often located near the tool-piece contact. In the contact area, continuum approaches have difficulty to accurately describe the emerged complex phenomena, such as fracture [TAV 06], dry sliding contact with a third body presence [RIC 08], high strains and temperature gradients. As for the discrete element method (DEM), this approach provides a good alternative to continuum methods to locally treat these phenomena.

If solutions have been proposed to apply DEM for simulation of continuum mechanical phenomena, application of this method to simulate thermal problems has until recently been restricted to granular materials [RIC 08, VAR 01, VAR 02b, VAR 02a, VAR 03, VAR 07]. Lately, Hahn *et al.* [HAH 11] have applied this method to

model 2D continuum thermal behaviors. This chapter attempts to extend this work to 3D continuous materials.

The previous chapter has presented a general methodology to model continuous materials from a mechanical point of view. Based on this methodology, the present chapter describes a method for simulating isotropic heat conduction through a 3D continuum material, using the DEM.

3.2. General description of the method

3.2.1. *Characterization of field variable variation in discrete domain*

To introduce the main concept of the heat conduction method, a discrete domain created exclusively with spherical discrete elements is considered (Figure 3.1). As shown in Figure 3.1, only contacts between particles are considered in the heat conduction calculations. The cohesive beams can only be used to identify, in a rapid and focused manner, the contacts between the discrete elements, or also to perform thermo-mechanical coupling.

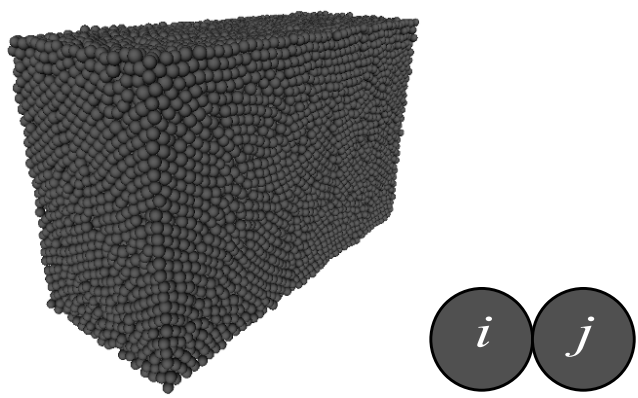

Figure 3.1. *Discrete domain for thermal conduction modeling. For a color version of the figure, see www.iste.co.uk/jebahi/discrete.zip*

To find the variation of a given field variable throughout a discrete domain, there are two main steps to follow, as explained in [VAR 01]:

– for each discrete element, the variations of the considered field variable due to interaction of this discrete element with each of its neighbors must be analyzed and stored separately;

– the stored variations associated with each discrete element must be summed to obtain the global field variable variations (at the discrete elements).

These steps can be translated mathematically into:

$$G_i = \sum_{j=1}^{N_{neigh}} g_{ij} \qquad [3.2]$$

where G_i is the global variation of the considered field variable at the discrete element i, g_{ij} is the variation of this field at i due to its interaction with the discrete element j and N_{neigh} is the total number of neighboring discrete elements of i.

3.2.2. *Application to heat conduction*

In the particular case of heat conduction, transferred heat between two discrete elements at a given instant, W_{ij}, can be calculated using Fourier's law as follows:

$$W_{ij} = S_t \, \lambda \, \frac{(\theta_j - \theta_i)}{l_{ij}} \qquad [3.3]$$

where S_t is the heat transmission surface area, $(\theta_j - \theta_j)$ is the temperature difference between discrete element i and discrete element j, λ is the material heat conductivity and l_{ij} is the distance between discrete element i and discrete element j. Furthermore, the thermal energy gain of a discrete

element i, ΔE_i, can be calculated as a function of its rise in temperature as follows:

$$\Delta E_i = c_p \, \rho_{\mu_i} \, V_i \, \Delta\theta_i$$

where c_p is the specific thermal capacity of the discrete element, ρ_{μ_i} represents the density of the discrete element i, V_i is the volume and $\Delta\theta_i$ is the rise in temperature at a discrete element i. The time derivative of this thermal energy gain represents the heat being transferred to discrete element i:

$$\frac{\Delta E_i}{\Delta t} = W_{ij} = \frac{c_p \, \rho_{\mu_i} \, V_i \, \Delta\theta_i}{\Delta t} \qquad [3.4]$$

If the time step Δt is small enough to consider $(\theta_j - \theta_i)$ constant during the time step, equations [3.3] and [3.4] can be combined to obtain the temperature rise of discrete element i due to its interaction with a neighbor j:

$$\Delta\theta_i = \frac{(\theta_j - \theta_i) \, S_t \, \lambda}{l_{ij} \, c_p \, \rho_{\mu_i} \, V_i} \Delta t \qquad [3.5]$$

Finally, equation [3.2] is used to obtain the total variation of the temperature at the discrete element i, $\Delta\Theta_i$, after the time step Δt:

$$\Delta\Theta_i = \sum_{j=1}^{N_{neigh}} \Delta\theta_j \qquad [3.6]$$

3.3. Thermal conduction in 3D ordered discrete domains

In the work by Hahn *et al.* [HAH 11], an approach to predict the temperature field in 2D discrete domains formed by hexagonal discrete elements was developed. Using the concepts introduced in the previous section, the present

section extends this approach to 3D ordered discrete domains formed by identically sized spherical discrete elements placed following a *simple cubic* crystal pattern. Figure 3.2 represents an illustration of this discrete domain. To fill all of the domain volume, each discrete element i is represented by a cube of continuous material whose volume equals $V_i = (2R)^3$. Equation [3.5] can be modified for the particular case of the crystal domain presented in Figure 3.2 as follows. The mass of each discrete element is supposed to be equal to the mass of the associated cubic volume. In this case, the discrete element density ρ_μ, which is same for all the discrete elements, is linked to the material density ρ_M by means of the volume fraction f_v as follows:

$$\rho_\mu = \frac{\rho_M}{f_v} = \frac{V_{cube}}{V_{sph}}\rho_M = \frac{8R^3}{4/3\ \pi\ R^3}\rho_M = \frac{6}{\pi}\rho_M \qquad [3.7]$$

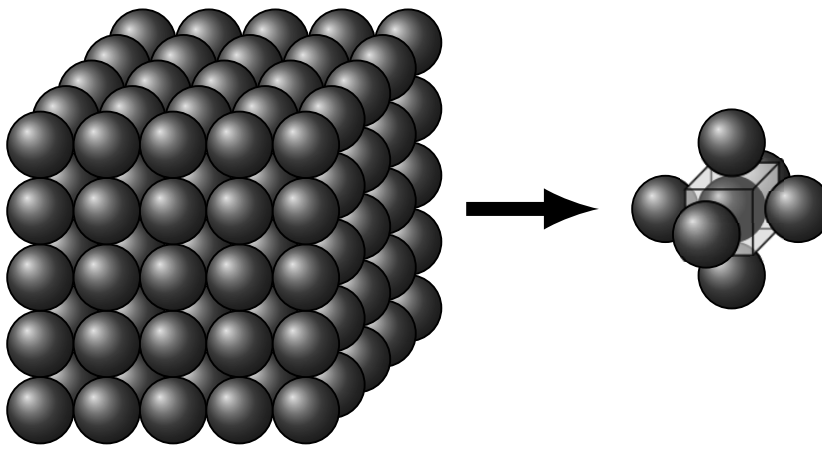

Figure 3.2. *3D crystal domain and example of a random particle with six neighbors. The volume represented by each discrete element is* $2R \times 2R \times 2R = 8R^3$

Let us consider the transmission surface to be equal to the surface of the cube face $S_t = 4R^2$ and the distance between discrete elements equal to the cube side $l_{ij} = 2R$. In this case,

equation [3.5] becomes:

$$\Delta\theta_i = \frac{(\theta_j - \theta_i)\ S_t\ \lambda}{l_{ij}\ c_p\ \rho_\mu\ V_{sph}}\ \Delta t = \frac{(\theta_j - \theta_i)\ (4R^2)\ \lambda}{(2R)\ c_p\ \rho_M\ (V_{cube}/V_{sph})\ V_{sph}}\ \Delta t$$
$$= \frac{\lambda}{c_p\ \rho_M}\ \frac{(\theta_j - \theta_i)}{(2R)^2}\ \Delta t \qquad [3.8]$$

Inside the discrete domain, the discrete elements have on average six neighbors. Considering a discrete element i with its neighbors (Figure 3.3), the total temperature variation at this element is given by:

$$\Delta\Theta_i = \sum_{j=1}^{6} \Delta\theta_j$$
$$= \frac{\lambda}{\rho_M\ c_p} \frac{(\theta_1 + \theta_2 + \theta_3 + \theta_4 + \theta_5 + \theta_6 - 6\theta_i)}{(2R)^2} \Delta t \qquad [3.9]$$

or also,

$$\Delta\Theta_i = \frac{\lambda}{\rho_M\ c_p}$$
$$\times \left(\frac{\theta_1 + \theta_2 - 2\theta_i}{(2R)^2} + \frac{\theta_3 + \theta_4 - 2\theta_i}{(2R)^2} + \frac{\theta_5 + \theta_6 - 2\theta_i}{(2R)^2} \right) \Delta t \qquad [3.10]$$

which is an exact fit to the finite central difference stencil for the 3D heat equation [3.1] with a mesh size equal to $2R$:

$$\frac{\partial\Theta}{\partial t} = \frac{\lambda}{\rho_M\ c_p} \left(\frac{\partial^2\Theta}{\partial x^2} + \frac{\partial^2\Theta}{\partial y^2} + \frac{\partial^2\Theta}{\partial z^2} \right) \approx$$
$$\approx \frac{\lambda}{\rho_M\ c_p} \left(\frac{\theta_1 + \theta_2 - 2\theta_i}{(2R)^2} + \frac{\theta_3 + \theta_4 - 2\theta_i}{(2R)^2} + \frac{\theta_5 + \theta_6 - 2\theta_i}{(2R)^2} \right)$$

In summary, the use of equation [3.2] to describe heat conduction through a 3D continuous material modeled with an ordered discrete domain as shown in Figure 3.2 fits a central difference stencil if:

– the mass of each discrete element is equal to the mass of the associated volume in the discretized continuous material (cubic volume in the given example);

– the transmission surface of each discrete element is equal to the area of the faces of the associated volume.

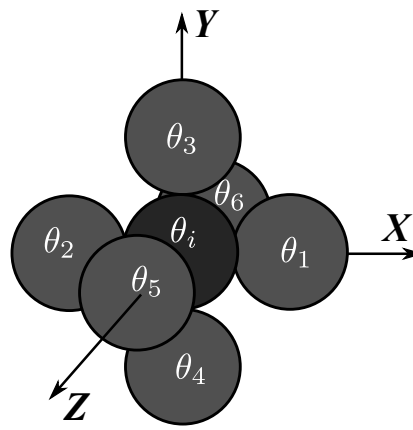

Figure 3.3. *Six discrete elements around an internal discrete element i. For a color version of the figure, see www.iste.co.uk/jebahi/discrete.zip*

However, application of this equation on disordered discrete domains is not straightforward. The next section attempts to address this issue.

3.4. Thermal conduction in 3D disordered discrete domains

To ease the coupling of the thermal and mechanical aspects of a simulation, both the thermal behavior and

mechanical behavior should work together using the same discrete domain. To perform quantitative simulation of a solid material by DEM, the previous chapter has shown that the discrete domain must verify some criteria related to compactness, homogeneity and isotropy (in terms of contact directions). To extend the general heat conduction method introduced in section 3.2.2 to this type of discrete domain (isotropic discrete domain), the items inferred in summary of the previous section will be assumed necessary, even if the structure of the 3D discrete domain is different.

The problem is that there is no geometrical method to find the volume fraction and the transmission surface associated with each discrete element (Figure 3.4). To circumvent this problem, the present chapter proposes a robust and numerically efficient method to obtain locally these parameters, ρ_μ and S_t [3.5], in 3D discrete domains. Such a method constitutes the main originality of the present work. As will be seen later, results obtained using this method are in agreement with the results of Hahn *et al.* [HAH 11] who have shown that local anisotropy in the thermal heat conductivity at small scales has no effect on the heat flux at the structure scale.

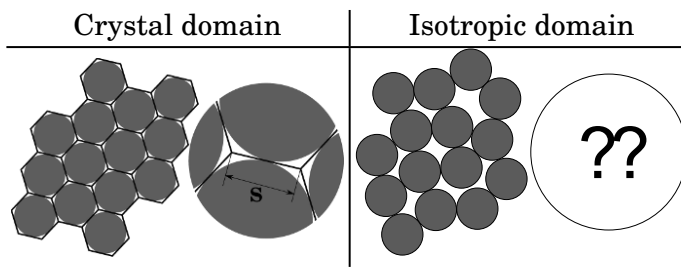

Figure 3.4. *2D example of a crystal (ordered) domain with known transmission surface and known volume fraction; and an isotropic discrete domain with unknown transmission surface and unknown volume fraction*

3.4.1. *Determination of local parameters for each discrete element*

To determine the transmission surface area and the discrete element density in an isotropic discrete domain, an equivalent platonic solid that depends on the number of neighbors is considered for each discrete element. Figure 3.5 shows an example of the equivalent platonic solid of a discrete element having six neighbors.

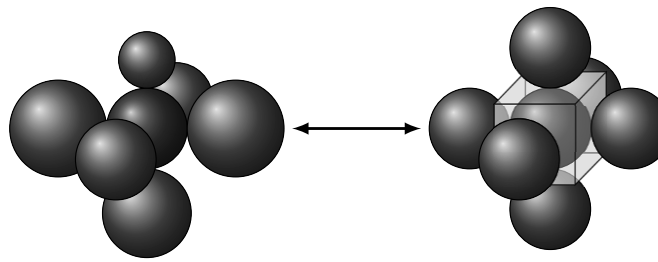

Figure 3.5. *Example of an equivalent platonic solid. For a color version of the figure, see www.iste.co.uk/jebahi/discrete.zip*

The transmission surface and the local volume fraction are calculated from this platonic solid. Note that due to random packing of discrete elements, the volume fraction may vary from one discrete element to another, since it depends on the number of discrete element neighbors. Consequently, the concept of *"local" volume fraction* will be used instead of the concept of *volume fraction* used before. Furthermore, dimensionless transmission surface $\tilde{S}_t$, defined as the ratio between the transmission surface S_t and the square of the considered discrete element radius R^2, will be preferred to S_t. This facilitates this parameter to be independent of the discrete element radii.

3.4.2. *Calculation of discrete element transmission surface*

As stated in section 3.4.1, a discrete element i is related to a regular polyhedron (platonic solid) by means of its number of neighbors. The number of surfaces of the chosen polyhedron is equal to the number of neighbors. Then, the area of the virtual polyhedron faces is calculated and used as the transmission surface of the considered discrete element i. In the cases where such a regular polyhedron does not exist, the transmission surface is chosen by linear interpolation (Figure 3.6). For the cases where the discrete element i is in contact with less than four neighbors, the slope is considered to be constant. In the example of Figure 3.5, in which six discrete elements are in contact with the discrete element of interest, the transmission surface area is considered to be four times the square of its radius $4R^2$, as shown in Figure 3.6 and in Table 3.1.

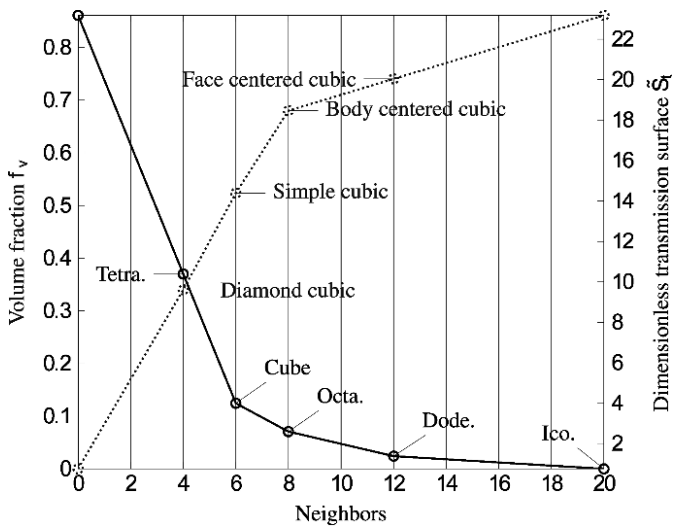

Figure 3.6. *Dimensionless transmission surfaces (solid curve) and volume fractions (dotted curve) as a function of the number of neighbors*

3.4.3. *Calculation of local volume fraction*

A similar method is used to calculate the volume fraction associated with each discrete element. The volume fraction of a given discrete element is chosen in the same way as the volume fraction of the associated crystal structure, which depends on the number of neighboring discrete elements. Just as in section 3.4.2, if the number of neighbors does not match any crystal structure, the local volume fraction is calculated using a linear interpolation (Figure 3.6). For the theoretical case where the discrete element has no neighbors, the local volume fraction is considered to be zero. Furthermore, when the discrete element of interest is in contact with more than 12 neighbors, the slope is considered to be constant. For instance, the discrete element shown in Figure 3.5 is assumed to occupy nearly 52.36% of the space, as is an atom in a *simple cubic* unit cell (Figure 3.7):

$$f_v = \frac{l^3}{(4/3)\pi R^3} = \frac{(2\,R)^3}{(4/3)\pi R^3} = \frac{6}{\pi} \approx 0.5236 \qquad [3.11]$$

where l is the side length of the equivalent platonic solid (cubic volume) and R is the radius of the discrete elements. Figure 3.6 and Table 3.1 give the results for other number of neighboring discrete elements (from 1 to 20 neighbors).

N_{neigh}	$\tilde{S}_t$	f_v	N_{neigh}	$\tilde{S}_t$	f_v
1	19,98076	0,08502	11	1,69019	0,72540
2	16,78460	0,17004	12	1,38757	0,74048
3	13,58845	0,25506	13	1,30888	0,75555
4	10,39230	0,34008	14	1,23020	0,77063
5	7,19615	0,43184	15	1,15152	0,78570
6	4,0	0,52359	16	1,07284	0,80078
7	3,29903	0,60188	17	0,99415	0,81586
8	2,59807	0,68017	18	0,91547	0,83093
9	2,29545	0,69525	19	0,83679	0,84601
10	1,99282	0,71032	20	0,75810	0,86109

Table 3.1. *Calculated values for $\tilde{S}_t$ and f_v as a function of the number of neighbors*

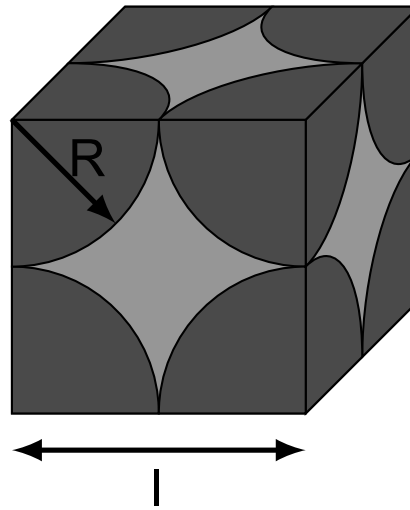

Figure 3.7. *Example of a simple cubic unit cell*

The methods described in the previous and present sections are numerically very efficient. The knowledge of the number of neighbors directly provides the transmission surface and local volume fraction that must be employed for the heat transfer calculation.

3.4.4. *Interactions between each discrete element and its neighbors*

Once the local volume fraction and transmission surface are obtained for each discrete element, some considerations must be taken into account to calculate the temperature rise. First, the heat exchange between any discrete element i and its neighbor j must be the same, irrespective of the identity of the discrete element of reference. This requirement means that the resultant amount of exchanged heat [3.3] must be the same, whether reference element i or element j is used in the calculation. This equivalence is achieved by averaging the parameter S_t from equation [3.3]. The transmission surface associated with the discrete element i can be obtained using

the dimensionless values presented in Table 3.1 as follows: $S_{t_i} = \tilde{S}_{t_i} R_i^2$. The equivalent transmission surface between this discrete element and its neighbor j is then given by: $S_{t_{ij}} = \sqrt{S_{t_i} S_{t_j}}$. On the contrary, the parameter f_v must not be averaged in such a way, because it determines the temperature rise of the discrete element and this variation depends on the properties of the discrete element itself and not on its interactions.

Taking into account the results of this section, and replacing ρ_{μ_i} with its expression (ρ_M / f_{v_i}, where f_{v_i} is the volume fraction of the discrete element i), equation [3.5] can be expressed as follows:

$$\Delta\theta_i = \frac{(\theta_j - \theta_i)\ S_{t_{ij}}\ \lambda\ f_{v_i}}{l_{ij}\ \rho_M\ c_p\ V_i} \Delta t \qquad [3.12]$$

Finally, the temperature variation, after a time step Δt, at a discrete element i belonging to an isotropic discrete domain can be obtained by summation of the local variations [3.12] due to interaction of this element with its neighbors as follows:

$$\Delta\Theta_i = \sum_{j=1}^{N_{neigh}} \Delta\theta_i = \sum_{j=1}^{N_{neigh}} \frac{(\theta_j - \theta_i)\ S_{t_{ij}}\ \lambda\ f_{v_i}}{l_{ij}\ \rho_M\ c_p\ V_i} \Delta t \qquad [3.13]$$

3.5. Validation

To validate the method described in the previous section, two types of thermal tests were simulated using isotropic discrete domains.

3.5.1. *Cylindrical beam in contact with a hot plane*

In the first case, the cylindrical domain shown in Figure 3.8, with an initial temperature of 298 K, is submitted to a boundary temperature of 798 K at the left-hand end

(located at $X = 0$). Further characteristics of the sample, which is assumed to be completely adiabatic, are given in Table 3.2. The results obtained with the DEM simulation are compared with analytical results obtained using the following equation [CRA 56]:

$$\Theta(x,t) = \Theta_{max} - \frac{4(\Theta_{max} - \Theta_{min})}{\pi} \sum_{n=0}^{\infty} \frac{(-1)^n}{2n+1} \times \cos \frac{(2n+1)\pi x}{2L} e^{\frac{-\lambda(2n+1)^2\pi^2 t}{c_p\ \rho\ 4L^2}} \quad [3.14]$$

with $\Theta_{max} = 798\,K$ and $\Theta_{min} = 298\,K$. Figure 3.9 presents this comparison. As can be seen, the numerical results are in good agreement with the analytical results, both at the beginning of the simulation when the greatest temperature gradient is found and at the end of the simulation when the temperature gradient is the smallest.

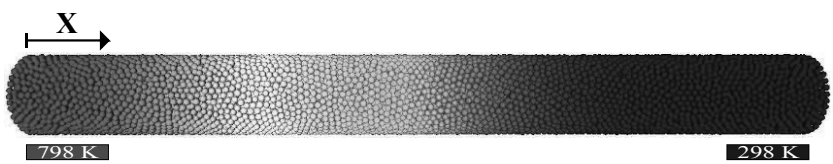

Figure 3.8. *Heat conduction in a cylindrical beam at a given time of the simulation. For a color version of the figure, see www.iste.co.uk/jebahi/discrete.zip*

3.5.2. *Dynamically heated sheet*

The second simulation aims to validate the heat conduction method developed in this chapter using complex thermal conditions, including high temperature gradients. A sheet was heated with a moving heat source whose characteristics are given in Table 3.3. The geometrical and thermal properties of this sheet are given in Figure 3.10 and

Table 3.4. It should be noted that this sheet whose thermal properties correspond to an aluminium alloy was allowed to reach elevated temperatures, actually causing material melting. The objective there would be to make this sheet in the same thermal conditions encountered during the friction stir welding (FSW) process. However, the material melting was not taken into account in the present simulation.

Parameter	Value
Length	$2.184\,\mathrm{mm}$
Radius	$0.116\,\mathrm{mm}$
Initial temperature	$298\,\mathrm{K}$
Density	$2.790\,\frac{\mathrm{kg}}{\mathrm{m}^3}$
Specific heat	$880\,\frac{\mathrm{J}}{\mathrm{kg\,K}}$
Thermal conductivity	$134\,\frac{\mathrm{W}}{\mathrm{m\,K}}$
Discrete elements	19.465
Element average radius	$8.998\,\mu\mathrm{m}$

Table 3.2. *Cylindrical beam characteristics*

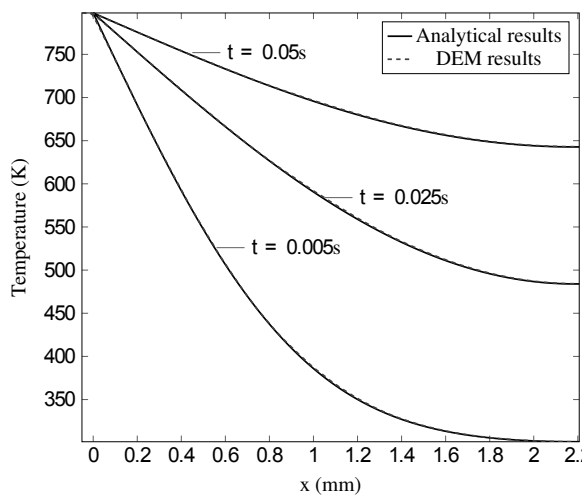

Figure 3.9. *Numerical and analytical temperature distributions at various times. For a color version of the figure, see www.iste.co.uk/jebahi/discrete.zip*

To control the heat propagation through this sheet, which is assumed to be completely adiabatic, local temperature evolutions were measured at three check-points (*A, B* and *C*). The coordinates of these check-points are given in Table 3.5. To test the convergence of the DEM calculations, different numbers of discrete elements were used to discretize the associated discrete domain: $1,000$, $5,000$ and $20,000$. Also, to obtain enough data to carry out statistical calculations, five discrete domains were created using the *cooker* algorithm (section 2.3.1) for each number of discrete elements. Thus, 15 different discrete domains were used in total. For each number of discrete elements, five sets of temperature evolutions were obtained at each check-point.

Parameter	Value
Diameter	$8\,\mathrm{mm}$
Height	$2\,\mathrm{mm}$
Velocity	$3.3\,\frac{\mathrm{mm}}{\mathrm{s}}$
Heat power	$10^{11}\,\frac{\mathrm{W}}{\mathrm{m}^3}$
Initial X position	$20\,\mathrm{mm}$

Table 3.3. *Heat source characteristics*

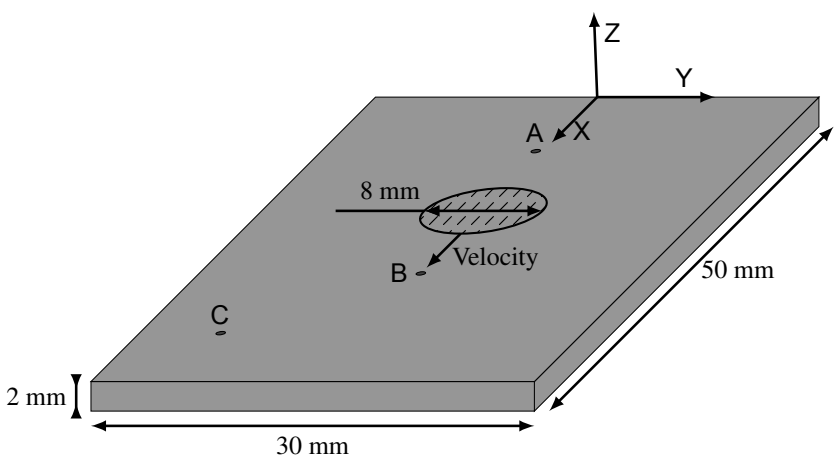

Figure 3.10. *Schema of the sheet used in calculations*

The relative dispersion e of these sets of temperature evolutions was computed for each number of discrete elements and at each check-point using the following equation:

$$e = \frac{1}{n} \sum_{p=1}^{n} \frac{\theta^p_{max} - \theta^p_{min}}{\theta^p_{max}} \qquad [3.15]$$

where $\theta^p_{max} = \underset{i=1,\ldots,5}{max} \{\theta^p_i\}$ and $\theta^p_{min} = \underset{i=1,\ldots,5}{min} \{\theta^p_i\}$, θ^p_i is the temperature of the discrete domain i at iteration p, and n is the total number of iterations. Figure 3.11 presents the values of e at the three check-points for each number of discrete elements. As obtained for the mechanical behavior, beyond $10,000$ discrete elements, the relative dispersion (obtained by interpolation) can be considered satisfactory (less than 6%). Furthermore, this parameter has a tendency to decrease with the number of discrete elements (less than 4% for $20,000$ discrete elements).

Parameter	Value
Length	$50\,\mathrm{mm}$
Width	$30\,\mathrm{mm}$
Height	$2\,\mathrm{mm}$
Initial temperature	$25\,^{\circ}\mathrm{C}$
Density	$2.790\,\frac{\mathrm{kg}}{\mathrm{m}^3}$
Specific heat	$880\,\frac{\mathrm{J}}{\mathrm{kg\,K}}$
Thermal conductivity	$134\,\frac{\mathrm{W}}{\mathrm{m\,K}}$

Table 3.4. *Sheet properties*

Check-point	x (mm)	y (mm)
A	9.5	-0.5
B	31.0	0.0
C	41.5	-9.5

Table 3.5. *Coordinates of the control points*

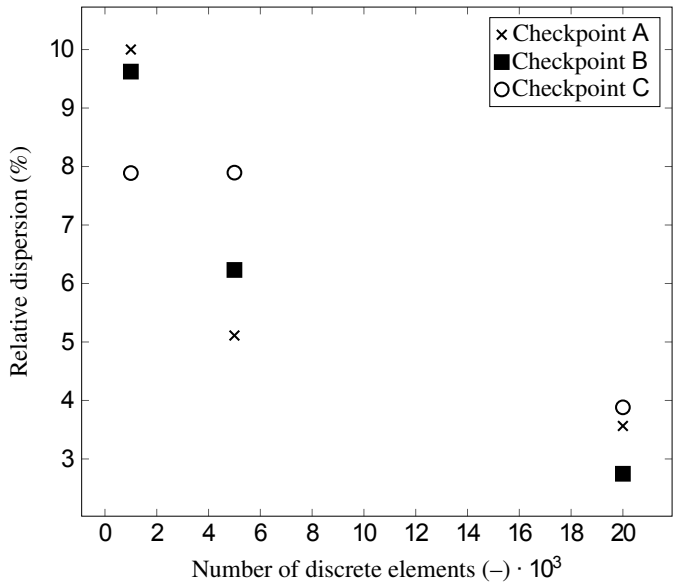

Figure 3.11. *Averaged relative dispersions of results obtained in the check-points for each type of domain*

To validate the DEM simulation, the results obtained with $20,000$ discrete elements were averaged and compared with other numerical results obtained with the finite element method (FEM) method using the *Abaqus 6.10*™ software. The FEM domain was meshed with cubic elements whose edges are 0.5 mm long. Figures 3.12a, 3.12b and 3.12c show this comparison. The maximal temperature difference was located in each figure, and the relative error between the FEM and DEM results was calculated at this point. Relatively small errors were obtained, which proves the validity of the developed heat conduction method.

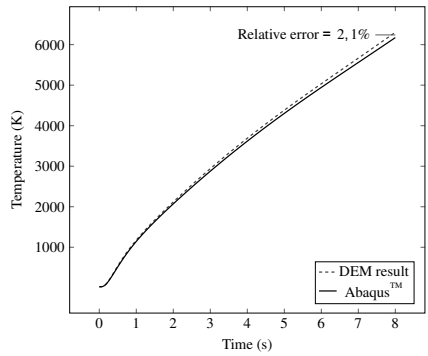

(a) Thermal field obtained at check-point A by the DEM and FEM.

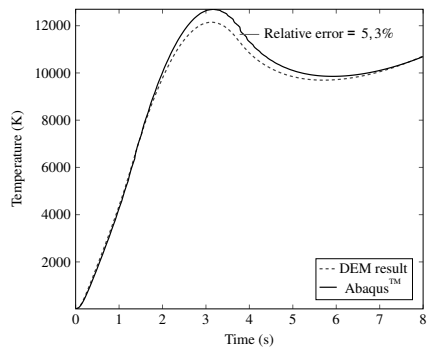

(b) Thermal field obtained at check-point B by the DEM and FEM.

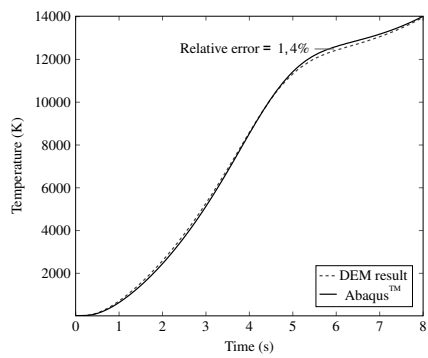

(c) Thermal field obtained at check-point C by the DEM and FEM.

Figure 3.12. *Thermal field obtained at different check-points by the DEM and FEM*

3.6. Conclusion

This chapter shows the way in which the DEM can be used to carry out complex heat conduction simulations using compact, homogeneous and isotropic (in terms of contact directions) discrete domains. The proposed method can be used to simulate conduction within continuous materials, and, for the first time, it is capable to deal with 3D models. This method can easily be coupled with the mechanical approach described in the previous chapter. Indeed, it is adapted for the same type of discrete domains that are used to carry out mechanical simulations.

The main originality of the presented heat conduction method is the way in which the volume fractions f_v and the transmission surfaces S_t of the discrete elements are treated to emerge the desired properties of the continuous materials under study. A virtual platonic solid is associated with each discrete element in the considered discrete domain. Only one parameter is required to define such a solid: the number of neighbors of the discrete element in question. This simple, fast and numerically efficient operation allows us to overcome all the problems created by the granular nature of the discrete domains, specially: (1) the problem of internal voids, related to the mass of the continuous material; and (2) the problem of contact surfaces between discrete elements, related to the internal conductivity of the continuous material.

To validate the developed heat conduction approach, it was applied to simulate two thermal tests. The first test is an academic test, for which analytical solution is available. The obtained DEM results for this test correlate very well with the analytical solutions. The second test is relatively complex and represents an initiation to simulation of a very complex manufacturing process: FSW. Comparison between results obtained by DEM simulation and FEM simulation (using *Abaqus 6.10*™ software) of such a test shows that the

developed approach is also applicable for complex thermal simulations involving high temperature gradients.

To reduce the calculation time, a long-term solution will consist of coupling the DEM with continuum approaches such as the FEM [ZIE 05a, ZIE 05b, ZIE 05c] or constrained natural element method (CNEM) [CHI 11, ILL 11, YVO 04]. Once again, the type of discrete domain used in this chapter makes this task easier.

4

Discrete Element Modeling of Brittle Fracture

4.1. Introduction

One of the most important problems in material science and engineering is fractures. For engineering materials, two possible types of fracture can be distinguished: ductile fracture and brittle fracture (Figure 4.1). The main difference between them can be attributed to the amount of plastic deformation (i.e. dislocation motion) that the material undergoes before fracture occurs. Ductile materials (e.g. low-carbon steels, aluminum, tungsten, etc.) undergo large amount of plastic deformation, while brittle materials (e.g. high-carbon steels, glass, ceramics, etc.) show little or no plastic deformation before fracture. Only brittle fracture is considered in this work. This means that all dissipation during the fracture process is associated directly with the creation of new free surfaces. This type of fracture is thought to be initiated under a tensile stress in mode I, as reported in the literature [LAW 93].

Discrete Element Method to Model 3D Continuous Materials, First Edition.
Mohamed Jebahi, Damien André, Inigo Terreros and Ivan Iordanoff.

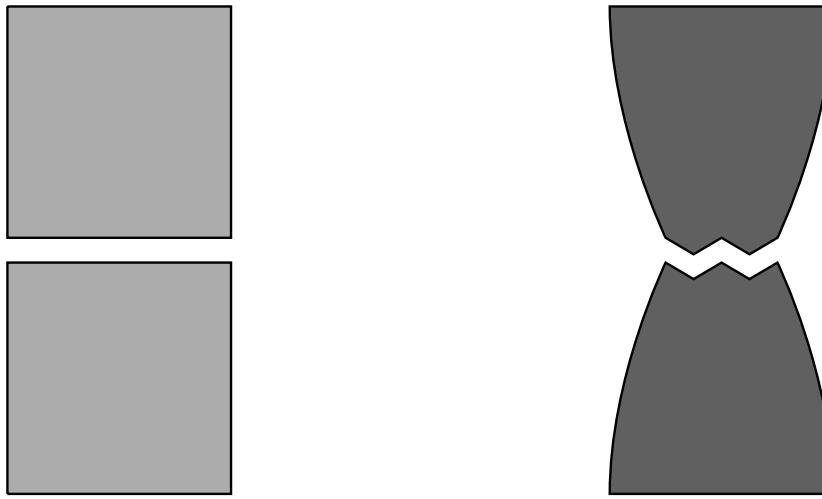

(a) Brittle fracture

(b) Ductile fracture

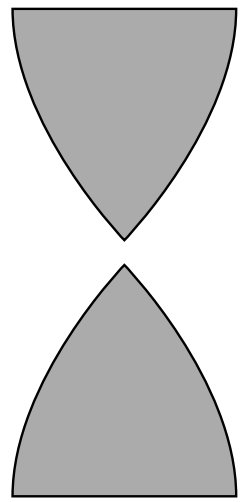

(c) Completely ductile fracture

Figure 4.1. *Difference between brittle fracture and ductile fracture*

Despite the great research effort, most of the complex fracture problems remain an ongoing challenge in computational mechanics. There exist several difficulties associated not only with the formulation of physically based models of material failure, but also with the numerical methods required to treat geometries that change in time (emergence of new free surfaces, singularities, etc.). Due to its discrete nature, the discrete element method (DEM) method presents a good candidate to model such problems, since it can naturally deal with emergent discontinuities that can occur in such problems. However, a major question encountered in DEM modeling of fracture is how to develop a fracture model able to quantitatively fit the fracture mechanisms experimentally observed, as reported in the literature [LAW 03, GRI 21]. Such a question has received a great deal of scientific interest over the years, which has led to the development of several fracture models. These models are presently widely applied to simulate various complex problems, such as tribology [RIC 07, IOR 08, TAN 09], impact [MAG 98, SHI 09] and fragmentation [D'AD 01, CAR 08] problems.

Most of the existent fracture models are based on a local description, i.e. at the bond (cohesive beam) level. These models give acceptable results at the macroscopic (structure) scale. However, as will be seen in the next section, in some cases, they are unable to correctly reproduce the cracking mechanisms at the microscopic scale, e.g. crack path. To overcome this limitation, a different model based on a non-local description is proposed in this book. By using individual cohesive beams, the new model computes averaging quantities (stresses) at the discrete elements, taking into account their neighbors. This model can be regarded as complementary to the existing models. Depending on the analysis scale and what is expected of the studied problem, one of these models can be chosen to model fractures.

In the following, the main concepts of one of the most commonly used local models as well as the newly proposed non-local model are detailed. To provide a quantitative study of these models, the silica glass which a typical brittle material is chosen as material of the numerical samples: the microscopic mechanical parameters of the cohesive beams linking the discrete elements are calibrated such that the associated macroscopic properties correspond to the silica glass.

4.2. Fracture model based on the cohesive beam bonds

The fracture models based on the cohesive beam bonds, also referred to as beam-based models, bond-based models, microscopic models or local fracture models, consider individual bonds (cohesive beams) to simulate fracture mechanisms. The main difference between these models lies in the way in which the fracture criterion is computed. Different criteria can be distinguished: maximal bond stress [POT 04], maximal bond strain [CAR 08] and maximal bond deformation energy. The maximal bond stress criterion is well adapted to study brittle fracture of materials, which is the subject of this chapter. The remainder of this section will focus on this criterion.

4.2.1. *Fracture criterion*

The maximal bond stress criterion presented here is derived from the Rankine criterion, which is widely applied to model brittle fracture. This criterion is based on the computation of the maximal principle stress in the beam bonds [POT 95]. Based on the Euler–Bernoulli beam theory, the maximal principle stress $\sigma_{\mu_{max}}$ (also known as equivalent Rankine stress) in a cohesive beam is given by:

$$\sigma_{\mu_{max}} = \frac{1}{2}\left(\sigma^n_{\mu_{max}} + \sqrt{\left(\sigma^n_{\mu_{max}}\right)^2 + 4\left(\tau_{\mu_{max}}\right)^2}\right) \qquad [4.1]$$

where $\sigma^n_{\mu_{max}}$ is the maximal normal stress (due to tensile and bending loadings) and $\tau_{\mu_{max}}$ is the maximal shear stress (due to torsion loading). Considering a cohesive beam connecting two discrete elements 1 and 2, the maximal normal stress in this beam can be obtained as follows:

$$\begin{aligned}
\sigma^n_{\mu_{max}} &= \sigma^{n^t}_{\mu_{max}} + \sigma^{n^b}_{\mu_{max}} \\
\sigma^{n^t}_{\mu_{max}} &= \frac{N_\mu}{S_\mu} \\
\sigma^{n^b}_{\mu_{max}} &= \frac{1}{2}\,\|\mathbf{M_{DE1}} + \mathbf{M_{DE1}}\|\,\frac{r_\mu}{I_\mu}
\end{aligned} \qquad [4.2]$$

where:

– $\sigma^{n^t}_{\mu_{max}}$ is the maximal normal stress due to tensile loadings;

– $\sigma^{n^b}_{\mu_{max}}$ is the maximal normal stress due to bending loadings;

– $S_\mu = \pi\, r_\mu^2$ is the section of the cohesive beam;

– r_μ is the beam radius;

– $I_\mu = \frac{\pi\, r_\mu^4}{4}$ is the moment of inertia along $\mathbf{Y}$ and $\mathbf{Z}$;

– $N_\mu = E_\mu\, S_\mu\, \frac{\Delta l_\mu}{l_\mu}$ is the normal force in the cohesive beam (E_μ is the microscopic Young's modulus);

– $\mathbf{M_{DE1}}$ and $\mathbf{M_{DE2}}$ are the beam torque reactions acting on discrete elements 1 and 2, respectively. Their expressions are given by [2.11] and [2.12], respectively.

The maximal shear stress in the considered cohesive beam is expressed as:

$$\tau_{\mu_{max}} = \frac{1}{2}\,\frac{r_\mu}{Io_\mu}\,(\mathbf{M_{DE1}} - \mathbf{M_{DE2}})\,.\mathbf{X} \qquad [4.3]$$

where $Io_\mu = \frac{\pi\, r_\mu^4}{2}$ is the polar moment of inertia. Assuming $M_{\mu x}$, $M_{\mu y}$ and $M_{\mu z}$ are, respectively, the torsional moment

along **X**, the bending moment along **Y** and the bending moment along **Z** in the cohesive beam, the equivalent Von-Mises stress can be rewritten as:

$$\sigma\mu max = \frac{1}{2}\left[\left(\frac{r\mu}{2\,I\mu}\sqrt{M\mu y2 + M\mu z2} + \frac{N\mu}{S\mu}\right) + \sqrt{\left(\frac{r\mu}{2\,I\mu}\sqrt{M\mu y2 + M\mu z2} + \frac{N\mu}{S\mu}\right)2 + 4\left(\frac{r\mu\,M\mu x}{Io\mu}\right)2}\right] \quad [4.4]$$

The proposed fracture criterion postulates that if the maximal principal stress in a cohesive beam $\sigma_{\mu_{max}}$ is larger than a certain critical value σ_{μ_f}, the considered beam is destroyed. The critical value σ_{μ_f}, called microscopic fracture stress, is to be determined by calibration.

4.2.2. *Calibration*

To calibrate the critical value σ_{μ_f}, quasi-static tensile tests were simulated using the same geometric model (cylindrical beam) that was used in the calibration of the microscopic mechanical properties of the cohesive beams (Figure 2.16). However, as in experimental fracture tests, the present simulations are displacement controlled. This facilitates the cracking mechanisms to evolve more rapidly, and then the "clean" fracture can properly be distinguished. Instead of applying tensile forces, displacements U_x and $-U_x$ are progressively applied on the opposite ends of the numerical sample "xMax" and "xMin" (Figure 2.16) until "clean" fracture occurs, i.e. until a sudden rise in the number of broken cohesive beams appears. Figure 4.2 illustrates the evolution of the number of the broken cohesive beams during a tensile test for an arbitrarily chosen σ_{μ_f}. The "clean" fracture can easily be identified by the sudden rise of this number.

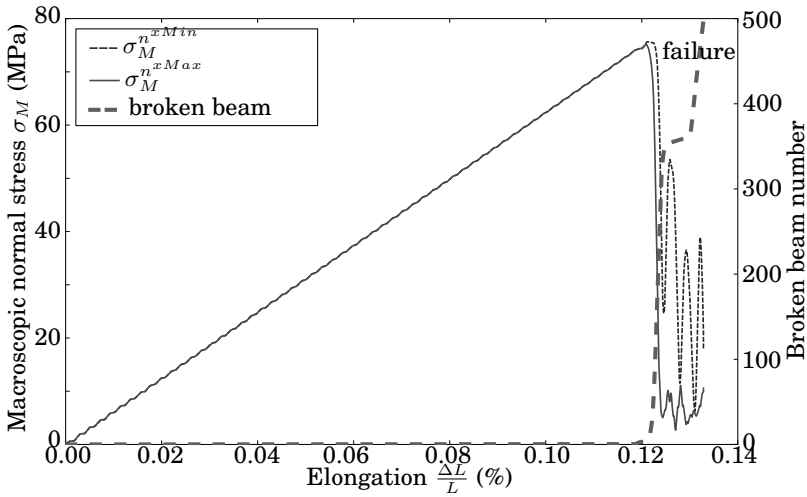

Figure 4.2. *Evolution of the number of the broken cohesive beams and the macroscopic normal stresses measured the end faces of the numerical sample. For a color version of the figure, see www.iste.co.uk/jebahi/discrete.zip*

To compute the macroscopic fracture stress σ_{M_f}, numerical sensors were implemented on the discrete elements belonging to the faces "xMax" and "xMin". These sensors record the forces $\mathbf{F_p}$ and torques $\mathbf{M_p}$ exerted on these elements. Thus, it is possible to compute the macroscopic normal forces applied on "xMin" and "xMax" as follows:

$$N_M^{xMin} = \sum_{p=1}^{N_{xMin}} \mathbf{F_p}.\mathbf{X} \qquad [4.5]$$

$$N_M^{xMax} = \sum_{p=1}^{N_{xMax}} \mathbf{F_p}.\mathbf{X} \qquad [4.6]$$

where N_{xMin} and N_{xMax} are the numbers of discrete elements belonging to "xMin" and "xMax", respectively. Using these

last equations, the macroscopic normal stresses at "xMax" and "xMin" can be obtained:

$$\sigma_M^{n^{xMin}} = \frac{N_M^{xMin}}{S_M} \quad [4.7]$$

$$\sigma_M^{n^{xMax}} = \frac{N_M^{xMax}}{S_M} \quad [4.8]$$

As shown in Figure 4.2, evolution of these quantities ($\sigma_M^{n^{xMin}}$ and $\sigma_M^{n^{xMax}}$) during a tensile test shows:

– very good agreement between these quantities before fracture occurs. Their evolution after fracture is due to the mechanical shock wave generated by sudden separation of the right sample part from the left one: elastic energy stored in the cohesive beams is released and transferred into kinetic energy; the crack, not being initiated at the center, causes the observed dissymmetry of $\sigma_M^{n^{xMin}}$ and $\sigma_M^{n^{xMax}}$ after fracture;

– rapid decrease in the macroscopic normal stresses beyond certain values, indicating the occurrence of "clean" fracture.

The macroscopic normal stress σ_M, which is assumed to be constant along the numerical sample, can be approximated as the average of $\sigma_M^{n^{xMin}}$ and $\sigma_M^{n^{xMax}}$:

$$\sigma_M^n = \left(\sigma_M^{n^{xMin}} + \sigma_M^{n^{xMax}}\right)/2 \quad [4.9]$$

Using the Rankine criterion, the macroscopic fracture stress which is none other than the maximal macroscopic principal stress can be expressed as:

$$\sigma_{M_f} = (\sigma_M^n)_{fracture} \quad [4.10]$$

where $(\sigma_M^n)_{fracture}$ is the macroscopic normal stress measured at the fracture of the numerical sample. The calibration process aims to research the appropriate microscopic fracture

stress σ_{μ_f} that ensures correct macroscopic fracture behavior: the macroscopic fracture stress σ_{M_f} obtained numerically must correspond to the one measured experimentally. Several numerical tests with different σ_{μ_f} have been performed, from which the corresponding σ_{M_f} have been determined. Furthermore, to take into account the dispersion of results due to the geometric discretization, four numerical samples have been prepared for each σ_{μ_f} value. Figure 4.3 shows the calibration results. A linear relationship is obtained between σ_{M_f} and σ_{μ_f}. Based on these results, the calibrated value of σ_{μ_f} corresponding to the silica glass whose macroscopic fracture stress is $\sigma_{M_f}^{Silica} = 50\,\mathrm{MPa}$ can be deduced: $\sigma_{\mu_f}^{Silica} = 292\,\mathrm{MPa}$.

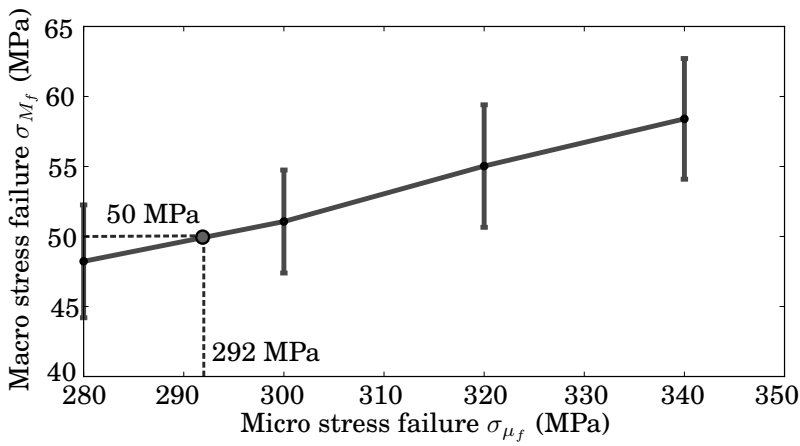

Figure 4.3. *Calibration of the microscopic fracture stress σ_{μ_f} of silica glass*

4.2.3. *Convergence study*

The influence of the number of discrete elements N, used to discretize the geometric model, on the macroscopic fracture criterion σ_{M_f}, was investigated in the same way as the elastic parameters. Figure 4.4 shows the evolution of σ_{M_f} as a

function of this number, for a fixed $\sigma_{\mu_f}^{Silica} = 292\,\mathrm{MPa}$. Beyond $N = 10,000$, σ_{M_f} is varying within 10% around an average value. This dispersion is larger than that obtained for the elastic parameters (Figure 2.25). Contrary to elastic phenomena, fractures are a local phenomenon for which crack initiation is attributed to the presence of local defects in the regions subjected to severe stresses. Therefore, the macroscopic fracture stress is more sensitive than the elastic parameters to the local beam arrangements which vary from one sample to another. However, this dispersion, which is lower than the dispersion obtained by Hentz *et al.* [HEN 04a], could be accepted, more so because it decreases as the number of discrete elements increases. As elastic parameters, the calibrated microscopic fracture stress σ_{μ_f} can be used for any discrete domain, provided that a sufficient number of discrete elements is used and the associated discrete domain is prepared as explained in section 2.3.

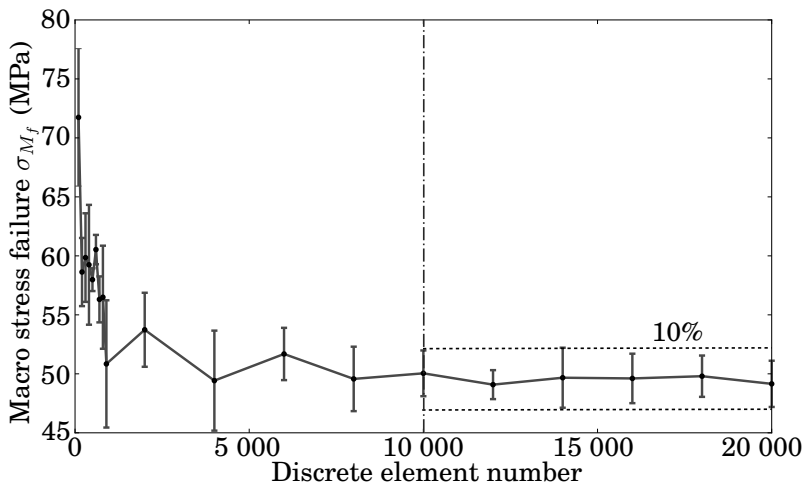

Figure 4.4. *Evolution of the macroscopic fracture stress σ_{M_f} as a function of the number of discrete elements*

4.2.4. *Validation*

To validate this model, it was applied to simulate several quasi-static reference tests. The microscopic fracture stress σ_{μ_f} is fixed at $292\ \mathrm{MPa}$, which corresponds to the macroscopic fracture stress of silica glass.

4.2.4.1. *Quasi-static bending of a 3D beam*

Figure 4.5 presents the discrete domain used to simulate the quasi-static bending test. A parallelepiped beam was preferred to a cylindrical beam. Indeed, by using a cylindrical beam, the region of maximum stress is reduced to a single line, which requires very fine discretization to ensure a sufficient number of discrete elements in this region (Figure 4.6). In contrast, by using a parallelepiped beam, this region extends over a rectangle, easy to capture by relatively coarse discretization (Figure 4.6).

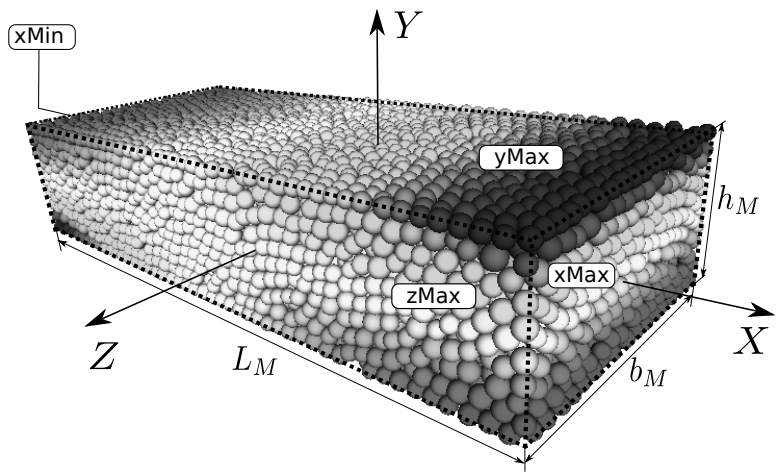

Figure 4.5. *Discrete domain for the quasi-static bending test. For a color version of the figure, see www.iste.co.uk/jebahi/discrete.zip*

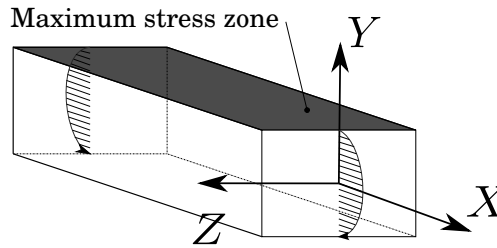

(a) Parallelepiped sample

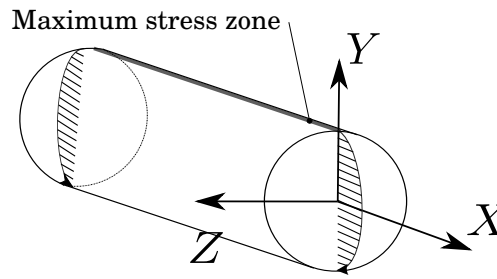

(b) Cylindrical sample

Figure 4.6. *Zones of maximum stress in parallelepiped and cylindrical numerical samples submitted to bending loading*

Rotations ϕ_z and $-\phi_z$ are progressively applied about the **Z** axis on the beam ends "xMin" and "xMax" until a "clean" fracture occurs. To compute the macroscopic fracture stress σ_{M_f}, it is necessary to measure the macroscopic bending torque (about the **Z** axis) M_{Mz}, which is assumed to be constant along the studied beam. To do so, the forces $\mathbf{F_p}$ and torques $\mathbf{M_p}$, applied on the discrete elements belonging to "xMax" and "xMin", were measured with the help of numerical sensors. Using these quantities, the bending torque can be obtained:

$$M_{Mz}^{xMin} = \sum_{p=1}^{n_{xMin}} \left(\mathbf{M_p} + \mathbf{O_1G_p} \wedge \mathbf{F_p}\right).\mathbf{Z} \qquad [4.11]$$

$$M_{Mz}^{xMax} = \sum_{p=1}^{n_{xMax}} \left(\mathbf{M_p} + \mathbf{O_2G_p} \wedge \mathbf{F_p}\right).\mathbf{Z} \quad [4.12]$$

$$M_{Mz} = \left(M_{Mz}^{xMin} + M_{Mz}^{xMax}\right)/2 \quad [4.13]$$

where O_1 and O_2 are the centers of, respectively, the faces "xMin" and "xMax". The maximal macroscopic normal stress $\sigma_{M_{max}}^{n}$ can be deduced from [4.13] as follows:

$$\sigma_{M_{max}}^{n} = \frac{M_{Mz}}{Iz}\frac{h_M}{12} \quad [4.14]$$

where Iz is the moment of inertia along the **Z** axis. Its expression is given by:

$$Iz = \frac{b_M\, h_M^3}{12} \quad [4.15]$$

where h_M and b_M are the dimensions of the numerical sample along **Y** and **Z**, respectively. The macroscopic fracture stress is then defined according to the Rankine criterion as:

$$\sigma_{M_f} = \left(\sigma_{M_{max}}^{n}\right)_{fracture} \quad [4.16]$$

where $\left(\sigma_{M_{max}}^{n}\right)_{fracture}$ is the maximal macroscopic normal stress measured at the fracture of the numerical sample.

Table 4.1 summarizes the results of the macroscopic fracture stress obtained from simulation of bending tests using four different numerical samples discretized with approximately $10,000$ discrete elements. These results are in good agreement with those obtained from tensile tests (with a margin of 6.5% error). Furthermore, the crack geometry seems in accordance with the brittle fracture theory (Figure 4.7). Indeed, the fracture surface is perpendicular to the neutral axis of the numerical sample (beam).

Sample	Tensile (MPa)	Bending (MPa)	Torsion (MPa)
No. 1	53.6	55.8	49.7
No. 2	48.6	55.6	52.1
No. 3	53.2	52.9	53.2
No. 4	51.8	56.4	51.3
Average	51.8	55.2	51.6
Difference	*Reference*	6.5 %	0.3 %

Table 4.1. *Comparison of the results of the macroscopic fracture stress obtained from tensile, bending and torsion tests: four discrete domains consisted of approximately* $10,000$ *discrete elements*

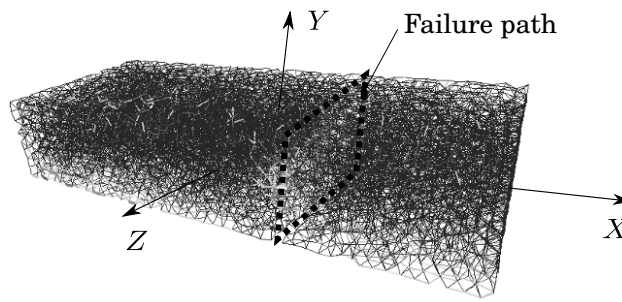

Figure 4.7. *Illustration of the crack morphology obtained from bending test*

4.2.4.2. *Quasi-static torsion of a 3D beam*

Figure 4.8 presents the geometric model used to simulate the quasi-static torsion test. A cylindrical beam, similar to that used in the calibration of the elastic parameters, is subjected to progressive rotations ϕ_x and $-\phi_x$ about the **X** axis on, respectively, "xMin" and "xMax" end faces.

To compute the macroscopic fracture stress, the forces $\mathbf{F_p}$ and torques $\mathbf{M_p}$, applied on the discrete elements belonging

to “xMin” and “xMax”, are measured. The macroscopic torsion torque M_{Mx} can be obtained from these quantities as follows:

$$M_{Mx}^{xMin} = \sum_{p=1}^{N_{xMin}} \left(\mathbf{M_p} + \mathbf{O_1G_p} \wedge \mathbf{F_p}\right).\mathbf{X} \qquad [4.17]$$

$$M_{Mx}^{xMax} = \sum_{p=1}^{N_{xMax}} \left(\mathbf{M_p} + \mathbf{O_2G_p} \wedge \mathbf{F_p}\right).\mathbf{X} \qquad [4.18]$$

$$M_{Mx} = \left(M_{Mx}^{xMin} + M_{Mx}^{xMax}\right)/2 \qquad [4.19]$$

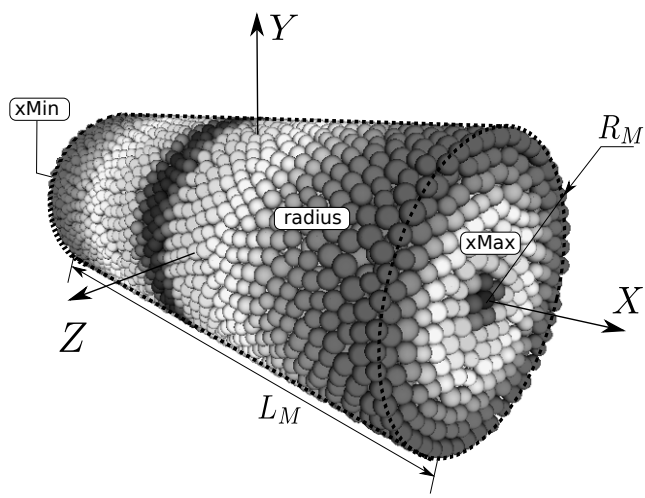

Figure 4.8. *Discrete domain for the quasi-static torsion test. For a color version of the figure, see www.iste.co.uk/jebahi/discrete.zip*

Based on the material strength theory, the maximal macroscopic shear stress can be obtained from [4.19] as:

$$\tau_{M_{max}} = \frac{M_{Mx}}{Io} R_M \qquad [4.20]$$

where R_M is the radius of the discrete domain and Io is the polar moment of inertia, which is defined as:

$$Io = \frac{\pi R_M^4}{2} \qquad [4.21]$$

Using the Rankine criterion, the macroscopic fracture stress which is none other than the maximal macroscopic principal stress can be expressed as:

$$\sigma_{M_f} = (\tau_{M_{max}})_{fracture} \qquad [4.22]$$

where $(\tau_{M_{max}})_{fracture}$ is the maximal macroscopic shear stress measured at the fracture of the numerical sample. Table 4.1 summarizes the different values of the macroscopic fracture stress obtained using four different numerical samples discretized with approximately $10,000$ discrete elements. These results show a very good correlation with those obtained from the tensile tests ($0.3\,\%$ error). Moreover, at the structure scale, the crack geometry seems in agreement with the brittle fracture theory (Figure 4.9). The crack surface is oriented at $45°$ to the main axis of the numerical sample.

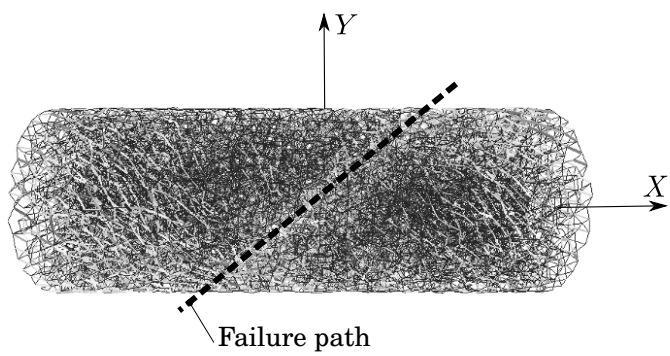

Figure 4.9. *Illustration of the crack morphology obtained from torsion test*

4.2.4.3. *Quasi-static 2D spherical indention*

The first two validation tests show that this model gives relatively good results at the structure scale. The numerical samples fail at the expected macroscopic fracture stress. Furthermore, the fracture surfaces seem in accordance with the brittle fracture theory. To investigate this last point more closely, 2D spherical indentation was simulated using this fracture model. Figure 4.10 shows the associated results. This simulation does not produce the Hertzian cone crack as experimentally observed (Figure 4.11). Instead, several cracks initiate beneath the indenter and propagate vertically throughout the thickness of the material being simulated. In conclusion, even this model is moderately satisfactory at the structure scale [AND 12a, SRI 13], it cannot reproduce correctly the cracking mechanisms at the microscopic scale.

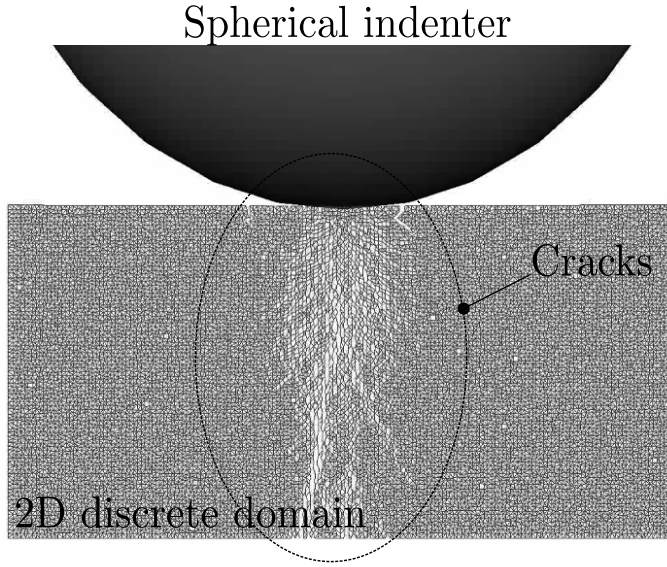

Figure 4.10. *2D spherical indentation with beam-based fracture model. For a color version of the figure, see www.iste.co.uk/jebahi/discrete.zip*

Figure 4.11. *The Hertzian cone crack under spherical indenter, as experimentally observed (taken from [ROE 56])*

4.3. Fracture model based on the virial stress

To overcome the limitations of the beam-based fracture models, another model based on a non-local formulation was proposed. The idea behind this model is that, in continuum mechanics, several techniques profiting from a solid foundation have been proposed to describe fracture. Therefore, it can be beneficial to apply these techniques in discrete mechanics. To achieve this aim, it is important to know the relationships between certain microscopic (of discrete elements) and macroscopic (of continua) quantities, allowing for discrete-continuum mechanics bridging. Chapter 1 has detailed several approaches used to this end. The present fracture model is based on one of these approaches: the virial stress technique which is used to compute an equivalent Cauchy stress tensor from discrete element forces and positions.

4.3.1. *Fracture criterion*

The proposed non-local fracture model is based on the computation of an equivalent Cauchy stress tensor at the discrete elements, taking into account their neighbors. Using [1.13], this tensor can be expressed at a discrete element i as follows:

$$\bar{\boldsymbol{\sigma}}_i = \frac{1}{2\,V_i} \sum_{j=1}^{N_{neigh}} \frac{1}{2} \left(\mathbf{l}^{ij} \otimes \mathbf{f}^{ij} + \mathbf{f}^{ij} \otimes \mathbf{l}^{ij} \right) \qquad [4.23]$$

where N_{neigh} is the number of discrete elements connected to the discrete element i and V_i is a volume associated with i at which the stress tensor is assessed. This volume is chosen in this work as the volume of the discrete element i. This choice allows us to take into account only the interactions between the regarded discrete element and its neighbors in computation of the equivalent Cauchy stress tensor. Larger volume can also be used to better reinforce the "non-local" character of the present fracture model. However, a very large volume can affect the accuracy of the obtained stress tensor. Further works would be done to accurately choose this parameter.

Remember that in this work it is assumed that completely brittle fracture occurs in the studied material, and such fracture type is thought to be initiated under tensile stress in mode I. Therefore, the new criterion postulates that a discrete element i is released from its neighbors when the associated hydrostatic stress computed, using:

$$P^i_{hyd} = \frac{1}{3}\,\mathrm{trace}(\bar{\boldsymbol{\sigma}}_i), \qquad [4.24]$$

is positive (tension state at i) and exceeds the fracture strength σ_{hyd_f}. In this case, all the beam bonds linking this discrete element to its neighbors break and are not taken into account anymore to compute the interparticle forces and torques at the next time step. Figure 4.12 shows an illustration of the cracking process using the new criterion.

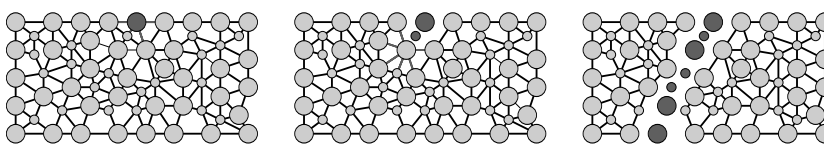

Figure 4.12. *The cracking mechanisms at the microscopic scale using the new fracture model*

Here, the fracture strength σ_{hyd_f} can be different from the macroscopic fracture stress measured at the macroscopic scale σ_{M_f}. This difference is due to the fact that the definition of the volume V_i is not precise. Further work must be done to find the appropriate V_i that ensures the equivalence of σ_{hyd_f} and σ_{M_f}. In this work, σ_{hyd_f} corresponding to σ_{M_f} is to be determined by calibration.

4.3.2. *Calibration*

The fracture strength σ_{hyd_f} was calibrated using the same procedure as in the calibration of the beam-based model. A series of quasi-static tensile tests were processed with different values of σ_{hyd_f}. Each test was repeated four times using different discretized numerical samples to verify the repeatability of the tests. All the numerical samples used in these tests were discretized with approximately $10,000$ discrete elements. Figure 4.13 presents the calibration results. The macroscopic fracture stress evolves linearly with the microscopic one. The calibrated value of σ_{hyd_f} which corresponds to the silica glass fracture stress $\sigma_{M_f}^{Silica} = 50\,\mathrm{MPa}$ is approximately: $\sigma_{hyd_f}^{Silica} = 64\,\mathrm{MPa}$.

4.3.3. *Convergence study*

The dependence of the macroscopic fracture stress σ_{M_f} on the number of discrete elements N was studied. In this study, the calibrated value of the fracture stress $\sigma_{hyd_f}^{Silica} = 64\,\mathrm{MPa}$ was used. Figure 4.14 presents the evolution of σ_{M_f} with respect to the number of discrete elements N. A good stability of the macroscopic fracture stress around the silica glass value of $\sigma_{M_f}^{Silica} = 50\,\mathrm{MPa}$ was obtained. Furthermore, σ_{M_f} converges to $\sigma_{M_f}^{Silica}$ more quickly than when using the beam-based model, indicating that the present model is more suitable to study cracking mechanisms at small scales. The given dispersion of 13% is in the same order of magnitude as

the dispersion obtained using the beam-based model. This dispersion could be accepted, since larger dispersions can be found in the literature [HEN 04a].

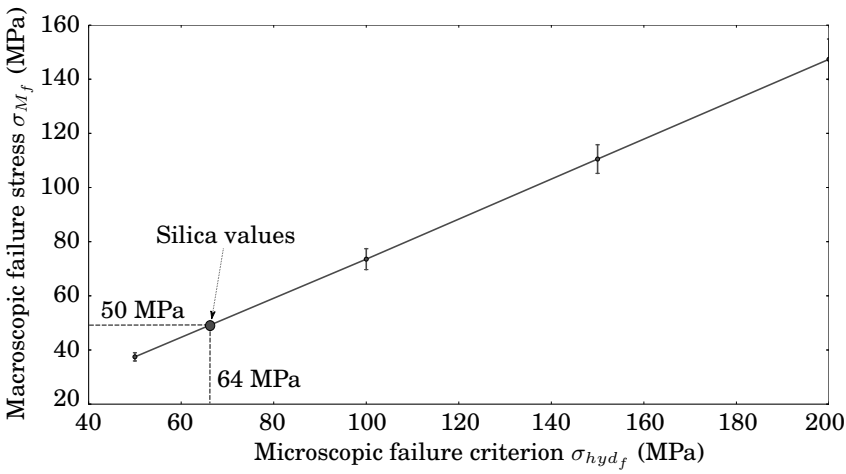

Figure 4.13. *Calibration of the fracture stress σ_{hyd_f} of silica glass*

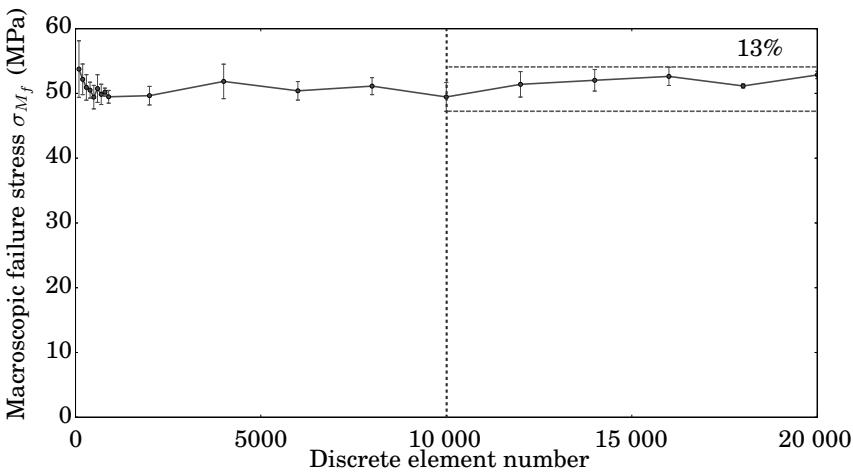

Figure 4.14. *Evolution of the macroscopic fracture stress σ_{M_f} as a function of the number of discrete elements, using the virial stress based model*

4.3.4. *Validation*

To validate this model at the structure scale, it was applied to simulate the reference tests used to validate the first beam-based model in sections 4.2.4.1 and 4.2.4.2 (bending and torsion tests of 3D beams). The fracture strength σ_{hyd_f} is fixed at $64\ MPa$, which corresponds to the macroscopic fracture stress of silica glass. Table 4.2 summarizes the macroscopic fracture stresses obtained from the tensile, bending and torsion tests. Fairly similar average macroscopic fracture stresses were obtained, which is in agreement with the material strength theory. To verify the crack morphology, the crack geometry obtained from the torsion test has been observed (Figure 4.15). A crack path is developed along a helical surface oriented at $45°$ to the main axis of the numerical sample (3D beam with circular base). This result is in accordance with the material strength theory, much better than that obtained using the beam-based fracture model.

Sample	Tensile (MPa)	Bending (MPa)	Torsion (MPa)
No. 1	53.3	47.0	51.5
No. 2	48.0	47.0	47.6
No. 3	48.3	46.2	50.9
No. 4	48.2	55.5	47.7
Average	49.5	48.9	49.4
Difference	*Reference*	1.2 %	0.2 %

Table 4.2. *Overview of the macroscopic fracture stresses from tensile, bending and torsional tests: four discrete samples made up of approximately* $10,000$ *discrete elements are used*

To better investigate the cracking mechanisms at smaller scales, the 2D spherical indentation was simulated using the present fracture model. Figure 4.16 shows the associated result. As expected, the crack pattern exhibits a cone geometry (Figure 4.16). It is clear that this model allows us to

describe more precisely the cracking mechanisms at small scales.

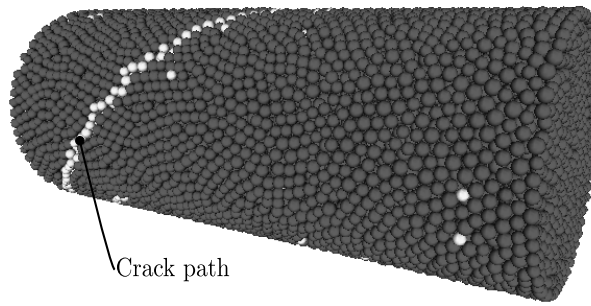

(a) View showing all discrete elements

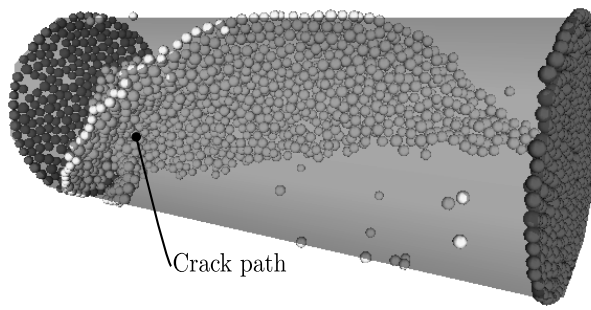

(b) View showing only critical discrete elements

Figure 4.15. *View of crack path in a torsional test; the discrete elements in which the fracture criterion is fulfilled are highlighted. For a color version of the figure, see www.iste.co.uk/jebahi/discrete.zip*

4.4. Conclusion

The present chapter has dealt with one of the most important phenomena encountered in material science and engineering: brittle fracture of materials. This phenomenon is the most fundamental issue motivating contemporary efforts toward discrete element modeling of continua.

First, one of the commonly used bond-based models was adapted to the present variation of the DEM. This model is based on the computation of the equivalent principle stress in the cohesive beams. Calibration of this model was performed using quasi-static tensile tests. As elastic parameters, the calibrated microscopic fracture stress is applicable for any discrete domain that is used to model the same material and is prepared following the methodology presented in Chapter 2. Validation of this model has shown that it is able to provide relatively good results at the structure level, however, it fails to reproduce the cracking mechanisms at smaller scales.

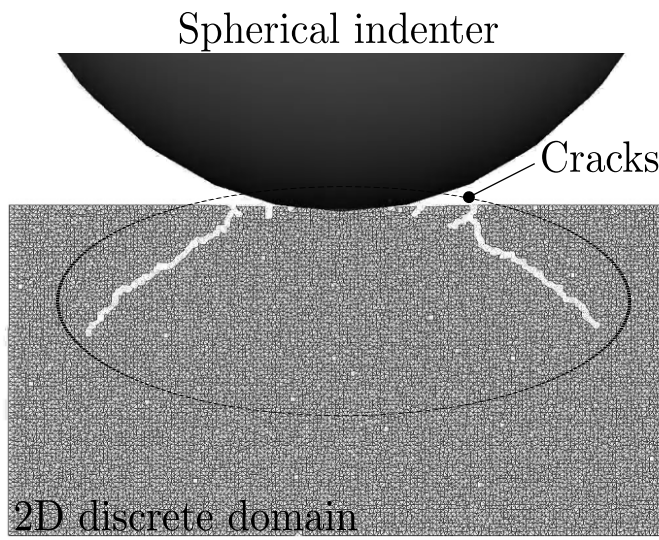

Figure 4.16. *Qualitative 2D indentation test showing cracks produced when using the new fracture criterion. For a color version of the figure, see www.iste.co.uk/jebahi/discrete.zip*

To overcome the limitations of the beam-based models, another approach has been proposed. This approach is based on a non-local formulation in which equivalent Cauchy stresses are assessed at the discrete elements, taking into account all their neighbors. Application of this approach to model various fracture problems has shown that relatively

good results are obtained at both macroscopic and microscopic scales.

The use of one of these two models in practice depends on what is expected from the simulated problem as well as on the analysis scale.

Conclusion

This book presents recent works on the modeling of continuum physics with the discrete element methods. The main interest of these approaches is to deal with problems where the studied domains become highly discontinuous: multiphase materials such as the composite materials, multicracked materials such as the brittle materials or metamaterials such as the technological foams. With these kinds of problems, the continuum approaches consist of homogenizing a representative material volume and deducing an average behavior on this volume. This process leads to loss of important local data that can drive some non-negligible effects at higher scales. For example, during a quasi-brittle material loading, a microcrack network appears and some of these microcracks coalesce to produce a macrocrack that leads to the collapse of the whole structure. Nevertheless, modeling these phenomena with discrete element method (DEM) is a hard and exciting challenge. The material behaviors are generally expressed and modeled with the continuum mechanics paradigm. How can we model and what is the significance of these physical quantities such as the Young's modulus, and the strain or the stress with the discrete mechanics? These questions are tackled and discussed throughout this book. After a general introduction, the book has described the following key characteristics.

Discrete Element Method to Model 3D Continuous Materials, First Edition.
Mohamed Jebahi, Damien André, Inigo Terreros and Ivan Iordanoff.

Chapter 1 gave a brief review on discrete element modeling. A classification of the DMs, the most commonly used method, was presented in order to introduce the one used in this book. According to the analysis scale, three classes can be distinguished. From these classes, the mesoscopic discrete methods (MDMs) are used at the mesoscopic scale which is the scale of interest of most of the complex phenomena that cannot easily be handled by continuum approaches. From the existing MDMs, the hybrid lattice-particle methods are the most adapted to model continuous materials. This is why the discrete method addressed in this book belongs to this category. This method, which is based on discrete mechanics, is dedicated to the modeling of continuous materials whose mechanical behavior is generally described by continuum mechanics. The second part of this chapter dealt with some numerical techniques to link these two classes of mechanics (continuum and discrete mechanics).

Chapter 2 described a general methodology to model a continuum using the chosen lattice-particle approach, with an application to elastic materials. This methodology can be divided into two parts. The first part is concerned with discrete domain construction, which plays an important role in the mechanical behaviors. As shown, the construction of the discrete domain must follow several geometrical conditions to ensure isotropy and refining independence of the simulation results. The second part is concerned with the mechanical behavior of the cohesive beams between the discrete elements. A calibration approach was detailed to determine the appropriate microscopic parameters (of the cohesive beams) that ensure a correct macroscopic mechanical behavior. To simplify the calibration process, a numerical study was also given. This study has allowed to find relationships between the microscopic and macroscopic parameters. Finally, to validate the presented methodology, it was applied to simulate several reference tests. The obtained

results are in good agreement with analytical and other numerical results. The dependence of these results on the number of discrete elements was also studied. Contrary to existing approaches, beyond $10,000$ discrete elements, the simulation results are relatively independent of this number. In the two last chapters, this general framework was applied to model thermal and brittle fracture behaviors.

Chapter 3 proposed an original and fast calculation method to compute thermal conduction in 3D continuous materials, using the present DEM variation. This method is an extension of the works of Hahn *et al.* [HAH 10] who have developed an approach to predict thermal conduction in two-dimensional (2D) discrete domains formed by hexagonal discrete elements. To validate this method, it was applied to simulate several reference tests involving high-temperature gradients. The obtained results are in good agreement with other analytical and numerical results obtained from finite element method (FEM) calculations.

Chapter 4 proposed two brittle fracture criteria to model complex cracking problems. The first criterion is based on a local formulation involving the cohesive beams and is inspired by the Rankine criterion, which is widely used to model brittle fracture. Application of this model has shown that it can give relatively good results at the structure scale. However, it fails to reproduce correctly the cracking mechanisms at smaller scales. To overcome this problem, another criterion based on a non-local formulation was developed. It consists of computing an equivalent Cauchy stress tensor at each discrete element taking into account its neighbors. As shown, this criterion provides relatively good results at both microscopic and macroscopic scales, better than when using the first beam-based criterion.

The aim of this book is to propose a rigorous scientific framework to the DEM applied to continuum. The main steps to achieve this goal are described from the discrete domain

creation to the validation tests. The physical behavior of the discrete domain is introduced through the rheological models implemented by the bonds between the discrete elements. The choice of the relevant rheological model is of utmost importance and is generally based on micromechanical considerations.

The application of preset DEM variation to continuum is relevant at the microscopic scale, where the material discontinuities and material heterogeneity appear. For example, the behavior of ceramic microstructures, which is highly heterogeneous, can be investigated using DEM. At this scale, one problem is how to model the boundary conditions and the loadings that are applied very far from the studied zone. To take into account these conditions, the DEM can be coupled with continuum methods such as FEM or constrained natural element method (CNEM) [JEB 14, JEB 13a, JEB 13c]. The second book in the series is dealt with this hot question.

Finally, the application of DEM for computational structure in engineering design is presently not feasible. The barriers are both technical and theoretical: high computational resource requirement, the lack of easy-to-use software and the lack of a well-designed theoretical framework. We hope that this set of book will provide concrete solutions to these scientific and technical problems.

Bibliography

[ABR 02] ABRAHAM F.F., WALKUP R., GAO H., *et al.*, "Simulating materials failure by using up to one billion atoms and the world's fastest computer: brittle fracture", *Proceedings of the National Academy of Sciences of the United States of America*, vol. 99, no. 9, pp. 5777–5782, 2002.

[ALD 57] ALDER B., WAINWRIGHT T., "Phase transition for a hard sphere system", *Journal of Chemical Physics*, vol. 27, pp. 1208–1209, 1957.

[ALD 59] ALDER B., WAINWRIGHT T., "Studies in molecular dynamics. I. General method", *Journal of Chemical Physics*, vol. 31, pp. 459–466, 1959.

[AND 12a] ANDRÉ D., Modélisation par éléments discrets des phases d'ébauchage et de doucissage de la silice, PhD Thesis, Université Bordeaux 1, 2012.

[AND 12b] ANDRÉ D., IORDANOFF I., CHARLES J.L., *et al.*, "Discrete element method to simulate continuous material by using the cohesive beam model", *Computer Methods in Applied Mechanics and Engineering*, vol. 213–216, pp. 113–125, 2012.

[AND 13] ANDRÉ D., JEBAHI M., IORDANOFF I., *et al.*, "Using the discrete element method to simulate brittle fracture in the indentation of a silica glass with a blunt indenter", *Computer Methods in Applied Mechanics and Engineering*, vol. 265, pp. 136–147, 2013.

Discrete Element Method to Model 3D Continuous Materials, First Edition.
Mohamed Jebahi, Damien André, Inigo Terreros and Ivan Iordanoff.

[AND 14] ANDRÉ D., IORDANOFF I., CHARLES J.L., *et al.*, "The GranOO workbench, a new tool for developing discrete element simulations, and its application to tribological problems", *Advances in Engineering Software*, vol. 74, pp. 40–48, 2014.

[ASH 76] ASHCROFT N., MERMIN N., *Solid State Physics*, Hardcover, 1976.

[ASH 86] ASH P., BOLKER E., "Generalized Dirichlet tessellations", *Geometriae Dedicata*, vol. 20, no. 2, pp. 209–243, 1986.

[BAG 93] BAGI K., "On the definition of stress and strain in granular assemblies through the relation between micro- and macro-level characteristics", in THORNTON C., (ed.), *Powders and Grains 1993*, Balkema, Rotterdam, pp. 117–121, 1993.

[BAG 95] BAGI K., "Geometrical modeling of granular assemblies", *Acta technica Academiae Scientiarum Hungaricae*, vol. 107, nos. 1–2, pp. 1–16, 1995.

[BAG 96] BAGI K., "Stress and strain in granular assemblies", *Mechanics of Materials*, vol. 22, pp. 165–177, 1996.

[BAG 05] BAGI K., "An algorithm to generate random dense arrangements for discrete element simulations of granular assemblies", *Granular Matter*, vol. 7, pp. 31–43, 2005.

[BAG 06] BAGI K., "Analysis of microstructural strain tensors for granular assemblies", *International Journal of Solids and Structures*, vol. 43, pp. 3166–3184, 2006.

[BEL 94] BELYTSCHKO T., LU Y.Y., GU L., "Element-free Galerkin methods", *International Journal for Numerical Methods in Engineering*, vol. 37, pp. 229–256, 1994.

[BEN 92] BENSON D.J., "Computational methods in Lagrangian and Eulerian hydrocodes", *Computer Methods in Applied Mechanics and Engineering*, vol. 99, nos. 2–3, pp. 235–394, 1992.

[BOB 09] BOBET A., FAKHIMI A., JOHNSON S., *et al.*, "Numerical models in discontinuous media: review of advances for rock mechanics applications", *Journal of Geotechnical and Geoenvironmental Engineering*, vol. 135, no. 11, pp. 1547–1561, 2009.

[BRA 02] BRATBERG I., RADJAÏ F., HANSEN A., "Dynamic rearrangements and packing regimes in randomly deposited two-dimensional granular beds", *Physical Review E*, vol. 66, p. 031303, 2002.

[CAI 95] CAILLERIE D., "Evolution quasistatique d'un milieu granulaire, loi incrémentale par homogénéisation", *Des Matériaux aux Ouvrages*, Hermes, Paris, pp. 53–80, 1995.

[CAM 98] CAMBOU B., *Behaviour of Granular Materials*, illustrated ed. edition, Springer, 1998.

[CAM 00] CAMBOU B., CHAZE M., DEDECKER F., "Change of scale in granular materials", *European Journal of Mechanics A/Solids*, vol. 19, pp. 999–1014, 2000.

[CAM 09] CAMBOU B., JEAN M., RADJAÏ F., *Micromechanics of Granular Materials*, Wiley, 2009.

[CAR 08] CARMONA H., WITTEL F., KUN K., *et al.*, "Fragmentation processes in impact of spheres", *Physical Review E*, vol. 77, no. 5, pp. 051302–051312, 2008.

[CHA 76] CHAPUIS R., De la structure géométrique, PhD Thesis, Ecole Polytechnique Montreal, 1976.

[CHA 15] CHARLES J.L., ANDRÉ D., IORDANOFF I., *3D Discrele Element Workbench for Highly Dynamic Thermo-mechnical Analysis*, ISTE, London and John Wiley & Sons, New York, 2015.

[CHE 01] CHEN S., WANG T., "Strain gradient theory with couple stress for crystalline solids", *European Journal of Mechanics A/Solids*, vol. 20, pp. 739–756, 2001.

[CHE 03] CHESSA J., WANG H., BELYTSCHKO T., "On the construction of blending elements for local partition of unity enriched finite elements", *International Journal for Numerical Methods in Engineering*, vol. 57, no. 7, pp. 1015–1038, 2003.

[CHI 11] CHINESTA F., CUETO E., CESCOTTO S., *et al.*, *Natural Element Method for the Simulation of Structures and Processes*, ISTE, London and John Wiley & Sons, New York, 2011.

[CHU 96] CHUNG J.W., ROOS A., HOSSON J.T.M.D., *et al.*, "Fracture of disordered three-dimensional spring networks: a computer simulation methodology", *Physical Review B*, vol. 54, pp. 15094–15100, December 1996.

[COS 09] COSSERAT E., COSSERAT F., *Théorie des corps déformables (Theory of Deformable Bodies)*, A. Hermann and Sons, 1909.

[CRA 56] CRANK J., *The Mathematics of Diffusion*, 2nd ed., Oxford University Press edition, 1956.

[CUN 71] CUNDALL P.A., "Computer model for simulating progressive large scale movements in blocky rock systems", *Proceedings of the Symposium of the International Society of Rock Mechanics*, Nancy, France, 1971.

[CUN 79] CUNDALL P.A., STRACK O.D.L., "A discrete numerical model for granular assemblies", *Geotechnique*, vol. 29, pp. 47–65, 1979.

[CUN 88] CUNDALL P.A., "Formulation of a three-dimensional distinct element model – part I, a scheme to detect and represent contacts in a system composed of many polyhedral blocks", *International Journal of Rock Mechanics and Mining Sciences*, vol. 25, pp. 107–116, 1988.

[D'AD 01] D'ADDETTA G.A., KUN F., RAMM E., *et al.*, "From solids to granulates – discrete element simulations of fracture and fragmentation processes in geomaterials", *Continuous and Discontinuous Modeling of Cohesive-Frictional Materials*, vol. 568 of Lecture Notes in Physics, Springer, Berlin, Heidelberg, pp. 231–258, 2001.

[D'AD 02] D'ADDETTA G.A., KUN F., RAMM E., "On the application of a discrete model to the fracture process of cohesive granular materials", *Granular Matter*, vol. 4, no. 2, pp. 77–90, 2002.

[D'AD 06] D'ADDETTA G.A., RAMM E., "A microstructure-based simulation environment on the basis of an interface enhanced particle model", *Granular Matter*, vol. 8, no. 3, pp. 159–174, 2006.

[DON 09] DONZÉ F.V., RICHEFEU V., MAGNIER S.A., "Advances in discrete element method applied to soil, rock and concrete mechanics, in: state of the art of geotechnical engineering", *Electronic Journal of Geotechnical Engineering*, vol. 8, pp. 1–44, 2009.

[EBE 10] EBERLY D., *Game Physics*, 2nd ed., Elsevier, Morgan Kaufmann edition, 2010.

[ERI 68] ERINGEN A., "Theory of micropolar elasticity", Liebowitz H. edition, *Fracture*, vol. 2, Academic Press, pp. 662–729, 1968.

[FAK 07] FAKHIMI A., VILLEGAS T., "Application of dimensional analysis in calibration of a discrete element model for rock deformation and fracture", *Rock Mechanics and Rock Engineering*, vol. 40, no. 2, pp. 193–211, 2007.

[FIN 70] FINNEY J.L., "Random packings and the structure of simple liquids. I. The geometry of random close packing", *Proceedings of the Royal Society of London. Series A, Mathematical and Physical Sciences*, vol. 319, no. 1539, pp. 479–493, 1970.

[FOU 22] FOURIER J., *Théorie analytique de la chaleur*, F. Didot, 1822.

[FOU 01] FOULKES W., MITAS L., NEEDS R., *et al.*, "Quantum Monte Carlo simulations of solids", *Reviews of Modern Physics*, vol. 73, no. 1, pp. 33–83, 2001.

[GOD 86] GODDARD J., "Microstructural origins of continuum stress fields – a brief history and some unresolved issues", in DEKEE D., KALONI P., (eds.), *Recent Developments in Structered Continua. Pitman Research Notes in Mathematics*, Wiley, p. 179, 1986.

[GOT 74] GOTOH K., FINNEY J.L., "Statistical geometrical approach to random packing density of equal spheres", *Nature*, vol. 252, pp. 202–205, 1974.

[GRI 21] GRIFFITH A., "The phenomena of rupture and flow in solids", *Philosophical Transactions of the Royal Society of London Series A*, vol. 221, pp. 163–198, 1921.

[GRI 01] GRIFFITHS D.V., MUSTOE G.G.W., "Modeling of elastic continua using a grillage of structural elements based on discrete element concepts", *International Journal for Numerical Methods in Engineering*, vol. 50, no. 7, pp. 1759–1775, 2001.

[GUN 02] GUNARATNE G.H., RAJAPAKSA C.S., BASSLER K.E., *et al.*, "Model for bone strength and osteoporotic fractures", *Physical Review Letters*, vol. 88, p. 068101, January 2002.

[GUP 99] GUPTA O.G., *Finite and Boundary Element Methods in Engineering*, A.A. Belkema, 1999.

[HAD 11] HADJESFANDIARI A.R., DARGUSH G.F., "Couple stress theory for solids", *International Journal of Solids and Structures*, vol. 48, pp. 2496–2510, 2011.

[HAH 10] HAHN M., WALLMERSPERGER T., KRÖPLIN B., "Discrete element representation of continua: proof of concept and determination of the material parameters", *Computational Materials Science*, vol. 50, pp. 391–402, 2010.

[HAH 11] HAHN M., SCHWARZ M., KRÖPLIN B.H., *et al.*, "Discrete element method for the thermal field: proof of concept and determination of the material parameters", *Computational Materials Science*, vol. 50, no. 10, pp. 2771–2784, 2011.

[HAL 75] HALICIOĞLU T., POUND G., "Calculation of potential energy parameters", *Physica Status Solidi (A)*, vol. 30, pp. 619–623, 1975.

[HEH 03] HEHRE W., *A Guide to Molecular Mechanics and Quantum Chemical Calculations*, Wavefunction Press, Irvine, CA, 2003.

[HEN 04a] HENTZ S., DAUDEVILLE L., DONZÉ F.V., "Identification and validation of a discrete element model for concrete", *Journal of Engineering Mechanics*, vol. 130, no. 6, pp. 709–719, 2004.

[HEN 04b] HENTZ S., DONZÉ F.V., DAUDEVILLE L., "Discrete element modeling of concrete submitted to dynamic loading at high strain rates ", *Computers & Structures*, vol. 82, nos. 29–30, pp. 2509–2524, 2004.

[HOH 64] HOHENBERG P., KOHN W., "Inhomogeneous electron gas", *Physical Review B*, vol. 136, no. 864, pp. B864–B871, 1964.

[HRE 41] HRENNIKOFF A., "Solution of problems of elasticity by the frame-work method", *ASME Journal of Applied Mechanics*, vol. 8, pp. A619–A715, 1941.

[IBR 03] IBRAHIMBEGOVIC A., DELAPLACE A., "Microscale and mesoscale discrete models for dynamic fracture of structures built of brittle material", *Computers & Structures*, vol. 81, no. 12, pp. 1287–1299, 2003.

[ILL 11] ILLOUL A.L., LORONG P., "On some aspects of the CNEM implementation in 3D in order to simulate high speed machining or shearing", *Computers and Structures*, vol. 89, pp. 940–958, 2011.

[IOR 08] IORDANOFF I., BATTENTIER A., NEAUPORT J., *et al.*, "A discrete element model to investigate sub-surface damage due to surface polishing", *Tribology International*, vol. 41, no. 11, pp. 957–964, 2008.

[ISS 92] ISSA J.A., NELSON R.N., "Numerical analysis of micromechanical behaviour of granular materials", *Engineering Computations*, vol. 9, pp. 211–223, 1992.

[JEA 99] JEAN M., "The non smooth contact dynamics method", *Computer Methods in Applied Mechanics and Engineering*, vol. 177, nos. 3–4, pp. 235–257, 1999.

[JEB 13a] JEBAHI M., Discrete-continuum coupling method for simulation of laser-induced damage in silica glass, PhD Thesis, Bordeaux 1 University, 2013.

[JEB 13b] JEBAHI M., ANDRÉ D., DAU F., *et al.*, "Simulation of Vickers indentation of silica glass", *Journal of Non-Crystalline Solids*, vol. 378, pp. 15–24, 2013.

[JEB 13c] JEBAHI M., CHARLES J., DAU F., *et al.*, "3D coupling approach between discrete and continuum models for dynamic simulations (DEM-CNEM)", *Computer Methods in Applied Mechanics and Engineering*, vol. 255, pp. 196–209, 2013.

[JEB 14] JEBAHI M., DAU F., CHARLES J.L., *et al.*, "Multiscale modeling of complex dynamic problems: an overview and recent developments", *Archives of Computational Methods in Engineering*, Springer, Netherlands, pp. 1–38, 2014.

[JEB 15] JEBAHI M., DAU F., CHARLES J.L., *et al.*, *Discrete-Continuum Coupling Method to Simulate Highly Dynamic Multi-Scale Problems*, ISTE, London and John Wiley & Sons, New York, 2015.

[JIN 07] JING L., STEPHANSSON O., *Fundamentals of Discrete Element Methods for Rock Engineering: Theory and Applications*, Elsevier, 2007.

[KEN 84] KEN-ICHI K., "Distribution of directional data and fabric tensors", *International Journal of Engineering Science*, vol. 22, no. 2, pp. 149–164, 1984.

[KRU 96] KRUYT N., ROTHENBURG L., "Micromechanical definition of strain tensor for granular materials", *ASME Journal of Applied Mechanics*, vol. 118, pp. 706–711, 1996.

[KRU 03] KRUYT N., "Statics and kinematics of discrete Cosserat-type granular materials", *International Journal of Solids and Structures*, vol. 40, pp. 511–534, 2003.

[KUH 99] KUHN M., "Structured deformation in granular materials", *Mechanics of Materials*, vol. 31, pp. 407–429, 1999.

[KUH 01] KUHL E., D'ADDETTA G., LEUKART M., *et al.*, "Microplane modeling and particle modeling of cohesive-frictional materials", in VERMEER P., HERRMANN H., LUDING S., *et al.*, (eds.), *Continuous and Discontinuous Modeling of Cohesive-Frictional Materials*, vol. 568 of Lecture Notes in Physics, Springer, Berlin, Heidelberg, pp. 31–46, 2001.

[KUN 96] KUN F., HERRMANN H.J., "A study of fragmentation processes using a discrete element method", *Computer Methods in Applied Mechanics and Engineering*, vol. 138, nos. 1–4, pp. 3–18, 1996.

[LAW 93] LAWN B., *Fracture of Brittle Solids*, 2nd ed., Cambridge University Press, 1993.

[LAW 03] LAWN B.R., "Fracture and deformation in brittle solids: a perspective on the issue of scale", *Journal of Material Research*, vol. 19, pp. 22–29, 2003.

[LEO 02] LEONOVA A., VOLKOVB V., "Internal rotations and stress tensor symmetry in theories of nematic liquids and solids", *Los Alamos e-Print Archive: Condensed Matter*, vol. 0203265, available at http://adsabs.harvard.edu/cgi-bin/bib_query?arXiv:condmat/ 0203265, 2002.

[LEV 98] LEVIN D., "The approximation power of moving least-squares", *Mathematics of Computation*, vol. 67, no. 224, pp. 1517–1531, 1998.

[LIA 97] LIAO C.L., CHANG T.P., YOUNG D.H., *et al.*, "Stress-strain relationship for granular materials based on the hypothesis of best fit", *International Journal of Solids and Structures*, vol. 34, nos. 31–32, pp. 4087–4100, 1997.

[LIN 97] LIN X., NG T.T., "A three-dimensional discrete element model using arrays of ellipsoids", *Geotechnique*, vol. 47, no. 2, pp. 319–329, 1997.

[LIU 03] LIU G.R., LIU M.B., *Smoothed Particle Hydrodynamics: A Meshfree Particle Method*, World Scientific Publishing Co. Pvt. Ltd, 2003.

[LIU 10] LIU M.B., LIU G., "Smoothed particle hydrodynamics (SPH): an overview and recent developments", *Archives of Computational Methods in Engineering*, vol. 17, pp. 25–76, 2010.

[LOC 06] LOCHMANN K., OGER L., STOYAN D., "Statistical analysis of random sphere packings with variable radius distribution", *Solid State Sciences*, vol. 8, no. 12, pp. 1397–1413, 2006.

[LUB 90] LUBACHEVSKY B.D., STILLINGER F.H., "Geometric properties of random disk packings", *Journal of Statistical Physics*, vol. 60, pp. 561–583, 1990.

[LUD 96] LUDING S., CLÉMENT E., RAJCHENBACH J., *et al.*, "Simulations of pattern formation in vibrated granular media ", *Europhysics Letters*, vol. 36, no. 4, pp. 247–252, 1996.

[MAG 98] MAGNIER S.A., DONZÉ F.V., "Numerical simulations of impacts using a discrete element method", *Mechanics of Cohesive-Frictional Materials*, vol. 3, no. 3, John Wiley & Sons, Ltd., pp. 257–276, 1998.

[MAH 09] MAHÉO L., GROLLEAU V., RIO G., "Damping efficiency of the Tchamwa-Wielgosz explicit dissipative scheme under instantaneous loading conditions", *Comptes Rendus Mécanique*, vol. 337, nos. 11–12, pp. 722–732, 2009.

[MAR 03] MARTIN C.L., BOUVARD D., SHIMA S., "Study of particle rearrangement during powder compaction by the discrete element method", *Journal of the Mechanics and Physics of Solids*, vol. 51, no. 4, pp. 667–693, 2003.

[MCL 74] MCLELLAN A., "Virial theorem generalized", *American Journal of Physics*, vol. 42, no. 239, pp. 239–243, 1974.

[MET 49] METROPOLIS N., ULAM S., "The Monte Carlo method", *Journal of the American Statistical Association*, vol. 44, no. 247, pp. 335–341, 1949.

[MIN 62] MINDLIN R., TIERSTEIN H.F., "Effects of couple-stresses in linear elasticity", *Archive for Rational Mechanics and Analysis*, vol. 11, pp. 415–488, 1962.

[MOË 99] MOËS N., DOLBOW J., BELYTSCHKO T., "A finite element method for crack growth without remeshing", *International Journal for Numerical Methods in Engineering*, vol. 46, pp. 131–150, 1999.

[MOR 88] MOREAU J.J., PANAGIOTOPOULOS P.D., *Nonsmooth Mechanics and Applications*, Springer-Verlag, 1988.

[MOR 94] MOREAU J.J., "Some numerical methods in multibody dynamics: application to granular materials", *European Journal of Mechanics A/Solids*, vol. 13, no. 4, pp. 93–114, 1994.

[MOR 97] MOREAU J., *Numerical Investigation of Shear Zones in Granular Materials*, Grassberger P., Wolf D.E. edition, World Scientific, Singapore, pp. 233–247, 1997.

[MUN 04] MUNJIZA A., *The Combined Finite-Discrete Element Method*, John Wiley & Sons, 2004.

[OST 02] OSTOJA-STARZEWSKI M., "Lattice models in micromechanics", *Applied Mechanics Reviews*, vol. 55, pp. 35–60, 2002.

[PAY 92] PAYNE M., TETER M., ALLAN D., *et al.*, "Iterative minimization techniques for ab initio total-energy calculations: molecular dynamics and conjugate gradients", *Reviews of Modern Physics*, vol. 64, no. 1045, pp. 1045–1097, 1992.

[PÖS 01] PÖSCHEL T., LUDING S., *Granular Gases*, vol. 564 of Lecture Notes in Physics, Springer, 2001.

[PÖS 05] PÖSCHEL T., SCHWAGER T., *Computational Granular Dynamics*, Springer, 2005.

[POT 95a] POTAPOV A., CAMPBELL C., HOPKINS M., "A two-dimensional dynamic simulation of solid fracture part I: description of the model", *International Journal of Modern Physics*, vol. 6, no. 3, pp. 371–397, 1995.

[POT 95b] POTAPOV A.V., CAMPBELL C.S., HOPKINS M.A., "A two-dimensional dynamic simulation of solid fracture part II: examples", *International Journal of Modern Physics*, vol. 6, no. 3, pp. 399–425, 1995.

[POT 04] POTYONDY D., CUNDALL P., "Abonded-particle model for rock", *International Journal of Rock Mechanics & Mining Sciences*, vol. 41, pp. 1329–1364, 2004.

[RAN 96] RANDLES P.W., LIBERSKY L.D., "Smoothed particle hydrodynamics: some recent improvements and applications", *Computer Methods in Applied Mechanics and Engineering*, vol. 139, pp. 375–408, 1996.

[RAP 80] RAPAPORT D.C., "The event scheduling problem in molecular dynamic simulation", *Journal of Computational Physics*, vol. 34, pp. 184–201, 1980.

[RIC 07] RICHARD D., IORDANOFF I., BERTHIER Y., *et al.*, "Friction coefficient as a macroscopic view of local dissipation", *Journal of Tribology*, vol. 129, no. 4, pp. 829–835, 2007.

[RIC 08] RICHARD D., IORDANOFF I., RENOUF M., *et al.*, "Thermal study of the dry sliding contact with third body presence", *ASME Journal of Tribology*, vol. 130, no. 3, pp. 031404–031414, 2008.

[ROE 56] ROESLER F.C., "Brittle fractures near equilibrium ", *Proceedings of the Physical Society. Section B*, vol. 69, no. 10, pp. 981–992, 1956.

[ROT 80] ROTHENBURG L., Micromechanics of idealized granular materials, PhD Thesis, Carleton University, Ottawa, Canada, 1980.

[ROU 04] ROUGIER E., MUNJIZA A., JOHN N., "Numerical comparison of some explicit time integration schemes used in DEM, FEM/DEM and molecular dynamics", *International Journal for Numerical Methods in Engineering*, vol. 62, pp. 856–879, 2004.

[SAT 04] SATAKE M., "Tensorial form definitions of discrete mechanical quantities for granular assemblies", *International Journal of Solids and Structures*, vol. 41, pp. 5775–5791, 2004.

[SCH 92a] SCHLANGEN E., VAN MIER J.G.M., "Experimental and numerical analysis of micromechanisms of fracture of cement-based composites", *Cement and Concrete Composites*, vol. 14, no. 2, pp. 105–118, 1992.

[SCH 92b] SCHLANGEN E., VAN MIER J.G.M., "Simple lattice model for numerical simulation of fracture of concrete materials and structures", *Materials and Structures*, vol. 25, no. 9, pp. 534–542, 1992.

[SCH 96] SCHLANGEN E., GARBOCZI E.J., "New method for simulating fracture using an elastically uniform random geometry lattice", *International Journal of Engineering Science*, vol. 34, no. 10, pp. 1131–1144, 1996.

[SCH 97] SCHLANGEN E., GARBOCZI E., "Fracture simulations of concrete using lattice models: computational aspects", *Engineering Fracture Mechanics*, vol. 57, nos. 2–3, pp. 319–332, 1997.

[SHA 97] SHABANA A.A., *Vibration of Discrete and Continuous Systems*, 2nd ed., Mechanical Engineerings Series, Springer, 1997.

[SHI 09] SHIU W., DONZÉ F.V., DAUDEVILLE L., "Discrete element modeling of missile impacts on a reinforced concrete target", *International Journal of Computer Applications in Technology*, vol. 34, no. 1, pp. 33–41, 2009.

[SRI 13] SRIVASTAVA A.K., GOPE P.C., *Strength of Materials*, PHI Learning Pvt. Ltd., 2013.

[STA 88] STANLEY H.E., OSTROWSKY N., *Random Fluctuations and Pattern Growth: Experiments and Models*, Springer Netherlands, 1988.

[SWE 83] SWENSON R., "Comments for virial systems for bounded systems", *American Journal of Physics*, vol. 51, pp. 940–942, 1983.

[SZA 89] SZABO A., OSTLUND N., *Modern Quantum Chemistry: Introduction to Advanced Electronic Structure Theory*, McGraw-Hill, New York, NY, 1989.

[TAN 09] TAN Y., YANG D., SHENG Y., "Discrete element method (DEM) modeling of fracture and damage in the machining process of polycrystalline sic", *Journal of the European Ceramic Society*, vol. 29, no. 6, pp. 1029–1037, 2009.

[TAV 06] TAVAREZ F.A., PLESHA M.E., "Discrete element method for modeling solid and particulate materials", *International Journal for Numerical Methods in Engineering*, vol. 70, pp. 379–404, 2006.

[TER 13] TERREROS I., IORDANOFF I., CHARLES J., "Simulation of continuum heat conduction using DEM domains", *Computational Materials Science*, vol. 69, pp. 46–52, 2013.

[TIM 83] TIMOSHENKO S., *History of Strength of Materials: With a Brief Account of the History of Theory of Elasticity and Theory of Structure*, Dover, New York, NY, 1983.

[TIN 93] TING J.M., KHWAJA M., MEACHUM L., *et al.*, "An ellipse-based discrete element model for granular materials", *International Journal of Analytical and Numerical Methods in Geomechanics*, vol. 17, no. 9, pp. 603–623, 1993.

[TOU 62] TOUPIN R., "Elastic materials with couple-stresses", *Archive for Rational Mechanics and Analysis*, vol. 11, pp. 385–414, 1962.

[TSA 79] TSAI D., "The virial theorem and stress calculation in molecular dynamics", *Journal of Chemical Physics*, vol. 70, pp. 1375–1382, 1979.

[VAR 01] VARGAS W.L., MCCARTHY J.J., "Heat conduction in granular materials", *AIChE Journal*, vol. 47, no. 5, pp. 1052–1059, 2001.

[VAR 02a] VARGAS W.L., MCCARTHY J.J., "Conductivity of granular media with stagnant interstitial fluids via thermal particle dynamics simulation", *International Journal of Heat and Mass Transfer*, vol. 45, pp. 4847–4856, 2002.

[VAR 02b] VARGAS W.L., MCCARTHY J.J., "Stress effects on the conductivity of particulate beds", *Chemical Engineering Science*, vol. 57, pp. 3119–3131, 2002.

[VAR 03] VARGAS W.L., MURCIA J.C., PALACIO L.E., *et al.*, "Fractional diffusion model for force distribution in static granular media", *Physical Review E*, vol. 68, pp. 021302–021311, 2003.

[VAR 07] VARGAS W.L., MCCARTHY J.J., "Thermal expansion effects and heat conduction in granular materials", *Physical Review E*, vol. 76, pp. 041301–041309, 2007.

[VOI 87] VOIGT W., "Theoretische Studien fiber die Elastizitatsverhiltnisse der Kristalle (Theoretical studies on the elasticity relationships of crystals)", *Abhandlungen zur Geschichte der mathematischen Wissenschaften*, Springer, p. 34, 1887.

[WAN 08] WANG Y., MORA P., "Macroscopic elastic properties of regular lattices", *Journal of the Mechanics and Physics of Solids*, vol. 56, no. 12, pp. 3459–3474, 2008.

[YVO 04] YVONNET J., RYCKELYNCK D., LORONG P., *et al.*, "A new extension of the natural element method for non-convex and discontinuous problems: the constrained natural element method (C-NEM)", *International Journal for Numerical Methods in Engineering*, vol. 60, pp. 1451–1474, 2004.

[ZHO 03] ZHOU M., "A new look at the atomic level virial stress: on continuum-molecular system equivalence", *Proceedings of the Royal Society A*, vol. 459, pp. 2347–2392, 2003.

[ZIE 05a] ZIENKIEWICZ O.C., TAYLOR R.L., *The Finite Element Method for Solid and Structural Mechanics*, Elsevier, 2005.

[ZIE 05b] ZIENKIEWICZ O.C., TAYLOR R.L., NITHIARASU P., *The Finite Element Method for Fluid Dynamics*, Elsevier, 2005.

[ZIE 05c] ZIENKIEWICZ O.C., TAYLOR R.L., ZHU J.Z., *Finite Element Method: Its Basis & Fundamentals*, Elsevier, 2005.

Index

Discrete Element Method to Model 3D Continuous Materials, First Edition.
Mohamed Jebahi, Damien André, Inigo Terreros and Ivan Iordanoff.

T

V

Other titles from

in

Numerical Methods in Engineering

2014

BECKERS Benoit, BECKERS Pierre
Reconciliation of Geometry and Perception in Radiation Physics

BERGHEAU Jean-Michel
Thermo-Mechanical Industrial Processes: Modeling and Numerical Simulation

BONNEAU Dominique, FATU Aurelian, SOUCHET Dominique
4-volume series
Hydrodynamic Bearings – Volume 1
Mixed Lubrication in Hydrodynamic Bearings – Volume 2
Thermo-hydrodynamic Lubricaton in Hydrodynamic Bearings – Volume 3
Internal Combustion Engine Bearings Lubrication in Hydrodynamic Bearings – Volume 4

DESCAMPS Benoît
Physical Form Finding of Lightweight Structures

2013

YASTREBOV Vladislav A.
Numerical Methods in Contact Mechanics

2012

DHATT Gouri, LEFRANÇOIS Emmanuel, TOUZOT Gilbert
Finite Element Method

2011

CHINESTA Francisco *et al.*
Natural Element Method for the Simulation of Structures and Processes

DAVIM Paulo J.
Finite Element Method in Manufacturing Processes

POMMIER Sylvie, GRAVOUIL Anthony, MOËS Nicolas, COMBESCURE Alain
Extended Finite Element Method for Crack Propagation

2010

SOUZA DE CURSI Eduardo, SAMPAIO Rubens
Modeling and Convexity

2008

BERGHEAU Jean-Michel, FORTUNIER Roland
Finite Element Simulation of Heat Transfer

EYMARD Robert
Finite Volumes for Complex Applications V

FREY Pascal, GEORGE Paul-Louis
Mesh Generation – 2nd edition

GAY Daniel, GAMBELIN Jacques
Modeling and Dimensioning of Structures

2005

BENKHALDOUN Fayssal
Finite Volumes for Complex Applications IV